REPORT DOCUMENTATION PAGE

Form Approved OMB NO. 0704-0188

1. REPORT DATE (DD-MM-YYYY)	2. REPORT TYPE	3. DATES COVERED (From - To)
22-07-2014	Ph.D. Dissertation	-

4. TITLE AND SUBTITLE
SYNTHESIS, CHARACTERIZATION AND APPLICATION OFFUNCTIONAL CARBON NANO MATERIALS

5a. CONTRACT NUMBER
W911NF-13-1-0138

5b. GRANT NUMBER

5c. PROGRAM ELEMENT NUMBER
206022

6. AUTHORS
Jin CHu

5d. PROJECT NUMBER

5e. TASK NUMBER

5f. WORK UNIT NUMBER

7. PERFORMING ORGANIZATION NAMES AND ADDRESSES
University of Puerto Rico at Rio Piedras
P. O. Box 21790

San Juan, PR 00931 -1790

8. PERFORMING ORGANIZATION REPORT NUMBER

9. SPONSORING/MONITORING AGENCY NAME(S) AND ADDRESS (ES)
U.S. Army Research Office
P.O. Box 12211
Research Triangle Park, NC 27709-2211

10. SPONSOR/MONITOR'S ACRONYM(S)
ARO

11. SPONSOR/MONITOR'S REPORT NUMBER(S)
62826-MS-REP.9

12. DISTRIBUTION AVAILIBILITY STATEMENT
Approved for public release; distribution is unlimited.

13. SUPPLEMENTARY NOTES
The views, opinions and/or findings contained in this report are those of the author(s) and should not contrued as an official Department of the Army position, policy or decision, unless so designated by other documentation.

14. ABSTRACT
The synthesis, characterizations and applications of carbon nanomaterials, including carbon nanorods, carbon nanosheets, carbon nanohoneycombs and carbon nanotubes were demonstrated. Different growth techniques such as pulsed laser deposition, DC/RF sputtering, hot filament physical vapour deposition, evaporative casting and vacuum filtration methods were introduced or applied for synthesizing carbon nanomaterials. The morphology, chemical compositions, bond structures, electronic, mechanical and sensing properties of the obtained samples were investigated.

15. SUBJECT TERMS
synhtesis, characterization, functionalied nano carbon

16. SECURITY CLASSIFICATION OF:			17. LIMITATION OF ABSTRACT	15. NUMBER OF PAGES	19a. NAME OF RESPONSIBLE PERSON
a. REPORT	b. ABSTRACT	c. THIS PAGE			Peter Feng
UU	UU	UU	UU		19b. TELEPHONE NUMBER 787-764-0000

Report Title

SYNTHESIS, CHARACTERIZATION AND APPLICATION OFFUNCTIONAL CARBON NANO MATERIALS

ABSTRACT

The synthesis, characterizations and applications of carbon nanomaterials, including carbon nanorods, carbon nanosheets, carbon nanohoneycombs and carbon nanotubes were demonstrated. Different growth techniques such as pulsed laser deposition, DC/RF sputtering, hot filament physical vapour deposition, evaporative casting and vacuum filtration methods were introduced or applied for synthesizing carbon nanomaterials. The morphology, chemical compositions, bond structures, electronic, mechanical and sensing properties of the obtained samples were investigated.

Tilted well-aligned carbon micro- and nano- hybrid rods were fabricated on Si at different substrate temperatures and incident angles of carbon source beam using the hot filament physical vapour deposition technique. The morphologic surfaces and bond structures of the oblique carbon rod-like structures were investigated by scanning electron microscopy, field emission scanning electron microscopy, transmission electron diffraction and Raman scattering spectroscopy. The field emission behaviour of the fabricated samples was also tested.

Carbon nanosheets and nanohoneycombs were also synthesized on Si substrates using a hot filament physical vapor deposition technique under methane ambient and vacuum, respectively. The four-point Au electrodes are then sputtered on the surface of the nanostructured carbon films to form prototypical humidity sensors. The sensing properties of prototypical sensors at different temperature, humidity, direct current, and alternative current voltage were characterized. Linear sensing response of sensors to relative humidity ranging from 11% to 95% is observed at room temperature. Experimental data indicate that the carbon nanosheets based sensors exhibit an excellent reversible behavior and long-term stability. It
also has higher response than that of the humidity sensor with carbon nanohoneycombs materials.
Conducting composite films containing carbon nanotubes (CNTs) were prepared in two different ways of evaporative casting and vacuum filtration methods using the biopolymer kappa-carrageenan (KC) as a dispersant. Evaporative casting and vacuum filtration film-formation processes were compared by testing electrical properties. Results showed that films produced using vacuum filtration had higher electrical properties than those prepared using the evaporative casting method. The evaporative casted multi walled carbon nanotubes composite films also performed as the best humidity sensor over all other films measured.

UNIVERSITY OF PUERTO RICO
RIO PIEDRAS CAMPUS
NATURAL SCIENCES FACULTY
DOCTORAL PROGRAM IN CHEMICAL PHYSICS

SYNTHESIS, CHARACTERIZATION AND APPLICATION OF FUNCTIONAL CARBON NANO MATERIALS

By

Jin Chu

A thesis submitted in partial fulfillment of the requirements for the degree of
Doctor of Philosophy

May 05, 2014

SYNTHESIS, CHARACTERIZATION AND APPLICATION OF FUNCTIONAL CARBON NANO MATERIALS

Accepted by the Faculty of the Doctoral Program in Chemical Physics of the University of Puerto Rico in partial fulfillment of the requirements for the degree of

Doctor of Philosophy

Dr. Peter X. Feng
Professor of the Department of Physics
Thesis Advisor

Dr. Luis F. Fonseca
Professor of the Department of Physics
Thesis Committee Member

Dr. Zhongfang Chen
Professor of the Department of Chemistry
Thesis Committee Member

May 05, 2014

TABLE OF CONTENT

Acknowledgements

The author give very special thanks to his thesis supervisor end research mentor Dr. Peter Xianping Feng, who offered him a chance to start his doctoral study and the opportunity to do current research, for the constant supports and guidance throughout his study and tremendous help in daily life. The financial supports through UPR-DEGI Scholarship for Academic Merit and Exceptional Executorships for one year, DEGI-PEAF for two years, and partially supports by grants NSF-DMR (0706147) and NASA-EPSCoR seed grant, are of great help in making the thesis possible.

The author appreciates Professor Luis F. Fonseca and Professor Zhongfang Chen not only for generously serving as the members of his thesis committee and correcting his research proposal, thesis, and valuable suggestions, but also for the graduate classes they had given to him.

The author thanks Professor Brad Weiner and Professor Gerardo Morell, who provided the support of the electron field emission experiment and pulsed laser system during the author's Ph.D study. The author thanks Dr. Vladimir Makarov for his assistance in laser system and Mr. Frank Mendoza for his help in field emission system.

The author also thanks Dr. Antonio Martinez and Ms. Ileana Desiderio for their kindly instructions in the enrollment process of graduate courses during the entire Ph.D study.

The author also acknowledge the group members (ever and present) in Prof. Feng's laboratory: Boqian Yang, Hongxin Zhang, Xinpeng Wang, Xiaoyan Peng, Rafael Velazquez and Eric Yiming Li for their great help and sharing throughout the author's doctoral study.

Thanks also give to the personnel of the Department of Physics, the Resource Center for Science and Engineering, the Decanato de Estudios Graduados e Investigacion (DEGI),

Office of International Student and Dean Office of Nature Science, especially Ms. Ileana Desiderio, Marilyn Rodriguez, Maria Vargas, Josefa Font, Lillian Nieves, Rosa M. Marrero Rivera, Caty Santiago, Mr. Carlos Pereira and Dr. Victor Orbegoso for doing all the paperwork regarding academic matters, purchase orders of scientific equipment, and scholarship matters.

Thank all the staff from Materials Characterization Center, Nanoscopy Facility, SPECLAB and ELECTRICAL CHARACTERIZATION LAB with very special thanks to Miss Christina for SEM measurements. Thank Prof. Maxime Guinel and Mr. Oscar Resto for SEM training and helping in SEM measurements, Mr. William and Anand P. Gaur from Prof. R. Katiyar's group for assistance with Raman and XRD measurements, Mr. Kiran Dasari from Prof. R. Palai's group for XPS measurements.

The author also thank their collaborators Dr. Marc in het Panhuis and Dr. Ali Aldalbahi from Soft Materials Group, School of Chemistry, and ARC Centre of Excellence for Electromaterials Science, University of Wollongong, Australia for the preparation and characterization of carbon nanotubes composite material.

Finally, the author thanks his wife Xiaoyan Peng and his son Yunong Chu Peng. Thanks Xiaoyan for all the love, caring and help during his PhD study. Thanks Yunong for his good behavior and lovely company during the PhD study and writing process of this thesis work.

Abstract

The synthesis, characterizations and applications of carbon nanomaterials, including carbon nanorods, carbon nanosheets, carbon nanohoneycombs and carbon nanotubes were demonstrated. Different growth techniques such as pulsed laser deposition, DC/RF sputtering, hot filament physical vapour deposition, evaporative casting and vacuum filtration methods were introduced or applied for synthesizing carbon nanomaterials. The morphology, chemical compositions, bond structures, electronic, mechanical and sensing properties of the obtained samples were investigated.

Tilted well-aligned carbon micro- and nano- hybrid rods were fabricated on Si at different substrate temperatures and incident angles of carbon source beam using the hot filament physical vapour deposition technique. The morphologic surfaces and bond structures of the oblique carbon rod-like structures were investigated by scanning electron microscopy, field emission scanning electron microscopy, transmission electron diffraction and Raman scattering spectroscopy. The field emission behaviour of the fabricated samples was also tested.

Carbon nanosheets and nanohoneycombs were also synthesized on Si substrates using a hot filament physical vapor deposition technique under methane ambient and vacuum, respectively. The four-point Au electrodes are then sputtered on the surface of the nanostructured carbon films to form prototypical humidity sensors. The sensing properties of prototypical sensors at different temperature, humidity, direct current, and alternative current voltage were characterized. Linear sensing response of sensors to relative humidity ranging from 11% to 95% is observed at room temperature. Experimental data indicate that the carbon nanosheets based sensors exhibit an excellent reversible behavior and long-term stability. It also has higher response than that of the humidity sensor with carbon nanohoneycombs

materials.

Conducting composite films containing carbon nanotubes (CNTs) were prepared in two different ways of evaporative casting and vacuum filtration methods using the biopolymer kappa-carrageenan (KC) as a dispersant. Evaporative casting and vacuum filtration film-formation processes were compared by testing electrical properties. Results showed that films produced using vacuum filtration had higher electrical properties than those prepared using the evaporative casting method. The evaporative casted multi walled carbon nanotubes composite films also performed as the best humidity sensor over all other films measured.

List of Figures

List of Tables

Chapter 1

Introduction and Outline

This chapter describes the motivation and outline of this thesis work. A brief review to the carbon phases and its allotropes, the properties of carbon nanomaterials, including structural properties, mechanical properties, electronic properties and the potential applications of carbon nanomaterials, is presented in this chapter.

1.1 Motivation

Of all the elements in the periodic table, only carbon provides the basis for life on earth. Carbon is also the key for many technological applications ranging from drugs to synthetic materials that have become indispensable in our daily life and have influenced the world's civilization for centuries [1, 2]. It allowed the beginnings of the industrial revolution, enabling the rise of the steel and chemical industries, it made the railways run, and it played a major role in the development of naval transportation. The increased device performance of information and data processing systems is changing our lives on a daily basis, producing scientific innovations for a new industrial era. However, success breeds its own problems, and there is ever more data to be handled—which requires a nanoscience approach [3].

Nanotechnology is considered to be the technology of the future; it is perhaps today's most advanced manufacturing technology, because it reaches the theoretical limit of accuracy which is the size of a molecule or atom. The last decade has seen advancement in every side of nanotechnology such as: nanoparticles and powders, nanolayers and coats, electrical, optic and mechanical nanodevices, and nanostructured biological materials. In manufacturing industry, two

interrelated trends are also clearly seen: the trend towards miniaturization and the trend towards ultra-precision processing [4]. Both trends are moving in the direction of nanotechnology, because both are tending to dimensions which lie in the range of several nanometers. Nanotechnology refers to the development of devices, structures, and systems whose size varies from 1 to 100 nanometers (nm).

The term "nanotechnology" was introduced by Nori Taniguchi in 1974 at the Tokyo International Conference on Production Engineering. He used the word to describe ultrafine machining: the processing of a material to nanoscale precision. This work was focused on studying the mechanisms of machining hard and brittle materials such as quartz crystals, silicon, and alumina ceramics by ultrasonic machining [5, 6]. However, American Physicist and Nobel Laureate Richard Feynman argued that the scanning electron microscope could be improved in resolution and stability, so that one would be able to "see" atoms. He proceeded to predict the ability to arrange atoms the way a researcher would want them, within the bounds of chemical stability, in order to build tiny structures that in turn would lead to molecular or atomic synthesis of materials [6, 7]. Based on Feynman's idea, K. E. Drexler advanced the idea of "molecular nanotechnology" in his books "*Engines of Creation"* (1986) and "*Nanosystems*" (1992) where he postulated the concept of using nanoscale molecular structures to act in a machinelike manner to guide and activate the synthesis of larger molecules. [8-10].

In the last three decades, zero-dimensional, one-dimensional, and two-dimensional carbon nanomaterials (such as fullerenes, carbon nanorods, carbon nanotubes, and grapheme…) have attracted significant attention from the scientific community due to their unique electronic, optical, thermal, mechanical, and chemical properties. Carbon nanomaterials, composed entirely of sp^2 bonded graphitic carbon, are found in all reduced dimensionalities including zero-dimensional

fullerenes, one-dimensional carbon nanotubes (CNTs), and two-dimensional graphene. With nanometer-scale dimensions, the properties of carbon nanomaterials are strongly dependent on their atomic structures and interactions with other materials. Advances in producing highly monodisperse carbon nanotube and graphene samples have renewed interest in employing them as the basis of electronic, optoelectronic, photovoltaic, and sensing applications[11]. CNTs are the most ideal and promising materials for future nanotechnology applications including field effect transistors, single electron transistors, field emission displays, memory devices, sensors and probes due to their remarkable thermal, electronic and mechanical properties [12, 13]. Meanwhile, research interest in graphene, a two-dimensional crystal consisting of a single atomic plane of carbon atoms, has also been driven by its extraordinary properties and widely potential applications [14, 15]. Recent measurements of the remarkable electronic properties of graphene have resulted in intense research activity. All these characteristics have put carbon and carbon-related nanomaterials in the spotlight of science and technology research.

1.2 Carbon Phases and carbon allotropes

The phase diagram of carbon (Fig. 1.1) was controversial for many years and only recently well established experimentally within the temperature range up to about 10,000 K and the pressure range up to about 100 Gpa, the higher region being still poorly understood [16, 17].

There are at least two stable solid phases of carbon: graphite with a crystalline hexagonal form and diamond with a tetrahedral form. Both forms can exist in the same quite wide range of thermodynamic conditions; however, graphite can be transformed to diamond only at very high pressures, above 10 GPa [18].

It is well known that at ambient pressure graphite will sublimate when heated rather than melt. The pressure of gaseous carbon is, however, relatively low, and at sufficient temperature and pressure

graphite will melt rather than vaporise. The two triple-points are estimated to locate at temperatures between 4300-4700 K, and pressures between 0.01 GPa (graphite - vapour -liquid) and 10 GPa (graphite - liquid - diamond) [19].

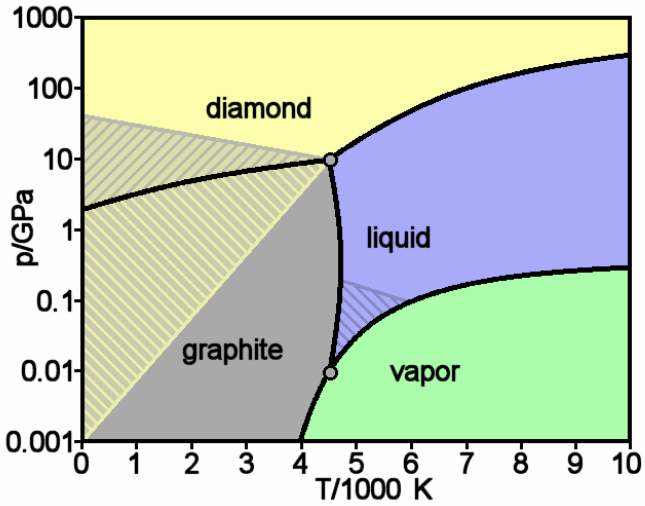

Fig. 1.1 Theoretically predicted phase diagram of carbon [20].

The different forms or allotropes of carbon include the hardest naturally occurring substance, diamond, and also one of the softest known substances, graphite. Moreover, it has an affinity for bonding with other small atoms, including other carbon atoms, and is capable of forming multiple stable covalent bonds with such atoms. As a result, carbon is known to form almost ten million different compounds-the large majority of all chemical compounds [20]. Carbon also has the highest sublimation point of all elements. At atmospheric pressure it has no melting point as its triple point is at 10.8 ± 0.2 MPa and 4,600 ± 300 K (~4,330 °C or 7,820 °F) [21, 22], so it sublimes at about 3,900 K [19, 23].

Carbon is well known to form distinct solid state allotropes with diverse structures and properties ranging from sp^3 hybridized diamond to sp^2 hybridized graphite. Mixed states are also possible and form the basis of amorphous carbon, diamondlike carbon, and nanocrystalline

diamond. Diamond is a metastable form of carbon that possesses a three-dimensional cubic lattice with a lattice constant of 0.357 nm and C–C bond length of 0.154 nm. In contrast, graphite is the most thermodynamically stable form of carbon at room temperature and consists of a layered two-dimensional structure where each layer possesses a hexagonal honeycomb structure of sp^2 bonded carbon atoms with a C–C bond length of 0.142 nm. These single atom thick layers (i.e., graphene layers) interact via noncovalent van der Waals forces with an interlayer spacing of 0.335 nm. The weak interlayer bonding in graphite implies that single graphene layers can be exfoliated via mechanical or chemical methods as will be outlined in detail below. Graphene is often viewed as the two-dimensional building block of other sp^2 hybridized carbon nanomaterials in that it can be conceptually rolled or distorted to form carbon nanotubes and fullerenes. [11]

Fullerenes are the zero-dimensional form of graphitic carbon that can be visualized as an irregular sheet of graphene being curled up into a sphere by incorporating pentagons in its structure. Fullerenes come in various forms and sizes ranging from 30 to 3000 carbon atoms. As a fullerene is elongated in one dimension, it approaches the structure of a CNT. Conceptually, CNTs are seamless cylinders of single or few layered graphene with a high aspect ratio (i.e. length to diameter ratio) that ranges from 10^2 to 10^7. The structure, diameter, and electronic type of a single-walled carbon nanotube (SWCNT) are determined by the chiral vector (i.e., roll-up vector) that defines the circumference of the SWCNT with respect to the graphene lattice (Fig. 1.2) [24]. Multi-walled carbon nanotubes (MWCNTs) consist of nested, concentric shells of SWCNTs with a spacing between individual walls of 0.34 nm.

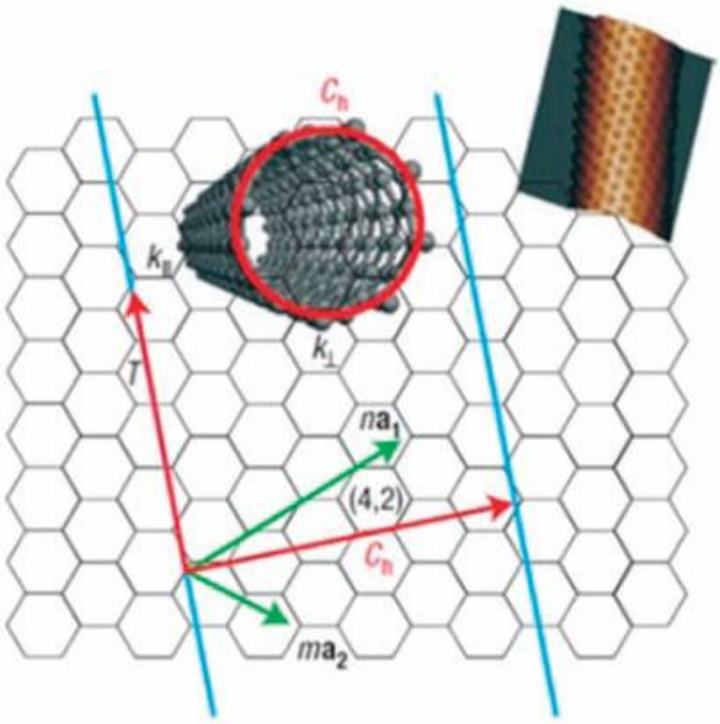

Fig. 1.2 A schematic of the lattice structure of graphene. Wrapping a rectangular section of graphene along the chiral vector (C_h) conceptually produces a SWCNT [11, 24].

1.3 Carbon nanotubes

CNTs are allotropes of carbon with a cylindrical nanostructure. Nanotubes have been constructed with length-to-diameter ratio of up to 132,000,000:1 [25], significantly larger than that of any other material. These cylindrical carbon molecules have unusual properties, which are valuable for nanotechnology, electronics, optics and other fields of materials science and technology. In particular, owing to their extraordinary thermal conductivity and mechanical and electrical properties, CNTs find applications as additives to various structural materials. [26]

1.3.1 Discovery of CNTs

In 1952, L. V. Radushkevich and V. M. Lukyanovich published clear images of 50 nanometer diameter tubes made of carbon in the Soviet Journal of Physical Chemistry [27]. This discovery

was largely unnoticed, as the article was published in the Russian language, and Western scientists' access to Soviet press was limited during the Cold War. It is likely that carbon nanotubes were produced before this date, but the invention of the transmission electron microscope (TEM) allowed direct visualization of these structures.

A paper by Oberlin, Endo, and Koyama published in 1976 clearly showed hollow carbon fibers with nanometer-scale diameters using a vapor-growth technique [28]. Additionally, the authors show a TEM image of a nanotube consisting of a single wall of graphene. Later, Endo has referred to this image as a single-walled nanotube [29].

In 1979, John Abrahamson presented evidence of carbon nanotubes at the 14th Biennial Conference of Carbon at Pennsylvania State University. The conference paper described carbon nanotubes as carbon fibers that were produced on carbon anodes during arc discharge. A characterization of these fibers was given as well as hypotheses for their growth in a nitrogen atmosphere at low pressures.[30]

In 1981, a group of Soviet scientists published the results of chemical and structural characterization of carbon nanoparticles produced by a thermocatalytical disproportionation of carbon monoxide. Using TEM images and XRD patterns, the authors suggested that their “carbon multi-layer tubular crystals” were formed by rolling graphene layers into cylinders. They speculated that by rolling graphene layers into a cylinder, many different arrangements of graphene hexagonal nets are possible. They suggested two possibilities of such arrangements: circular arrangement (armchair nanotube) and a spiral, helical arrangement (chiral tube).[31]

In 1987, Howard G. Tennett of Hyperion Catalysis was issued a U.S. patent for the production of "cylindrical discrete carbon fibrils" with a "constant diameter between about 3.5 and about 70 nanometers..., length 102 times the diameter, and an outer region of multiple essentially

continuous layers of ordered carbon atoms and a distinct inner core...."[29]

Sumio Iijima's discovery of multi-walled carbon nanotubes in the insoluble material of arc-burned graphite rods in 1991 [32] and Mintmire, Dunlap, and White's independent prediction that if single-walled carbon nanotubes could be made, then they would exhibit remarkable conducting properties [33] helped create the initial buzz that is now associated with carbon nanotubes. Nanotube research accelerated greatly following the independent discoveries [34, 35] by Bethune at IBM [29] and Iijima at NEC of single-walled carbon nanotubes and methods to specifically produce them by adding transition-metal catalysts to the carbon in an arc discharge. The arc discharge technique was well-known to produce the famed Buckminster fullerene on a preparative scale [36], and these results appeared to extend the run of accidental discoveries relating to fullerenes. The original observation of fullerenes in mass spectrometry was not anticipated [37], and the first mass-production technique by Krätschmer and Huffman was used for several years before realizing that it produced fullerenes [36].

The discovery of nanotubes remains a contentious issue. Many believe that Iijima's report in 1991 is of particular importance because it brought carbon nanotubes into the awareness of the scientific community as a whole.[38]

1.3.2 Structure of CNTs

CNTs can be constructed in two basic forms, SWCNTs and MWCNTs. SWCNTs consist of a single tube of graphene sheet which is made up of benzene type hexagonal rings of carbon atoms (Fig. 1.3), whereas MWCNTs are composed of several concentric tubes of graphene fitted one inside the other [39, 40]. The diameter of CNTs varies from a few nanometres in the case of SWCNTs to several tens of nanometres in the case of MWCNTs. The lengths of the CNTs are usually in the micrometre range [41].

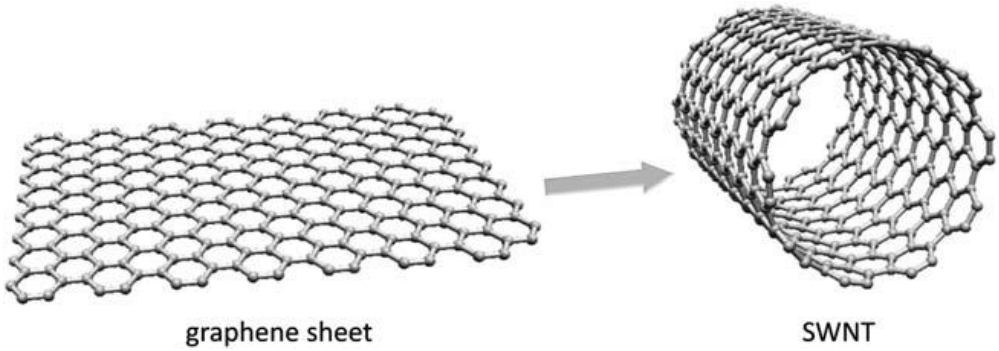

Fig. 1.3 Wrapping of graphene sheet to form SWCNT [40].

In addition to the two different basic structures, there are three different possible types of carbon nanotubes. These three types of CNTs are armchair carbon nanotubes, zigzag carbon nanotubes, and chiral carbon nanotubes. The difference in these types of carbon nanotubes are created depending on how the graphite is "rolled up" during its creation process. The choice of rolling axis relative to the hexagonal network of the grapheme sheet and the radius of the closing cylinder allows for different types of SWCNTs [39].

The chiral vector is represented by a pair of indices, n and m, where these two integers correspond to the number of unit vectors along the two directions in the honeycomb crystal lattice of grapheme. When $m = 0$ the nanotube is called "zigzag", when $n = m$ the nanotube is called "armchair", and all other configuration are designated as chiral [42-44]. Fig. 1.4 and Fig. 1.5 show the three different types of SWCNTs: armchair, zigzag, and chiral [40, 43].

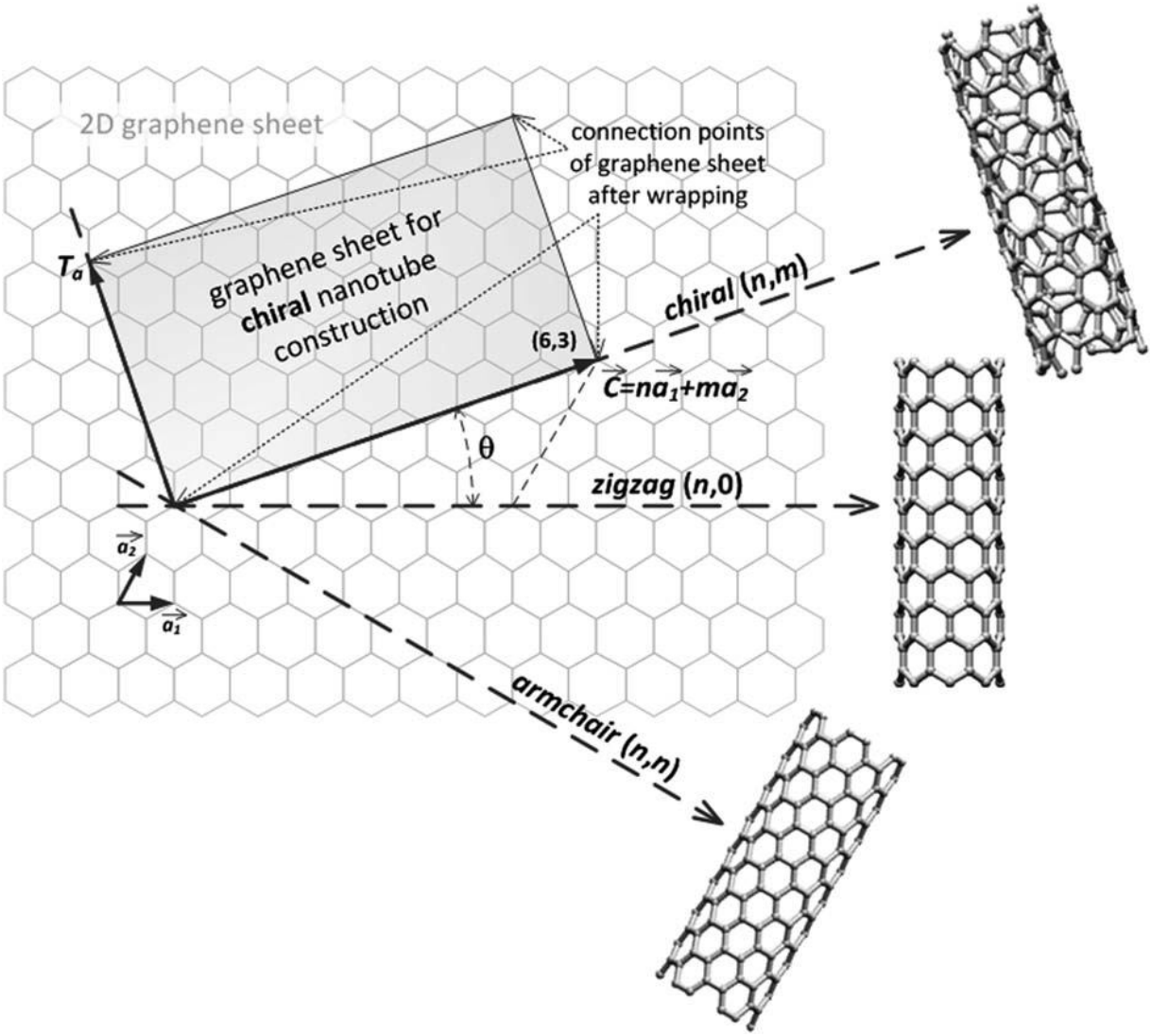

Fig. 1.4 The principle of CNT construction from graphene sheet along the chiral vector [40].

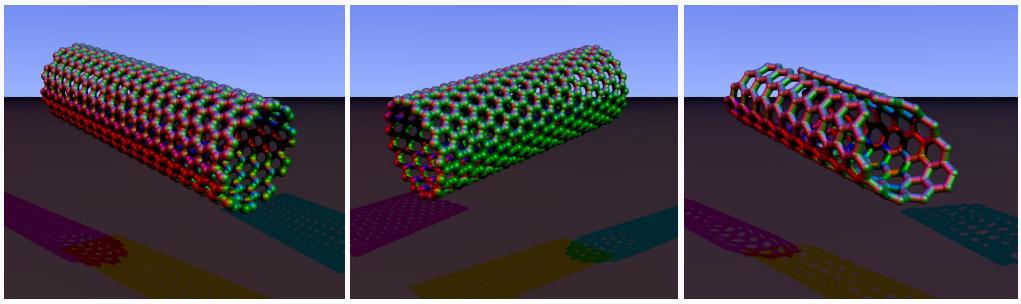

Fig. 1.5 Three types of SWCNTs: (a) Armchair (*n*,*n*), (b) Zigzag (*n*,0) and (c) Chiral (*n*,*m*) [29].

1.3.3 Properties of CNTs

1) Mechanical properties

The strength of the sp^2 carbon-carbon bonds gives carbon nanotubes amazing mechanical properties. No previous material has displayed the combination of superlative mechanical, thermal, and electronic properties attributed to them. Their densities can be as low as 1.3 g/cm3(one-sixth of that of stainless steel). CNTs Young's moduli (measure of material stiffness) are superior to all carbon fibres with values greater than 1 TPa which is approximately 5x higher than steel [45]. However, their strength is what really sets them apart. Carbon nanotubes are the strongest materials ever discovered by mankind. The highest measured tensile strength or breaking strain for a carbon nanotube was up to 63 GPa which is around 50 times higher than steel [45]. Even the weakest types of carbon nanotubes have strengths of several GPa [39, 46]. Besides that, Standard SWCNTs can withstand a pressure up to 25 GPa without deformation [29].

2) Electrical properties

Because of the symmetry and unique electronic structure of graphene, the structure of a nanotube strongly affects its electrical properties. for a given (n,m) nanotube, if $n = m$, the nanotube is metallic; if $n - m$ is a multiple of 3, then the nanotube is semiconducting with a very small band gap, otherwise the nanotube is a moderate semiconductor. Thus all armchair ($n = m$) nanotubes are metallic, and nanotubes (6,4), (9,1), etc. are semiconducting [47]. Semiconducting nanotubes have bandgaps that scale inversely with diameter, ranging from approximately 1.8 eV for very small diameter tubes to 0.18 eV for the widest possible stable SWCNT [48].

3) Thermal properties

All nanotubes are expected to be very good thermal conductors along the tube, exhibiting a

property known as "ballistic conduction", but good insulators laterally to the tube axis. Measurements show that a SWCNT has a room-temperature thermal conductivity along its axis of about 3500 $W \cdot m^{-1} \cdot K^{-1}$ [49]; compare this to copper, a metal well known for its good thermal conductivity, which transmits 385 $W \cdot m^{-1} \cdot K^{-1}$. A SWCNT has a room-temperature thermal conductivity across its axis (in the radial direction) of about 1.52 $W \cdot m^{-1} \cdot K^{-1}$ [50], which is about as thermally conductive as soil. The temperature stability of carbon nanotubes is estimated to be up to 2800℃ in vacuum and about 750℃ in air [51].

1.3.4 Applications of CNTs

Nowadays, various prototype electronic devices have been developed using single and multi-walled CNTs.

1) CNTs for electronic and optoelectronic applications

The diverse range of CNT electronic properties as a function of their chiral vector coupled with their quasi-one dimensional structure presents a number of attractive opportunities for electronic applications. For example, semiconducting CNTs are promising channel materials in field-effect transistors (FETs), whereas metallic CNT thin films are potentially useful as transparent conductors [52].

When a potential is applied between a CNT surface and an anode, electrons are easily emitted from their tips (electron tunneling from the tips into the vacuum) due to curvature (presence of pentagons) [53] or dangling bonds (oxidized tips) [54]. Using this principle, CNTs can be used as efficient field emission sources for the fabrication of multiple electronic devices [55] such as flat panel displays, intense light sources or bright lamps [56-58], and X-ray sources [59].

The unique optical properties of CNTs also present opportunities for novel optoelectronic

devices. Semiconducting CNTs are direct band gap materials that possess free electron–hole pair excitations as well as strongly bound electron–hole pair states called excitons [60, 61]. It have been incorporated in a variety of optoelectronic devices such as light detectors, light emitters, and transparent conductors [24, 62, 63]. Van Hove singularities in the one-dimensional density of states and strongly bound excitons make CNTs interesting candidates for optoelectronics [64].The exciton binding energy depends on the diameter of CNTs [65, 66] as well as on the dielectric constant of the surrounding environment [66]. Excitons in CNTs can be created optically as well as electrically, and the corresponding radiative recombination results in photoluminescence and electroluminescence in CNTs. Electroluminescence in CNTs has been demonstrated at room temperature in ambipolar FETs [67] as well as through impact excitation in unipolar FETs [68].

2) CNTs for photovoltaic applications

The unique optical, electrical, chemical, and mechanical properties of CNTs make them enticing materials for photovoltaic applications. CNTs possess a wide range of direct bandgaps matching the solar spectrum, strong photoabsorption, from infrared to ultraviolet, and high carrier mobility and reduced carrier transport scattering, which make themselves ideal photovoltaic material. Photovoltaic effect can be achieved in ideal SWCNTs diodes. Individual SWCNTs can form ideal p-n junction diodes [69].Furthermore, the optical excitation of strongly bound excitons in semiconducting SWCNTs at room temperature shows similarities to the conjugated organic molecules and polymers that are commonly employed in organic photovoltaics [61, 70]. In addition, CNTs show significantly higher carrier mobility and reduced trap density compared to organic electronic materials. Consequently, CNTs are gaining popularity as components of photovoltaic devices [71, 72].

3) CNTs for sensing applications

The fabrication of chemical sensors using CNTs can also be exploited so that novel and low-cost technologies can emerge in the near future. Lieber et al. [73] were the first to demonstrate that it is possible to sense functional chemical groups attached at the nanotube ends using chemical force microscopy (CFM) techniques. Subsequently, Dai et al. [74] carried out toxic gas sensing experiments using pellets of SWCNTs. The authors were able to detect low gas concentrations (e.g., ppm) of nitrogen dioxide (NO_2) or ammonia (NH_3), by observing strong and drastic transport changes in the SWCNT material [74]. Therefore, it is possible to construct various types of nanotube composite pellets that are sensitive to gases and could be used to monitor leaks in chemical plants. One report of gas sensors based on single CNT FETs was also made by Kong et al. in 2000 [74]. Large shifts in threshold voltages were observed in the negative and positive directions upon exposure to NH_3 and NO_2, respectively [43].

In addition to gas sensing, SWCNTs can also be used as sensitive environmental pressure sensors [75].Wood and Wagner [75] noted that SWCNTs are very sensitive to liquid immersion or polymer embedding [76] because the nanotubes slightly deform in the presence of different liquid media. Sensitive visible radiation and magnetic sensors could also be developed using CNT materials.

4) CNTs for electrochemical applications

Due to the large surface area observed in MWCNT and bundles of MWCNTs, as well as their high electrical conductivity, CNTs are excellent candidates for application involving electrochemical devices [57]. For instance, the fabrications of supercapacitors and electrochemical actuators that could be used as artificial muscles are further alternatives for CNT applications [43].

The exceptional electrical and mechanical properties of CNTs have made them alternatives to

the traditional electrical actuators for both microscopic and macroscopic applications. CNTs are very good conductors of both electricity and heat, and they are also very strong and elastic molecules in certain directions. These properties are difficult to find in the same material and very needed for high performance actuators. For current CNTs actuators, MWCNTs and bundles of MWCNTs have been widely used mostly due to the easiness of handling and robustness. Solution dispersed thick films and highly ordered transparent films of CNTs have been used for the macroscopic applications [77].

5) CNTs for gas and hydrogen storage applications

In addition to being able to store electrical energy, there has been some research in using carbon nanotubes to store hydrogen (H_2) to be used as a fuel source. By taking advantage of the capillary effects of the small carbon nanotubes, it is possible to condense gases in high density inside single-walled nanotubes. This allows for gases, most notably H_2, to be stored at high densities without being condensed into a liquid [78]. It is important to emphasize that H_2 storage in CNTs may be used on vehicles in place of gas fuel cells for a hydrogen-powered car. Unfortunately, there has been controversy on the high H_2 storage capacity in CNTs (from 0.1 to 66 wt%) [79].

1.4 Graphene

The youngest representative of synthetic carbon allotropes is 2D graphene. In graphene, carbon atoms are densely packed in a regular sp^2-bonded atomic-scale chicken wire (hexagonal) pattern (Fig. 1.6). Graphene can be described as a one-atom thick layer of graphite. It is the basic structural element of other allotropes, including graphite, carbon nanotubes and fullerenes [80]. Unlike most materials in condensed matter physics, where the Schrodinger equation can be used to

describe their electronic properties, for graphene, the charge carriers mimic relativistic particles and can thus be described using the Dirac equation and this allows access to quantum electrodynamics in a simple condensed matter experiment [81]. The scalability of graphene devices to nanodimensions makes it a promising candidate for applications, because of its ballistic transport at room temperature combined with chemical and mechanical stability. Remarkable properties extend to bilayer and fewlayer graphene [82].

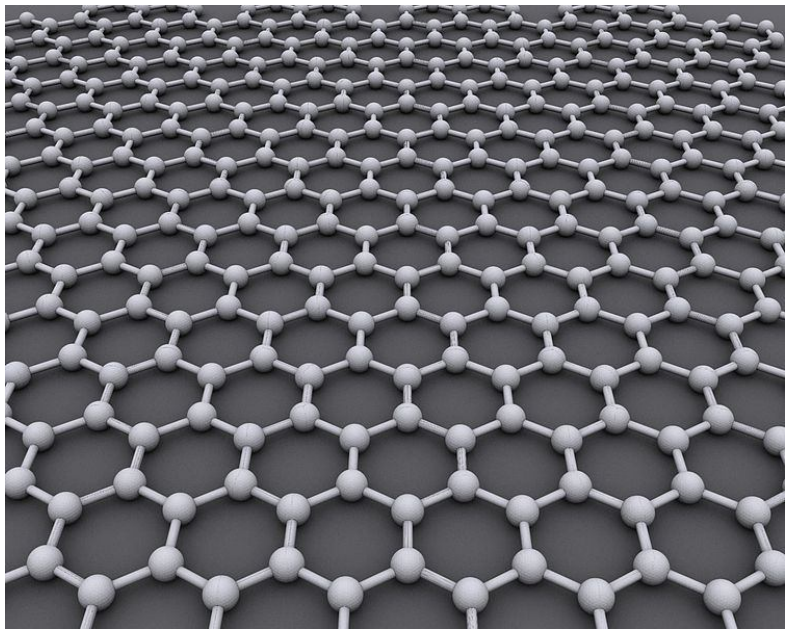

Fig. 1.6 Schematic of graphene: an atomic-scale honeycomb lattice made of carbon atoms [80].

High-quality graphene is strong, light, nearly transparent and an excellent conductor of heat and electricity. Its interactions with other materials and with light and its inherently 2D nature produce unique properties, such as the bipolar transistor effect, ballistic transport of charges and large quantum oscillations.

At the time of its isolation in 2004 [2, 83], researchers studying carbon nanotubes were already familiar with graphene's composition, structure and properties, which had been calculated decades earlier. The combination of familiarity, extraordinary properties, surprising ease of

isolation and unexpectedly high quality of the obtained graphene enabled a rapid increase in graphene research. Andre Geim and Konstantin Novoselov won the Nobel Prize in Physics in 2010 "for groundbreaking experiments regarding the 2D material graphene" [84].

1.4.1 Properties of graphene

1) Mechanical properties

Due to the strength of its 0.142 nm-long carbon bonds, graphene appeared to be one of the strongest materials known with a breaking strength over 100 times greater than a hypothetical steel film of the same thickness [85], with a Young's modulus (stiffness) of 1 Tpa [14]. Not only is graphene extraordinarily strong, it is also very light at 0.77 milligrams per square meter. It is often said that a single sheet of graphene (being only 1 atom thick), sufficient in size enough to cover a whole football field, would weigh under 1 single gram [86]. What's more, graphene also contains elastic properties, being able to retain its initial size after strain [86]. You can stretch graphene up to 20% of its initial length. It is expected that graphene's mechanical properties will find applications into making a new generation of super strong composite materials and along combined with its optical properties, making flexible displays [87].

2) Chemical properties

Graphene is the only form of carbon (and generally all solid materials) in which each single atom is in exposure for chemical reaction from two sides due to the 2D structure. It is known that carbon atoms at the edge of graphene sheets have special chemical reactivity, and graphene has the highest ratio of edgy carbons. In addition, various types of defects within the sheet, which are very common, increase the chemical reactivity [88]. Similar to the surface of graphite, graphene can adsorb and desorb various atoms and molecules (for example, NO_2, NH_3, ⋯) [87].The onset

temperature of reaction between the basal plane of single-layer graphene and oxygen gas is below 260℃ [89] and the graphene burns at very low temperature (~350 °C) [90]. In fact, graphene is chemically the most reactive form of carbon, owing to the lateral availability of carbon atoms.

3) Electronic properties

Intrinsic graphene is a semi-metal or zero-gap semiconductor with very high electrical conductivity [86]. Carbon atoms have a total of 6 electrons, 2 in the inner shell and 4 in the outer shell. The 4 outer shell electrons in an individual carbon atom are available for chemical bonding, but in graphene, each atom is connected to 3 other carbon atoms on the 2D plane, leaving 1 electron freely available in the third dimension for electronic conduction. These highly-mobile electrons are called pi (π) electrons and are located above and below the graphene sheet. These pi orbitals overlap and help to enhance the carbon to carbon bonds in graphene. Fundamentally, the electronic properties of graphene are dictated by the bonding and anti-bonding (the valance and conduction bands) of these pi orbitals.

It has proved that at the Dirac point in graphene, electrons and holes have zero effective mass. This occurs because the energy – movement relation (the spectrum for excitations) is linear for low energies near the 6 individual corners of the Brillouin zone [80]. These electrons and holes are known as Dirac fermions, or Graphinos, and the 6 corners of the Brillouin zone are known as the Dirac points [91]. The equation describing the electrons' linear dispersion relation is $E = \hbar v_F \sqrt{k_x^2 + k_y^2}$, where the Fermi velocity $v_F \sim 10^6$ m/s, and the wavevector k is measured from the Dirac points (the zero of energy is chosen here to coincide with the Dirac points) [92]. Due to the zero density of states at the Dirac points, electronic conductivity is actually quite low. However, the Fermi level can be changed by doping (with electrons or holes) to create a material that is potentially better at conducting electricity than, for example, copper at room temperature [86].

4) Optical properties

Graphene's ability to absorb a rather large 2.3% of white light is also a unique and interesting property, especially considering that it is only 1 atom thick. This is due to its aforementioned electronic properties; the electrons acting like massless charge carriers with very high mobility [86, 87, 93]. A few years ago, it was proved that the amount of white light absorbed is based on the Fine Structure Constant, rather than being dictated by material specifics. Adding another layer of graphene increases the amount of white light absorbed by approximately the same value (2.3%) [86].

5) Thermal properties [87]

Graphene is a perfect thermal conductor. Its thermal conductivity at room temperature is much higher than the value observed in all the other carbon structures such as carbon nanotubes, graphite and diamond (> 5000 W/m/K).

The ballistic thermal conductance of graphene is isotropic, i.e. same in all directions. Similarly to all the other physical properties of this material, its 2D structure makes it particularly special. Graphite, the 3D version of graphene, shows a thermal conductivity about 5 times smaller (1000 Wm-1K-1). The phenomenon is governed by the presence of elastic waves propagating in the graphene lattice, called phonons.

The study of thermal conductivity in graphene may have important implications in graphene-based electronic devices. As devices continue to shrink and circuit density increases, high thermal conductivity, which is essential for dissipating heat efficiently to keep electronics cool, plays an increasingly larger role in device reliability.

1.4.2 Applications of graphene

1) Graphene for digital electronics applications

The high field effect mobility of graphene has inspired significant efforts to explore its utility for digital electronics. In principle, the high mobility allows faster switching circuits, and the ideal 2D structure enables ultimate scaling of the device channel [94]. The low contact resistance of graphene, in contrast to CNTs, also enables high conductance devices. However, the lack of a band gap and the resulting low on/off ratio (5–10) seriously compromises the prospects of graphene for digital electronics where an on/off ratio of 10^4–10^6 is desired. Graphene shows a minimum conductivity of 4–8 $e^2 h^{-1}$ even at zero carrier concentration (i.e., unbiased gate) and thus it cannot be turned off completely. Although the origin of the minimum conductivity is not completely understood [95, 96], it is widely accepted that graphene-based digital electronics will require a method to open a band gap in graphene.

2) Graphene for radio frequency electronic devices

It is desired for high speed radio frequency (RF) electronic devices that: short gate length, large transconductance, small contact resistance and drain current saturation. Graphene is an excellent candidate for the first three RF device requirements. As a true 2D material, graphene should be ideal in the limit of short gate length devices. Furthermore, high carrier mobility in graphene at room temperature (typically 10 000–20 000 $cm^2 V^{-1} s^{-1}$ on SiO_2) [97, 98] results in a normalized transconductance parameter of up to 7 ms [99], which is higher than the transconductance in state-of-the-art Si metal oxide semiconductor field effect transistors (MOSFETs) and GaAs high electron mobility transistors (HEMTs) [94]. The contact resistance of graphene (500–1000 Ω μ m [100]) is much smaller than that of a SWCNT (12.9 k Ω), but it is still

an order of magnitude higher than in Si MOSFETs and GaAs HEMTs [94]. On the other hand, the saturation velocity in graphene (4×10^7 cm s^{-1}) exceeds that of GaAs HEMTs and Si MOSFETs by approximately a factor of two [101].

3) Graphene for photovoltaic applications

Due to the lack of a band gap in graphene, it is not well-suited as an active layer material for efficient carrier generation and separation in photovoltaic devices. However, modern solar cells consist of an assembly of several layers such as transparent conducting electrodes and charge blocking interfacial layers. In this regard, the large conductivity and high transparency of single layer graphene make it a promising material for transparent conducting electrodes in OPVs. In addition, graphene and its chemically modified derivatives are potentially candidates for charge blocking interfacial layers [80, 102, 103].

4) Graphene for sensing applications

Like SWCNTs, every carbon atom in single-layer graphene is on the surface, which implies that its electronic properties should be sensitive to the surrounding environment. Consequently, the electrical conductivity of graphene is strongly modulated by adsorbates, providing clear opportunities for sensing. Graphene based electrochemical sensors have been achieved by researchers [104-106].

1.5 Carbon nanorods

Since Iijima discovered CNTs in 1991[32], other nanotubular structures have been an area of interest along the scientific community across the globe [107]. Nanowires, nanorods and nanobelts form an important class of 1D nanostructures, which provide models to study the relationship between electrical transport, optical and other properties with dimensionality and size confinement

[108]. This synthesis revolution led to a possible alternative of nanotubes for molecular electronics [109]. 1D carbon nanomaterials including carbon nanorods have attracted more attention not only due to their small dimension and unique electrical, chemical, mechanical properties, but also for their potential applications in various technologies [110, 111].

Carbon nanorods were produced using different synthesis routes such as vapour-liquid-solid growth, oxide-assisted growth, vapour-solid growth, carbothermal reactions, template-based synthesis, solution-liquid-solid process and sovothermal synthesis [107, 108]. Besides these methods, M. Venkateswer Rao and Vivek Dhand *et al.* synthesized carbon nanorods using a flame reactor with/without catalyst [107, 112]. X. Wang *et al.* reported a novel benzene-thermal-reduction-catalysis route to produce carbon nanorods in the presence of different catalysts at 200℃ [111].

What's more, Carbon nanorods can be synthesized via a "top-down" or "bottom-up" approach by using a hard template or seed mediation method, respectively. Whereas lithographic methods use a "top-down" miniaturization of patterns, the alternative approach of the "bottom-up" construction of objects has been suggested as a means to overcome the limitations of lithography [113]. Carbon nanorods can also be grown from the catalytic decomposition of certain hydrocarbons over small metal particles such as iron, cobalt, nickel, and some of their alloys [114, 115]. The diameter of the nanostructure is controlled by the size of the catalyst particle and can vary between 2 and 100 nm, and lengths ranging from 5 to 100 μm^3.

Recently, 1D tilted nanorods have attracted noticeable research interest due to their inherent anisotropic nature with tilted geometry. 1D carbon tilted nanorods were successfully synthesized by using a catalyst-assisted oblique angle deposition technique [116] and hot filament physical vapour deposition technique [117].

Due to the extraordinary combination of physical and chemical properties exhibited by carbon nanorods, which blends two properties that rarely coexist: high surface area and high electrical conductivity, which are the result of the unique stacking and crystalline order present within the structure, there are tremendous opportunities to exploit the potential of this form of carbon in a number of areas.

1.6 Thesis outline

In this thesis, we address the synthesis, characterization and applications of carbon nanomaterials, including carbon nanorods, nanosheets, nanohoneycombs and nanotubes. The potentials carbon nanomaterials as field electron emitting materials and humidity sensors are demonstrated.

Following is a brief outline of our present work:

In Chapter 2, an overview of the synthesis and characterization techniques, which have been used in this thesis, is presented. The experimental setups and basic physical processing with different synthesis techniques (PLD, DC/RF sputtering, HFPVD), which are installed in our laboratory, are described. Various general characterization techniques and tools for the study of the morphologic surface, chemical compositions and structural, mechanical, electronic and sensing properties of nano-materials are also introduced.

In Chapter 3, we address a simple approach for synthesizing well aligned one-dimensional tilted micro- and nanorods hybrid carbon structure at different substrate temperatures and incident angles of carbon source beam by hot filament physical vapor deposition technique. The morphologic surfaces and bond structures of the oblique carbon rod-like structures were investigated by scanning electron microscopy, field emission scanning electron microscopy, transmission electron diffraction and Raman scattering spectroscopy. The field emission

measurement of the fabricated samples indicates that the sample grown at higher temperature has better field emitting behaviour.

In Chapter 4, carbon nanosheets and nanohoneycombs were synthesized on Si substrates using a hot filament physical vapor deposition technique under methane ambient and vacuum, respectively. The four-point Au electrodes are then sputtered on the surface of the nanostructured carbon (n-C) films to form prototypical humidity sensors. The sensing properties of prototypical sensors at different temperature, humidity, direct current (DC), and alternative current (AC) voltage were characterized. Linear sensing response of sensors to relative humidity ranging from 11% to 95% is observed at room temperature. Experimental data indicate that the carbon nanosheets based sensors exhibit an excellent reversible behavior and long-term stability. It also has higher response than that of the humidity sensor with carbon nanohoneycombs materials.

In Chapter 5, conducting composite films containing CNTs were prepared by using the biopolymer kappa-carrageenan as a dispersant. Films prepared by vacuum filtration exhibited higher conductivity compared to those prepared by evaporative casting. All composite films displayed sensitivity to water vapour, but MWCNTs films were more sensitive than SWCNTs films.

In Chapter 6, we summarize the present thesis work. Some important issues for further study in current research topic are presented.

1.7 References

[1] N. Martin, Dirk M. Guldi and L. Echegoyen, *Chem. Commun.* 47: 604–605 (2011)

[2] Dirk M. Guldi and V. Sgobba, *Chem. Commun.* 47: 606–610 (2011)

[3] P.G. Soukiassian, M.S. Ramachandra Rao, *J. Phys. D: Appl. Phys.* 43: 370301 (2010)

[4] M.C. Rocco, *National Science Foundation, Official who oversees the nanotechnology initiative* 285: 3 (2001)

[5] N. Taniguchi, *On the basic concept of nanotechnology*. *Proc.* ICPB Tokyo (1974)

[6] P.M. Ajayan and T.W. Ebbesen, *Rep. Prog. Phys.* 60: 1025-1065 (2003)

[7] R. Feynman, *Engineering & Science Magazine*, California, Institute of Technology, USA (1960)

[8] K.E. Drexler. *Engines of creation: the coming era of nanotechnology*, Doubleday (1986) (ISBN: 0-385-19973-2).

[9] K.E. Drexler. *Nanosystems: molecular machinery, manufacturing and computation*. New York: Wiley (1992) (ISBN: 0-471-57518-6).

[10] A.G. Mamalis, L.O.G. Vogtlander, and A. Markopoulos, *Precision Enginerring* 28: 16 (2004)

[11] D. Jariwala, V.K. Sangwan, L.J. Lauhon, T.J. Marks and M.C. Hersam, *Chem. Soc. Rev.* 42: 2824-2860 (2013)

[12] M.M. J. Treacy, T.W. Ebbesen and J.M. Gibson, *Nature* 381: 678-680 (1996)

[13] E.W. Wong, P.E. Sheehan and C.M. Lieber, *Science* 277: 1971-1975 (1997)

[14] G. Lee, X. Wei, J.W. Kysar, J. Hone, *Science* 321: 385-388 (2008)

[15] L.A. Ponomarenko, F. Schedin, M.I. Katsnelson, R. Yang, E.W. Hill, K.S. Novoselov, A.K. Geim, *Sicence* 320: 356 (2008)

[16] F.P. Bundy, *Physica A* 156: 169 (1989)

[17] J. Steinback et al., *J. Appl. Phys.* 58 (11): 4374 (1985)

[18] A.G. Whittaker , *Science* 200: 763 (1978)

[19] J.M. Zazula, LHC Project Note 78/97, 1997

[20] Carbon. From Wikipedia: http://en.wikipedia.org/wiki/Carbon

[21] D. Haaland, *Carbon* 14 (6): 357 (1976)

[22] A. Savvatimskiy, *Carbon* 43 (6): 1115 (2005)

[23] A.G. Whittaker, *Nature* 276: 695–696 (1978)

[24] P. Avouris, Z. Chen and V. Perebeinos, *Nat. Nanotechnol.* 2: 605–615 (2007)

[25] X. Wang, Q. Li, J. Xie, Z. Jin, J. Wang, Y. Li, K. Jiang, S. Fan, *Nano Letters* 9 (9): 3137–3141 (2009)

[26] S. Gullapalli, M.S. Wong, *Chemical Engineering Progress* 107 (5): 28–32 (2011)

[27] L.V. Radushkevich, *Journal of Physical Chemistry* (in Russian) 26: 88–95 (1952)

[28] A. Oberlin, M. Endo, T. Koyama, *Journal of Crystal Growth* 32 (3): 335–349 (1976)

[29] Carbon nanotube. From Wikipedia: http://en.wikipedia.org/wiki/Carbon_nanotube

[30] J. Abrahamson, P.G. Wiles, B.L. Rhoades, *Carbon* 37 (11): 1873 (1999)

[31] Izvestiya Akademii Nauk SSSR, *Metals* 3 (in Russian): 12–17 (1982)

[32] S. Iijima, *Nature* 354: 56–58 (1991)

[33] J.W. Mintmire, B.I. Dunlap, C.T. White, *Phys. Rev. Lett.* 68 (5): 631–634(1992)

[34] D.S. Bethune, C.H. Kiang, M.S. De Vries, G. Gorman, R. Savoy, J. Vazquez, R. Beyers, *Nature* 363: 605–607 (1993)

[35] S. Iijima, Toshinari, Ichihashi, *Nature* 363: 603–605 (1993)

[36]W. Krätschmer, Lowell D. Lamb, K. Fostiropoulos, Donald R. Huffman, *Nature* 347: 354–358 (1990)

[37] H.W. Kroto, J.R. Heath, S.C. O'Brien, R.F. Curl, R.E. Smalley, *Nature* 318: 162–163 (1985)

[38] M. Monthioux, V. Kuznetsov, *Carbon* 44 (9): 1621 (2006)

[39] N. Saifuddin, A.Z. Raziah, and A.R. Junizah, *Journal of Chemistry* 2013: 676815 (2013)

[40] J. Prasek, J. Drbohlavova, J. Chomoucka, J. Hubalek, O. Jasek, V. Adam and R. Kizek, *J. Mater. Chem.* 21: 15872–15884 (2011)

[41] *Biosensing Using Nanomaterials*, ed. A. Merkoci, Wiley, New Jersey, 2009

[42] M.S. Dresselhaus, G.Dresselhaus, and A. Jorio, *Annu. Rev. Mater.Res.* 34: 247–278 (2004)

[43] M. Terrones, *Annu. Rev. Mater.Res.* 33: 419–501 (2003)

[44] M. Zhang and J. Li, *Materials Today* 12: 12–18, (2009)

[45] M.F. Yu, B.S. Files, S. Arepalli, and R.S. Ruoff, *Physical Review Letters* 84: 5552–5555 (2000)

[46] S. Xie, W. Li, Z. Pan, B. Chang, and S. Lianfeng, *Journal of Physics and Chemistry of Solids* 61: 1153–1158 (2000)

[47] X. Lu, Z. Chen, *Chemical Reviews* 105 (10): 3643–3696 (2005)

[48] J.A. Elliott, J.K.W. Sandler, A.H. Windle, R.J. Young, and M.S.P. Shaffer, *Physical Review Letters* 92: 1–4 (2004)

[49] E. Pop, D. Mann, Q. Wang, K. Goodson, H. Dai, *Nano Letters* 6 (1): 96–100 (2005)

[50] S. Sinha, S. Barjami, G. Iannacchione, A. Schwab, G. Muench, *Journal of Nanoparticle Research* 7 (6): 651–657 (2005)

[51] E. Thostenson, C. Li, T. Chou, *Composites Science and Technology* 65: 491–516 (2005)

[52] A.D. Franklin, M. Luisier, S.J. Han, G. Tulevski, C.M. Breslin, L.Gignac, M.S. Lundstrom and W. Haensch, *Nano Lett.* 12: 758–762 (2012)

[53] J.M. Bonard, *et al.*, *Phys. Rev. Lett.* 81:1441–1444 (1998)

[54] Y. Saito, *et al.*, *Nature* 389:554–555 (1997)

[55] W.A. De Heer, *et al.*, *Science* 268: 845–847 (1995)

[56] D. Rotman, *Tech. Rev.* 38–45 (2002)

[57] R.H. Baughman, A.A. Zakhidov, W.A. De Heer, *Science* 297: 787–792 (2002)

[58] H. Sugie, M. Tanemura, V. Filip, K. Iwata, K. Takahashi, F. Okuyama, *Appl. Phys. Lett.* 78: 2578–2580 (2001)

[59] G.Z. Yue, *et al.*, *Appl. Phys. Lett.* 81: 355–357 (2002)

[60]F. Wang, G. Dukovic, L.E. Brus and T.F. Heinz, *Science* 308: 838–841 (2005)

[61] M.J. O'Connell, *et al*., *Science* 297: 593–596 (2002)

[62] P. Avouris, M. Freitag and V. Perebeinos, *Nat. Photonics* 2: 341–350 (2008)

[63] H. Liangbing, L. Jianfeng, L. Jun, G. George and M. Tobin, *Nanotechnology* 21: 155202 (2010)

[64] S.M. Bachilo, M.S. Strano, C. Kittrell, R.H. Hauge, R.E. Smalley and R.B. Weisman, *Science* 298: 2361–2366 (2002)

[65] G. Dukovic, F. Wang, D. Song, M.Y. Sfeir, T.F. Heinz and L.E. Brus, *Nano Lett.* 5: 2314–2318 (2005)

[66] V. Perebeinos, J. Tersoff and P. Avouris, *Phys. Rev. Lett.* 92: 257402 (2004)

[67] J.A. Misewich, R. Martel, P. Avouris, J.C. Tsang, S. Heinze and J. Tersoff, *Science* 300: 783–786 (2003)

[68] J. Chen, V. Perebeinos, M. Freitag, J. Tsang, Q. Fu, J. Liu and P. Avouris, *Science* 310: 1171–1174 (2005)

[69] J.U. Lee, *Appl. Phys. Lett.* 87 (3): 073101 (2003)

[70] G.D. Scholes and G. Rumbles, *Nat. Mater.* 5: 683–696 (2006)

[71] A.C. Dillon, *Chem. Rev.* 110: 6856–6872 (2010)

[72] D.D. Tune, B.S. Flavel, R. Krupke and J.G. Shapter, *Adv.Energy Mater.* 2: 1043–1055 (2012)

[73] S.S. Wong, E. Joselevich, A.T. Woolley, C.L. Cheung, C.M. Lieber, *Nature* 394: 52–55 (1998)

[74] J. Kong *et al.*, *Science* 287:622–625 (2000)

[75] J.R. Wood, H.D.Wagner, *Appl. Phys. Lett.* 76: 2883–85 (2000)

[76] J.R. *Wood, et al*., *Phys. Rev. B* 62: 7571–7575 (2000)

[77] Carbon nanotube actuators. From Wikipedia: http://en.wikipedia.org/wiki/Carbon_nanotube_actuators

[78] A.C. Dillon, K.M. Jones, T.A. Bekkedahl, C.H. Klang, D.S. Bethune, and M.J. Heben, *Nature* 386: 377–379 (1997)

[79] M. Hirscher, *et al.*, *J. Alloys Comp.* 330: 654–658 (2002)

[80] Graphene. From Wikipedia: http://en.wikipedia.org/wiki/Graphene

[81] Y. Zhang, Y.W. Tan, H.L. Stormer, P. Kim, *Nature* 438: 201 (2005)

[82] A. Geim, K.S. Novoselov, *Nat Mater* 6: 183 (2007)

[83] "This Month in Physics History: October 22, 2004: Discovery of Graphene". *APS News*. Series II 18 (9): 2. 2009

[84] "The Nobel Prize in Physics 2010". The Nobel Foundation

[85] “2010 Nobel Physics Laureates", nobelprize.org

[86] Jesus de La Fuente, Properties Of Graphene: http://www.graphenea.com/pages/graphene-properties

[87] Graphene: World-leading Research and Development: http://www.graphene.manchester.ac.uk/story/properties/

[88] P.A. Denis, F. Iribarne, *Journal of Physical Chemistry C* 117 (37): 19048 (2013)

[89] Y. Yamada, *et al.*, *Journal of American Chemical Society* 136 (6): 2232 (2014)

[90] A. Eftekhari, P. Jafarkhani, *Journal of Physical Chemistry C* 117 (48): 25845(2013)

[91] G.W. Semenoff, *Physical Review Letters* 53 (26): 2449 (1984)

[92] P. Avouris, Z. Chen, V. Perebeinos, *Nature Nanotechnology* 2 (10): 605–615 (2007)

[93] A.B. Kuzmenko, E. Van Heumen, F. Carbone, D. Van Der Marel, *Physical Review Letters* 100 (11): 117401 (2008)

[94] F. Schwierz, *Nat. Nanotechnol.* 5: 487–496 (2010)

[95] A.H. Castro Neto, F. Guinea, N.M.R. Peres, K.S. Novoselov and A.K. Geim, *Rev. Mod. Phys.* 81: 109–162 (2009)

[96] S. Das Sarma, S. Adam, E.H. Hwang and E. Rossi, *Rev. Mod. Phys.* 83: 407–470 (2011)

[97] K.S. Novoselov, A.K. Geim, S.V. Morozov, D. Jiang, Y. Zhang, S.V. Dubonos, I.V. Grigorieva and A.A. Firsov, *Science* 306: 666–669 (2004)

[98] J.H. Chen, C. Jang, S. Xiao, M. Ishigami and M.S. Fuhrer, *Nat. Nanotechnol.* 3: 206–209 (2008)

[99] H. Xu, Z. Zhang, H. Xu, Z. Wang, S. Wang and L.M. Peng, *ACS Nano* 5: 5031–5037 (2011)

[100] S. Russo, M.F. Craciun, M. Yamamoto, A.F. Morpurgo and S. Tarucha, *Phys. E* 42: 677–679 (2010)

[101] R.S. Shishir and D.K. Ferry, *J. Phys.: Condens. Matter* 21: 344201 (2009)

[102] F. Bonaccorso, Z. Sun, T. Hasan and A.C. Ferrari, *Nat. Photonics* 4: 611–622 (2010)

[103] X. Wan, G. Long, L. Huang and Y. Chen, *Adv. Mater.* 23: 5342–5358 (2011)

[104] M. Pumera, A. Ambrosi, A. Bonanni, E.L.K. Chng and H.L. Poh, Trac, *Trends Ana. Chem.* 29: 954–965 (2010)

[105] D.A.C. Brownson and C.E. Banks, *Analyst* 135: 2768–2778 (2010)

[106] Y. Shao, J. Wang, H. Wu, J. Liu, I.A. Aksay and Y. Lin, *Electroanalysis* 22: 1027–1036 (2010)

[107] Vivek Dhand, *et al.*, *Indian J. Eng. Mater. Sci.* 14: 235-239 (2007)

[108] C.N.R. Rao, F.L. Deepak, G. Gundiah and A. Govindaraj, *Prog. Solid State Chem.* 31: 5-147 (2003)

[109] M. Mannsberger, *et al.*, *Carbon* 42: 953-960 (2004)

[110] G.Y. Zhang, X. Jiang and E. Wang, *Science* 300:472 (2003)

[111] X.J. Wang, J. Lu, Y. Xie, G.A. Du, Q.X. Guo, S.Y. Zhang, *J. Phys. Chem. B* 106: 933-937 (2002)

[112] M.V. Rao, K. Amareshwari, V. Viditha, C. Mahender, V. Himabindu and Y. Anjaneyulu, *International Journal of Innovation and Applied Studies* 3: 1-5 (2013)

[113] I.W. Eugenii Katz, *ChemInform.* 43: 6042–6108 (2004)

[114] R.T.K. Baker and P.S. Harris, *Chemistry and Physics of Carbon* 14: 83 (1978)

[115] A. Oberlin, M. Endo and T. Koyama, *J. Cryst. Growth* 32: 335 (1976)

[116] H.X. Zhang and P.X. Feng, *J. Phys. D: Appl. Phys.* 42: 025406 (2009)

[117] J. Chu, X.Y. Peng, A. Aldalbahi, M. in het Panhuis, R. Velazquez and P.X. Feng, *J. Phys. D: Appl. Phys.* 45: 395102 (2012)

Chapter 2

Synthesis and characterization techniques

This chapter provides an overview of the synthesis and characterization techniques which can be used to synthesize carbon nanomaterials we installed in our laboratory, including the pulsed laser deposition (PLD), direct current/radio frequency (DC/RF) sputtering and hot filament chemical/physical vapour deposition (HFCVD/PVD) setups in our laboratory. The contents of this chapter include the experimental setups, basic physical processing in different synthesis techniques, and general characterization techniques for the study of the morphologic surface, chemical compositions and structural, mechanical, electronic and sensing properties of carbon nanomaterials.

2.1 PLD techniques

Laser was first demonstrated in 1960 by Maiman [1]. Since then it has been developed into a powerful tool in many applications [2]. Solid materials can be ablated by pulsed laser and deposited onto substrate to form stoichiometric nano-structured thin films ornanostructures, which is the so-called pulsed laser deposition (PLD) [3].

PLD is a thin film deposition technique where a high-power pulsed laser beam is focused inside a vacuum chamber to strike a target of the material that is to be deposited. This material is vaporized from the target in a plasma plume which deposits it as a thin film on a substrate. This process can occur in ultra high vacuum or in the presence of a background gas. [1]

As shown in Fig. 2.1, the basic-setup of PLD system is simple relative to many other deposition techniques. A pulsed laser beam which is focused by a focal lens hits the surface of a solid target of known composition (which leads to the instantaneous vaporization of the target

materials), and the evaporated materials presented as a glowing plasma plume condenses onto a substrate.

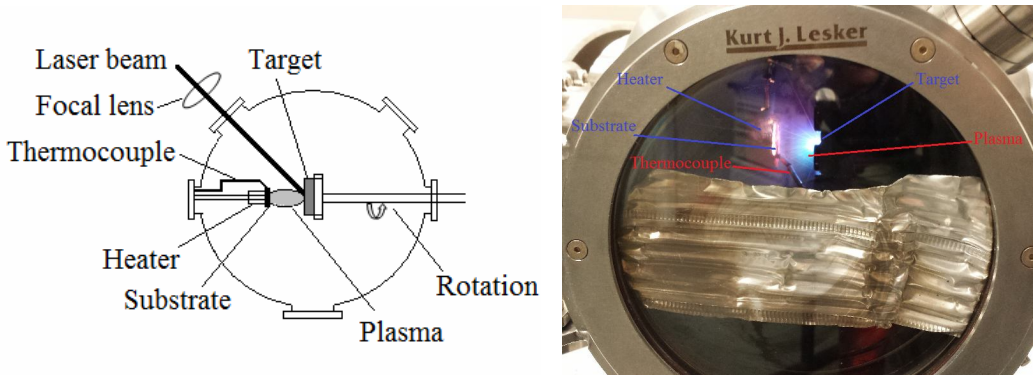

Fig. 2.1 Schematic of PLD system in our lab.

Fig. 2.2 shows the PLD system we installed in our laboratory for the growth of nanostructures. It consists of the following main parts as most of PLD system [4, 5]:

1) A spherical stainless steel chamber with a target holder, a stable substrate heater (up to 1200℃) together with a thermocouple and a substrate holder inside the chamber. The substrate is placed parallel to the target surface at a variable distance (2 cm- 5 cm).

2) Target rotation during ablation is necessary. Because after laser ablation, the grooves are formed on the surface of target, which results in unstable plasma plume during a long duration deposition. The target surface area can be used more effectively for a longer duration without groove formation.

3) Vacuum pump (mechanical pump and turbo pump) to evacuate the chamber; gauges, feed-throughs and flux controller for gas flow and pressure control.

4) Laser system, normally Excimer laser and Nd: YAG laser are used. In our PLD system, CO_2 laser with a wavelength ~10.6 μm and variable frequencies (1, 5, 10, 12 and 15 Hz) and high

voltage (HV1-HV5, 1010V-1130V) is used.

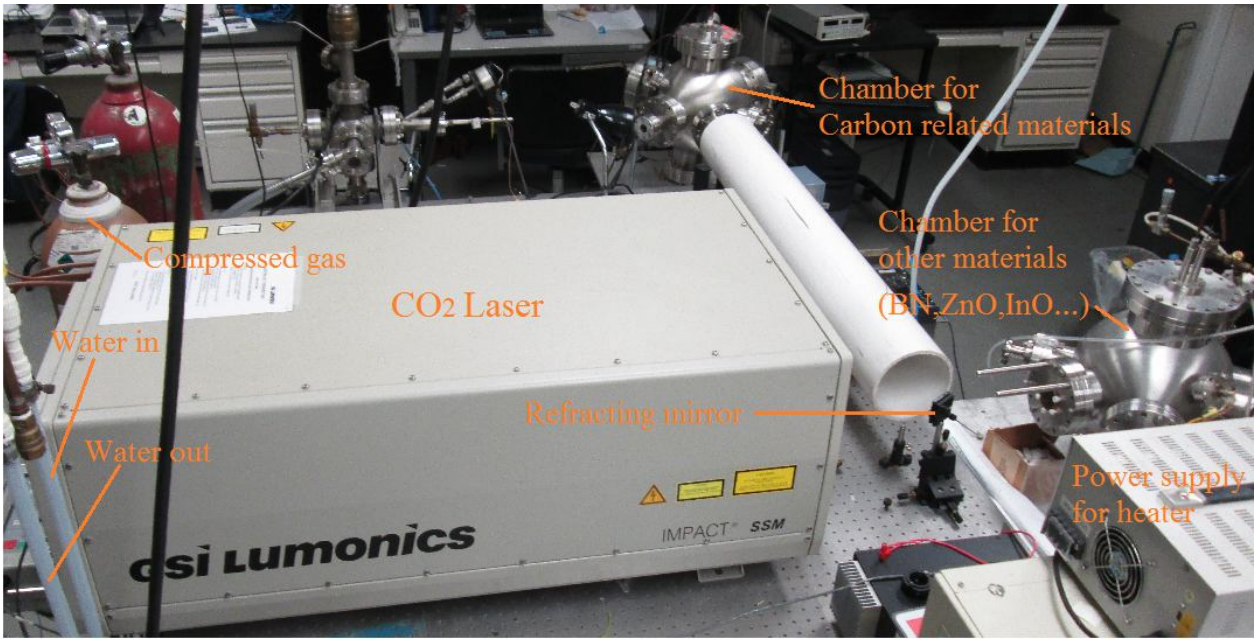

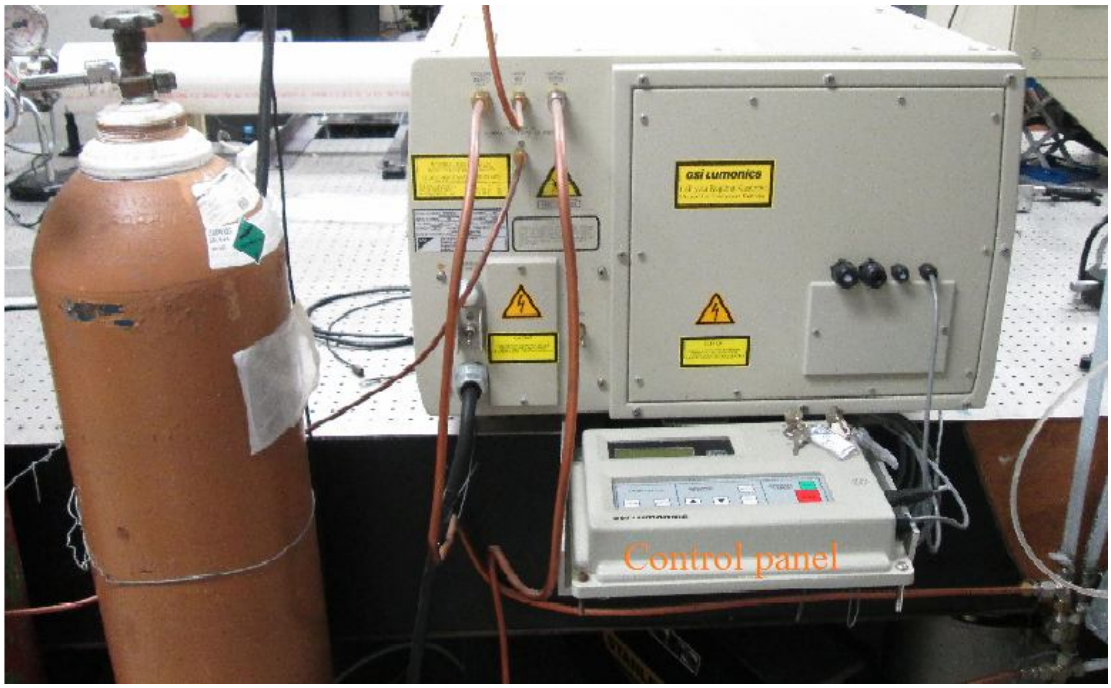

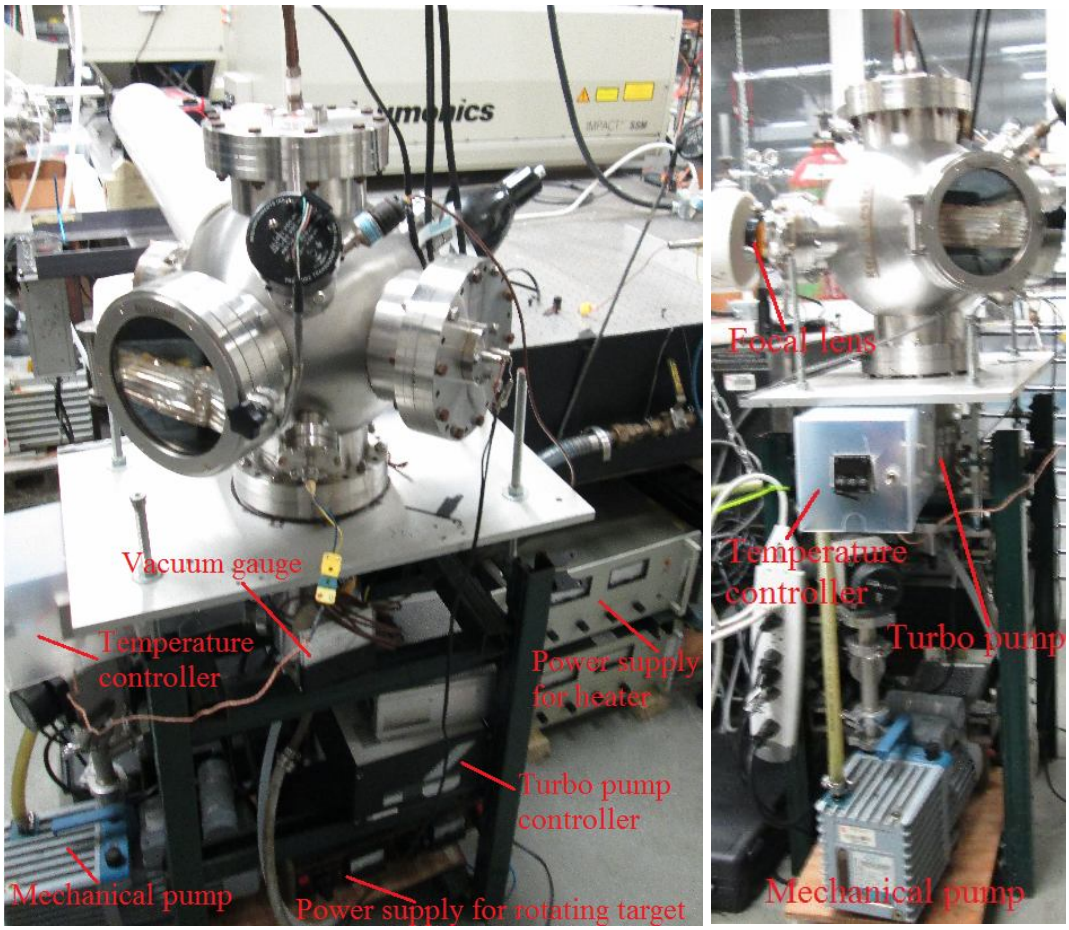

Fig. 2.2 Photograph of the PLD system installed in our lab.

In contrast to the simple setup of PLD system, the physical phenomena of laser-target interaction and film growth are very complex. The detailed mechanisms consist of the ablation process of the target material by the laser irradiation, the development of a plasma plume with high energetic ions, electrons as well as neutrals and the crystalline growth of the film itself on the heated substrate. The process of PLD can generally be divided into four stages [1, 5, 6]:

1) Laser ablation of the target material and creation of a plasma;

2) Dynamic of the plasma;

3) Deposition of the ablation material on the substrate;

4) Nucleation and growth of the film on the substrate surface.

Due to the short laser pulsed duration (~10 ns) and the small temporal spread (<10 m *s*) of the ablated materials, PLD has been used successfully to fabricate crystalline thin films with epitaxy quality. Ceramic oxide, nitride films, metallic multi-layers, hetero-structures and various super-lattices grown by PLD have been demonstrated [7-10]. PLD is extensively recognized as a thin film growth technique. However, the fabrication of nanostructures with PLD has been given less attention. Actually, one of the major advantages of PLD over the other techniques is that laser can ablate target materials over a wide range of pressure, which allows a precise control on morphology, size and composition of the fabricated nanostructures.

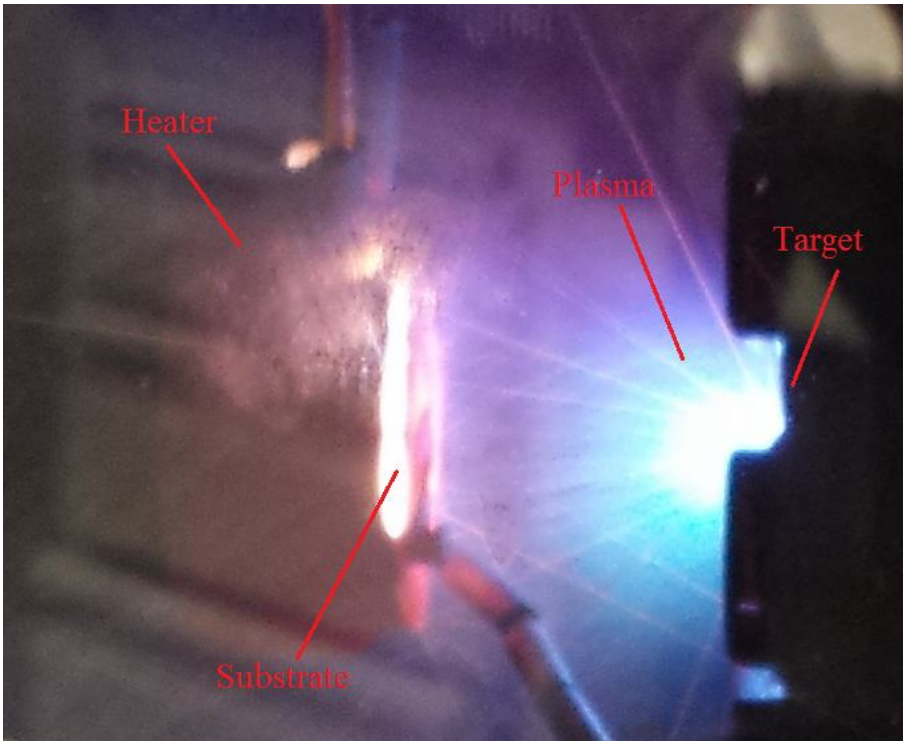

Fig. 2.3 The typical plasma plume from our PLD system.

Fig. 2.3 shows the typical plasma plume produced during the PLD process. A GSI LUMONICS IMPACT SSM CO_2 laser (10.6 μm, 5 Hz repetition rate) was used to irradiate the

commercial silicon carbide (SiC) target (purity up to 99.99%) at background pressure of 0.02 mTorr in the chamber. The diameter of the focused spot of the laser beam on the SiC target was ~2 mm, and the target was rotated at circa 200 rpm.

2.2 DC/RF sputtering techniques

Sputtering is a process whereby atoms are ejected from a solid target material due to bombardment of the target by energetic particles [11-13]. It only happens when the kinetic energy of the incoming particles is much higher than conventional thermal energies ($\gg$ 1 eV). This process can lead, during prolonged ion or plasma bombardment of a material, to significant erosion of materials, and can thus be harmful. On the other hand, it is commonly utilized for thin-film deposition, etching and analytical techniques [11].

During the early investigations of some nanomaterials, sputtering including DC sputtering, RF magnetron sputtering, and reactive sputtering, is one of the most popular growth techniques [12]. Sputtering process [15] is driven by momentum exchange between the energetic ions and atoms in the material, due to collisions as shown in Fig. 2.4. The number of atoms ejected from the target surface per incident ion is called the sputter yield, which is an important parameter of the efficiency of the sputtering process [5, 12, 13]. The sputter yield depends on the energy of the incident ions, mass of the ions and target atoms, and binding energy of atoms in the solid target. Sputtered atoms ejected from the target have a wide energy distribution, typically up to tens of eV (100,000 K). The sputtered ions (typically only a small fraction — order 1% — of the ejected particles are ionized) can ballistically fly from the target in straight lines and impact energetically on the substrates or vacuum chamber (causing resputtering). Alternatively, at higher gas pressures, the ions collide with the gas atoms that act as a moderator and move diffusively, reaching the substrates or vacuum chamber wall and condensing after undergoing a random walk. The entire

range from high-energy ballistic impact to low-energy thermalized motion is accessible by changing the background gas pressure. The sputtering gas is often an inert gas such as argon. For efficient momentum transfer, the atomic weight of the sputtering gas should be close to the atomic weight of the target, so for sputtering light elements neon is preferable, while for heavy elements krypton or xenon are used. Reactive gases can also be used to sputter compounds [16]. In order to control the plasma properties (ion/electron density) to achieve the optimum sputtering conditions, a variety of techniques are used including magnetic fields and a bias voltage to the target [5].

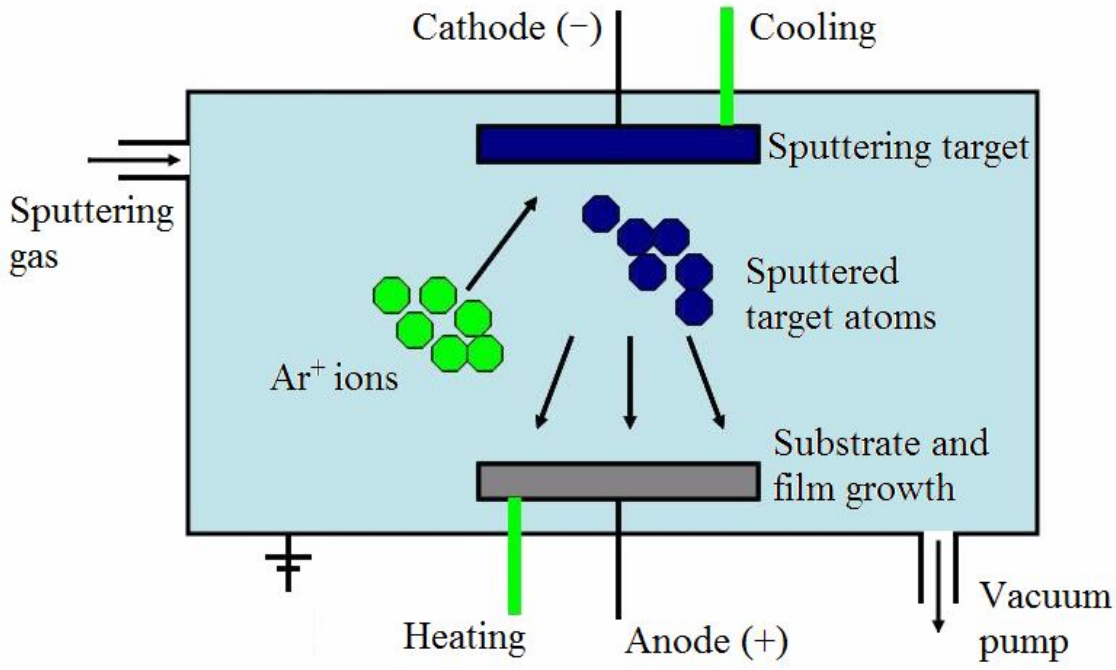

Fig. 2.4 Schematic of the sputtering process for nano-materials deposition.

Several additional benefits are derived from the sputter process [13]. Sputtering is done in a soft vacuum of 5 to 70 millitorr, pressures obtainable by small, reliable and inexpensive mechanical pumps. This eliminates the costly and elaborate high vacuum pump system required in evaporative coating. Sputter coating is specific with regard to the amount of coating material

needed to achieve a desired coating thickness, and evaporative coating is much more wasteful of material; consequently the annual cost of the precious metal or semiconductor used is significantly reduced [15].

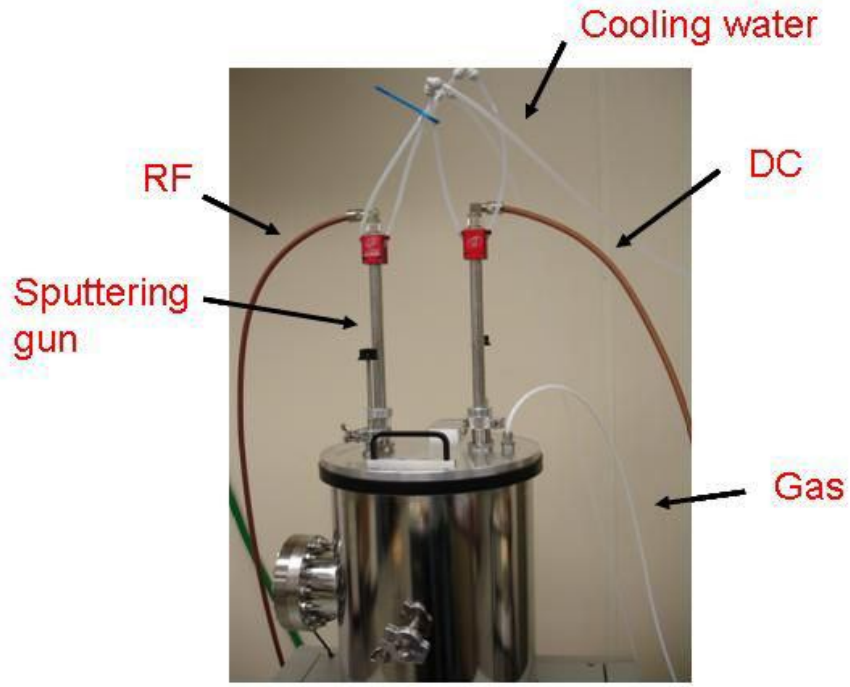

Fig. 2.5 Photograph of the top part of our sputtering system.

Shown in Fig. 2.5 is our sputtering system (2006 HUMMER 8.3, Anatech Ltd, CA) we installed in laboratory, which has two magnetron sputtering guns supplied with RF and DC power supplies respectively which allows co-sputtering of metallic and insulating materials. Fig. 2.6 shows the bottom part of our sputtering system, the heating controller is home-made, which affords the temperature of substrates varying in 100- 800 ℃.

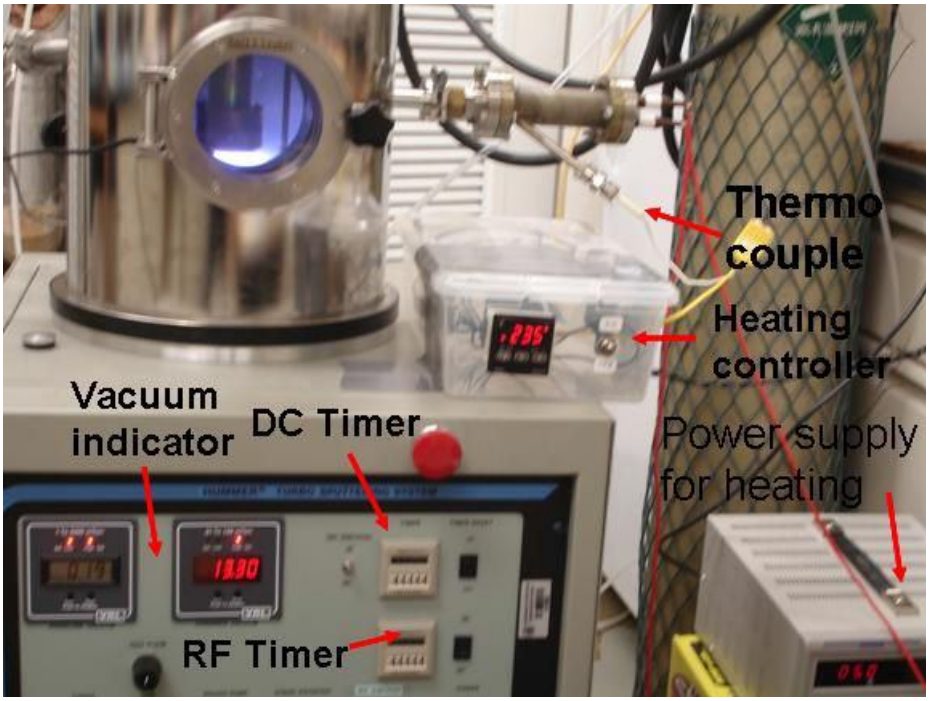

Fig. 2.6 Photograph of the bottom part of our sputtering system.

In our RF/DC magnetron sputtering system, as shown in Fig. 2.7, the sputtering source has the unique feature of attaching the target using magnetic force [17]. This is accomplished by attaching a magnetically permeable "keeper" to the bottom of the target. This keeper coupling with the magnetic field of the sputtering source provides sufficient force to clamp and center the target, eliminating the need for complex mechanical clamps. Specially, for non-machinable materials like ceramic and oxide materials, a copper backing plate containing a magnetic keeper should be used. The target must be bonded to this backing plate and this bond must be able to withstand a temperature of 220℃. Fig. 2.7c shows one example of a ZnO target bonded to a copper backing plate with a magnetic keeper attached. Fig. 2.7d shows the magnetron sputter gun with the target-mounting surface, the vacuum feedthrough, the power connector and the water lines [16] (connected to a cooling system to cool down the sputter gun and the target, as shown in Fig. 2.8).

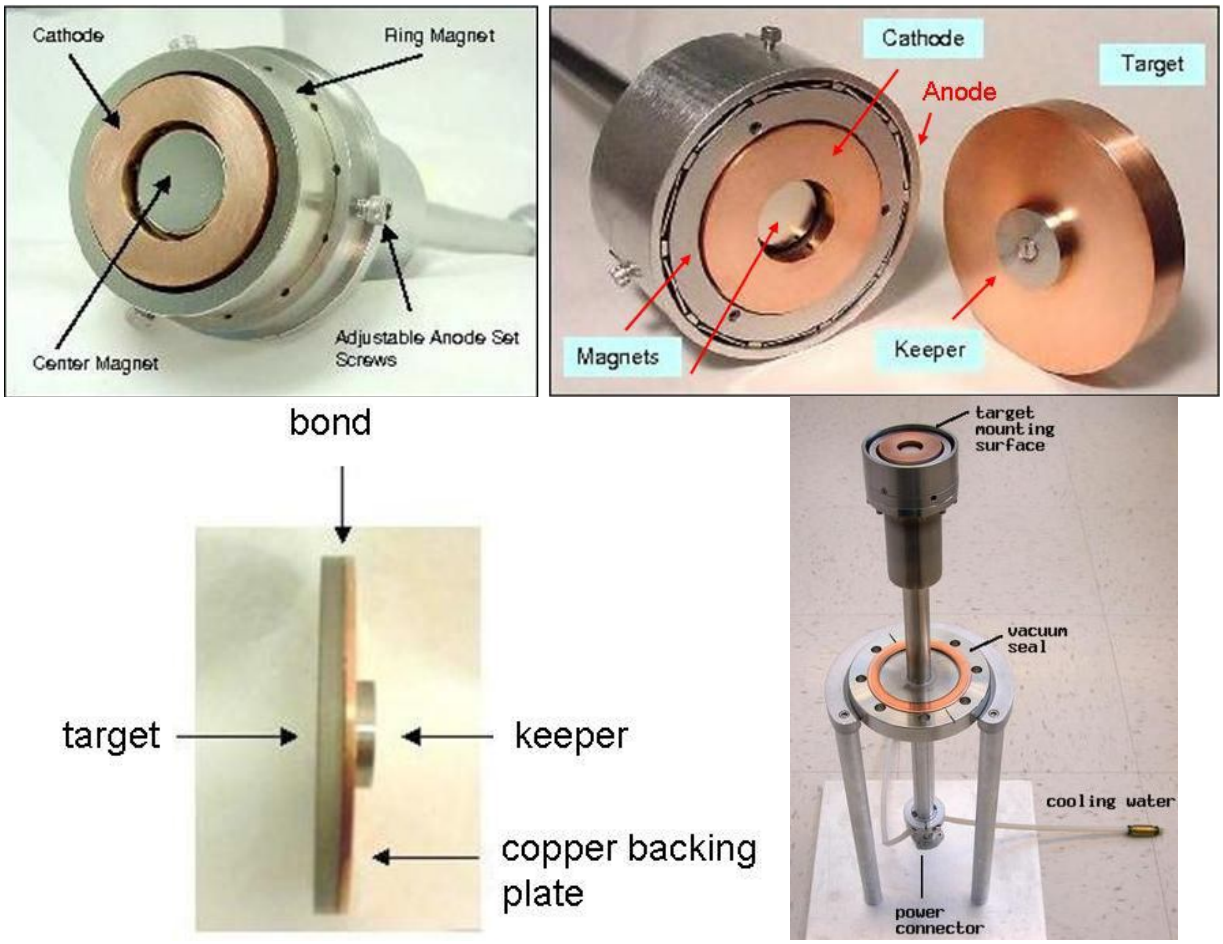

Fig. 2.7 Magnetron sputtering gun and configuration of the sputtering source.

Fig. 2.8 Cooling system for our sputtering system.

2.3 HFCVD/PVD techniques

Chemical vapor deposition (CVD) is a chemical process used to produce high-purity, high-performance solid materials. The process is often used in the semiconductor industry to produce thin films. In typical CVD, the substrate is exposed to one or more volatile precursors, which react and/or decompose on the substrate surface to produce the desired deposit. Frequently, volatile by-products are also produced, which are removed by gas flow through the reaction chamber [18].

Many types of CVD are commonly used to deposit thin films. Following are several CVD techniques:

1) Plasma-Enhanced CVD (PECVD): Utilizes plasma to enhance chemical reaction rates of the precursors. PECVD processing allows deposition at lower temperatures, which is often critical

in the manufacture of semiconductors. The lower temperatures also allow for the deposition of organic coatings, such as plasma polymers, that have been used for nanoparticle surface functionalization [19].

2) Atomic-layer CVD (ALCVD): Deposits successive layers of different substances to produce layered, crystalline films.

3) Combustion Chemical Vapor Deposition (CCVD): CCVD or flame pyrolysis is an open-atmosphere, flame-based technique for depositing high-quality thin films and nanomaterials.

4) Hot-wire CVD (HWCVD): Also known as hot filament CVD (HFCVD), this process uses a hot filament to chemically decompose the source gases [20].

5) Hybrid Physical-Chemical Vapor Deposition (HPCVD): This process involves both chemical decomposition of precursor gas and vaporization of a solid source.

6) Metalorganic chemical vapor deposition (MOCVD): This CVD process is based on metalorganic precursors.

Fig. 2.9 shows the HFCVD/PVD system we installed in our laboratory for the growth of nanostructures in our work. Different tungsten oxide nanostructures can be grown using our HFCVD system [21, 22]. The HFPVD technique is a simple technique in which the easily available graphite stick (0.5-1.0mm diameter, 15mm length) is used as a precursor to provide a carbon source and filament, to replace the tungsten filament in our HFCVD system[21, 22].

Variable nanomaterials can be synthesized on different substrates using the HFPVD technique at different temperatures and incident angles. A thermocouple is introduced to estimate the substrate temperature. No catalyst or other carbon-containing compound precursor will be used. Prior to the experiments, the substrates is ultrasonically washed in a methanol solution for 5 min, and dried with nitrogen. After placing the substrate, the chamber is pumped down to 2.67×10^{-3} Pa,

then fed with Ar gas to ambient pressure, and then pumped down to 2.67×10^{-3} Pa. This process will be repeated thrice to keep oxygen out and obtain a good vacuum. A dc power supply HY3020E with an electric current of 18A is used to heat the filament to a temperature of up to 2000 ℃ to promote gas phase activation. The substrate is placed on a holder under the hot filament. No extra heater is used to heat the substrate. The temperature of the substrate is controlled by simply changing the distance between the substrate and the hot filament. The position of the substrate on the holder can be changed to get different incident angles [23].

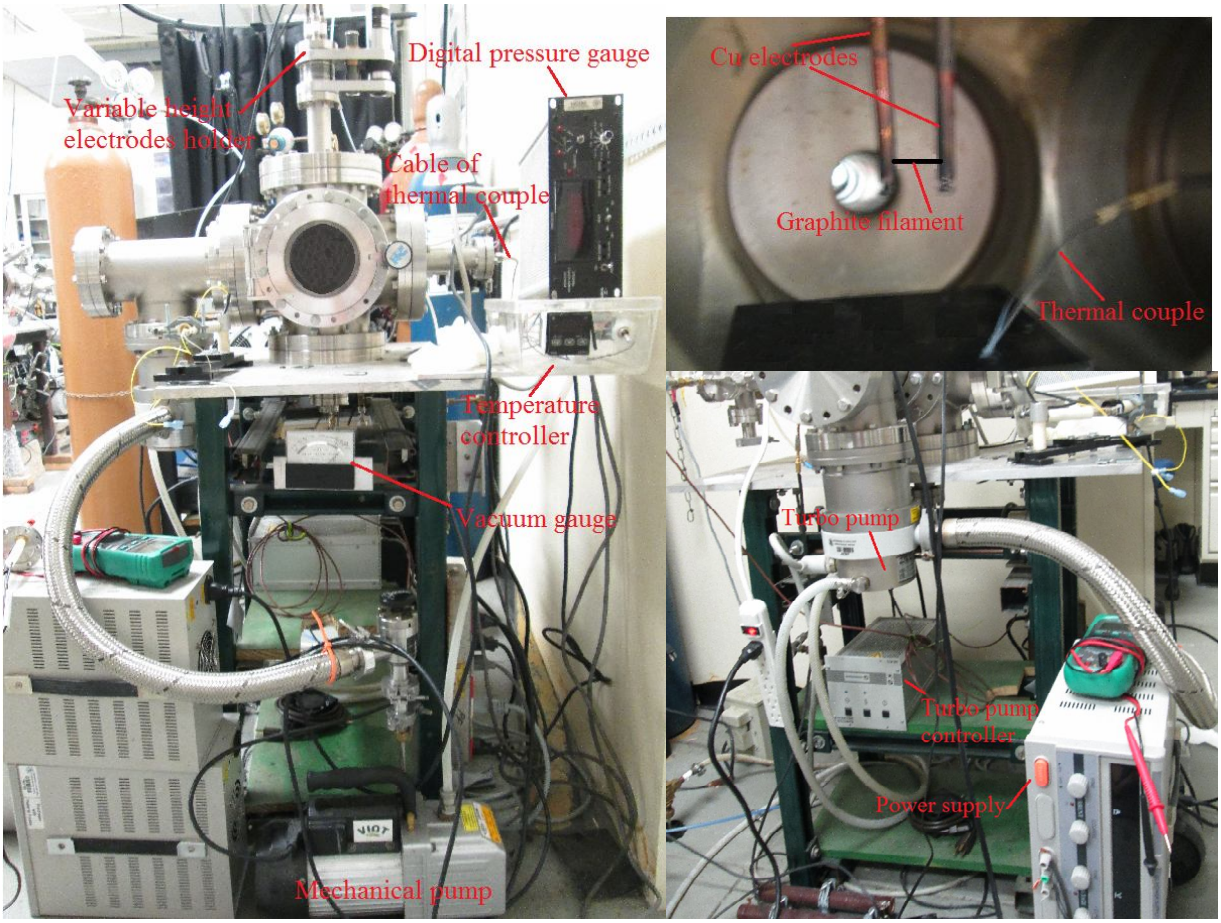

Fig. 2.9 Photograph of the HFCVD/PVD system we installed in lab.

In this thesis work, different carbon nanomaterials were synthesized by using this simple HFPVD technique, see chapter 3 and 4 in details.

2.4 SEM and EDS

Scanning electron microscope (SEM) is a type of electron microscope that produces images of a sample by scanning it with a focused beam of high-energy electrons to generate a variety of signals at the surface of solid specimens. The electrons interact with atoms in the sample, producing various signals that can be detected and that contain information about the sample's surface topography and composition. The electron beam is generally scanned in a raster scan pattern, and the beam's position is combined with the detected signal to produce an image. SEM can achieve resolution better than 1 nanometer [24]. SEM is also capable of performing analyses of selected point locations on the sample. This approach is especially useful in qualitatively or semi-quantitatively determining chemical compositions using EDS [25].

In a typical SEM electrons are thermionically emitted from a tungsten or lanthanum hexaboride (LaB6) cathode and are accelerated towards and anode; alternatively, electrons can be emitted via field emission (FE). The electron beam, which typically has an energy ranging from a few hundred eV to 100 keV, is focused by one or two condenser lenses into a beam with a very fine local spot. The beam then passes through pairs of scanning coils or pairs of deflector plates. The objective lens deflects the beam horizontally and vertically so that it scans in a raster fashion over a rectangular area of the sample surface. When the primary electron beam interacts with the sample, the electrons lose energy by repeated scattering and absorption within a teardrop-shaped volume of the specimen known as the interaction volume, which extends from less than 100 nm to around 5 μm into the surface. The size of the interaction volume depends on the electrons' landing energy, the atomic number of the specimen and the specimen's density. The energy exchanges

between the electron beam and the sample results in the emission of electrons and electromagnetic radiation, which can be detected to produce an image. The most common imaging mode monitors low energy (<50 eV) secondary electrons. Due to their low energy, these electrons originate within a few nanometers from the surface. The electrons are detected by a scintillator-photomultiplier device and the resulting signal is rendered into a two-dimensional intensity distribution that can be viewed as an image. The brightness of the signal depends on the number of secondary electrons reaching the detector. Besides secondary electrons, back-scattered electrons are also produced when the electron beam interacts with the sample. The back-scattered electrons consist of high energy electrons originating in the electron beam that are reflected or back-scattered out of the specimen interaction volume. Back-scattered electrons may be used to detect contrast between areas with different chemical compositions, since the brightness of the back-scattered electron (BSE) image tend to increase with the atomic number [26, 27].

SEM has many advantages over traditional microscopes. It has a large depth of field, which allows more than a specimen to be in focus at one time. SEM also has much higher resolution, so closely spaced specimens can be magnified at much higher levels. Because the SEM uses electromagnets rather than lenses, the researcher has much more control in the degree of magnification. All of these advantages, as well as the actual strikingly clear images, make SEM one of the most useful instruments in research today [28]. Shown in Fig. 2.10 is a JEOL JSM-7500F field emission Scanning electron microscope (FESEM) in our university, one of SEM instrument we used in this work.

Fig. 2.10 JEOL JSM-7500F FESEM in our university.

2.5 TEM

Transmission electron microscopy (TEM) is a microscopy technique in which a beam of electrons is transmitted through a thin specimen, interacting with the specimen as it passes through it. Electrons are usually generated in an electron microscope by thermionic emission from a filament, in this case LaB6, or by field emission. The stream of electrons is focused to a small, thin, coherent beam by the use of two condenser lenses. The first lens largely determines the spot size, which is the general size range of the final spot that strikes the sample. The second lens actually

changes the size of the spot on the sample changing it from a wide dispersed spot to a pinpoint beam. The beam is restricted by the condenser aperture knocking out high angle electrons which then strikes the specimen where parts of it are transmitted. Depending on the density of the material present, some of the electrons are scattered (elastically or inelastically) and disappear from the beam. The transmitted portion of the beam (unscattered electrons) is focused by the objective lens into an image. The image is passed down the column through the intermediate and projector lenses, being enlarged all the way. The image strikes down the phosphor image screen and light is generated, allowing the user to see the image [26, 29]. Shown in Fig. 2.11 is a typical TEM instrument.

TEMs are capable of imaging at a significantly higher resolution than light microscopes, owing to the small de Broglie wavelength (or matter wavelength) of electrons. This enables the instrument's user to examine fine detail—even as small as a single column of atoms, which is thousands of times smaller than the smallest resolvable object in a light microscope.

At smaller magnifications TEM image contrast is due to absorption of electrons in the material, due to the thickness and composition of the material. At higher magnifications complex wave interactions modulate the intensity of the image, requiring expert analysis of observed images. Alternate modes of use allow for the TEM to observe modulations in chemical identity, crystal orientation, electronic structure and sample induced electron phase shift as well as the regular absorption based imaging. [30]

Fig. 2.11 Photograph of a typical TEM instrument.

2.6 Raman spectroscopy

Raman spectroscopy is a spectroscopic technique used to investigate vibrational, rotational, and other low frequency modes in a system [31]. It relies on inelastic scattering, or Raman scattering of monochromatic light, usually from a laser in the visible, near infrared, or near ultraviolet range [32, 33]. The laser light interacts with phonons in the system, resulting in the energy of the laser photons being shifted up or down. The shift in energy gives information about the phonon modes in the system. The energy difference between the initial and final vibrational levels, ν, or Raman shift in wave numbers (cm^{-1}) is given by: incident scattered

$$\nu = 1/\lambda_{incident} - 1/\lambda_{scattered}$$

in which $\lambda_{incident}$ and $\lambda_{scattered}$ are the wavelengths (in cm) of the incident and Raman scattered photons, respectively. The Raman effects occur when light impinges upon a molecule or solid and interacts with the electron cloud of the bonds of the material. The incident photon excites one of the electrons into a virtual state. For the spontaneous Raman effects, the molecule or solid will be

excited from the ground state to a virtual energy state, and relax into a vibrational excited state, which generates Stokes Raman scattering. If the molecule or solid was already in an elevated vibrational energy state, the Raman scattering is then called anti-Stokes Raman scattering. The atoms in a Raman active molecule or solid will vibrate or oscillate about their normal positions with certain frequency. This type of vibration is called a normal mode of vibration. Solids and polyatomic molecules have more than one normal modes of vibration, each with their characteristic frequency. In solids this vibrations are called phonons. A polarizability change or amount of deformation of the electron cloud, with respect to the vibrational coordinate is required for the molecule or solid to exhibit the Raman effects. The amount of the polarizability change will determine the intensity, whereas the Raman shift is equal to the vibrational level that is involved. Typically, in Raman spectroscopy, the sample will be illuminated with a laser beam. Light from the illuminated spot of the sample is collected with a lens and sent through a monochromator. Wavelengths close to the laser line, due to elastic Rayleigh scattering, are filtered out while the rest of the collected light is dispersed into a detector. However, spontaneous Raman scattering is inefficient and usually very weak and as a result the main difficulty is separating the weak inelastically scattered light from the intense Rayleigh scattered laser light. Raman spectrometers typically use holographic diffraction gratings and multiple dispersion stages to achieve a high degree of laser rejection [32, 33]. Modern instrumentation almost universally employs notch or edge filters for laser rejection and spectrographs either AT (axial transmissive), CT (Czerny-Turner) monochromator, or FT (Fourier transform spectroscopy based), and CCD (Charge Coupled Device) detectors [31]. Fig. 2.12 shows a high-resolution Jobin-Yvon T-64000 Triple-mate Raman instrument. Our Raman measurements in this work are achieved using this system with an excitation wavelength of 514.5 nm (Ar^+ ion laser). A liquid nitrogen cooled

charge-coupled device system was used to collect and process the scattered data.

Fig. 2.12 A Jobin-Yvon T-64000 Triple-mate Raman instrument.

2.7 Field emission

Field emission**,** the emission of electrons from the surface of a conductor, caused by a strong electric field, also called Cold Emission [34] or Field Electron Emission [35]. Discharge of electrons from the surface of a material subjected to a strong electric field. In the absence of a strong electric field, an electron must acquire a certain minimum energy, called the work function, to escape through the surface of a given material, which acts as a barrier to electron passage. If the material is placed in an electric circuit that renders it strongly negative with respect to a nearby positive electrode, the work function is so lowered that some electrons will have sufficient energy to leak through the surface barrier. The resulting current of electrons through the surface of a material under the influence of a strong electric field is called field emission [34].

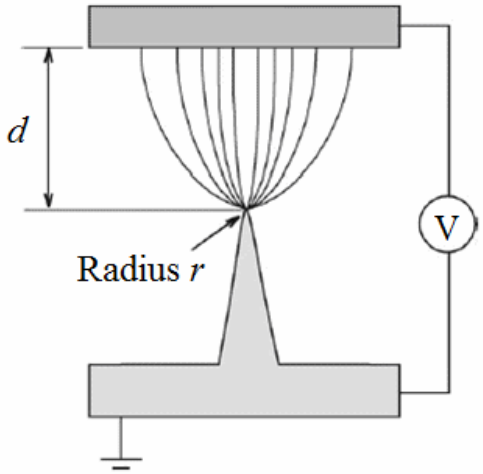

Fig.2.13 Illustration of field electron emission from a tip [36].

The electron field emission is a quantum-mechanical tunneling of electrons through the surface potential barrier into the vacuum upon the application of sufficiently high electric fields (10^7-10^8 V/cm) normal to the surface of metal, or semi-conducting. In practical terms, this means approximately 1000-10000 KV, for an anode-cathode separation of 1 mm. However, if the cathode surface has a high point as shown in Fig. 2.13, electrons may be extracted at a considerably lower applied gap field. This is because the lines of force converge at the sharp point and the physical geometry of the tip provides a field enhancement [36].

According to the Fowler–Nordheim (FN) theory, the field emission current density J (emission current I /emission area A) can be expressed as a function of the work function of the emission tip Φ and the local electric fields E_{local}. The FN equation [23, 35] is

$$J = A(E_{local})^2/\Phi \exp(-B\Phi^{3/2}/E_{local})$$

where A and B are constants and their values are 1.54×10^{-6} A eV V^{-2} and 6.83×10^3 $eV^{-2/3}$ V μm^{-1}, respectively. The local field E_{local} is related to the macroscopic applied electric field E by a dimensionless geometrical enhancement factor β [37, 38] as

$E_{local}=\beta E$

The value of β has been determined form the slope of the FN plot using the relation [39]

$\beta= B\Phi^{1.5}d/Slope$

where d is the distance of the anode from the emitting surface. The enhancement factor β was derived from the slope of the graph by assuming that the work function of the carbon nanostructures was the same as that of graphite (~5 eV).

According to above equations, the emission current is strongly dependent on the following three factors: (1) the work function of the emitter surface, (2) the radius of curvature of the emitter apex and (3) the emission area. It is clear that at a specific field, lower work function materials can produce higher electron emission current. However, not all low work function materials are ideal for construction of filed emission cathodes. For some materials, such as cesium or cesium coated cathodes, the stable emission and long lifetime will be an obstacle [36].

2.8 Sensing properties measurements

While the sensitivity of the electronic properties of carbon nanomaterials to the surrounding environment poses challenges in some applications, it offers a distinct advantage for sensors [40]. Their unique electrical, optical and mechanical properties make them very interesting for developing the new generation of miniaturised, low-power, ubiquitous sensors [41]. For more than a decade, carbon nanomaterials have been used to sense a variety of analytes including gases, solvents, biomolecules [40] and humidity [42, 43]. In the particular case of gas sensing, some carbon nanomaterials such as nanofibres, nanotubes and graphene are threatening the dominance position of other well established nanomaterials, yet the commercial exploitation of carbon nanomaterials is still a way off [41].

All sensors normally need to be tested and calibrated before applications. There are many

different types of equipment, which can be used for calibration of the sensors. We designed and fabricated a novel compact calibration system in our laboratory to calibrate gas, thermal and humidity sensors [44].

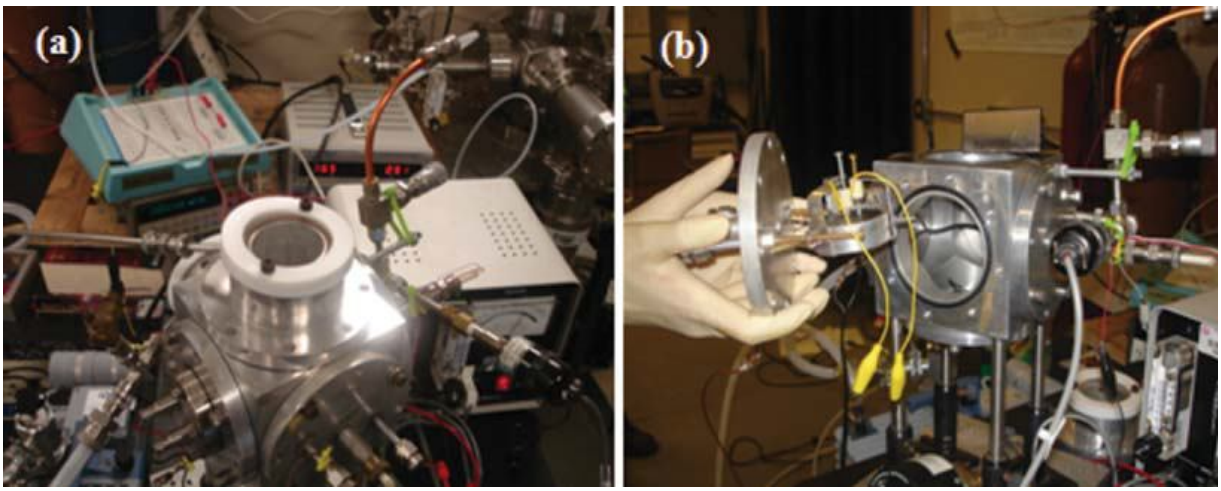

Fig. 2.14 Images of gas and thermal sensor calibration system [44].

Fig. 2.14 shows the images of the calibration system taken from external view (Fig. 2.14a) and internal view (Fig. 2.14b). Besides thermocouple, heater, a voltage-current-resistor (*V*-*I*-*R*) electrical circuit, gas flow controller, it also includes a plasma beam source for treatment of the surface of the sensor device. Several windows are also installed and used for analyzing plasma dynamics. Complementary plasma diagnostic tools, such as plasma spectroscopic diagnostics, are used to characterize the reactive species. The results obtained are used for optimizing calibration. It is a cheap, compact, and easily adjustable apparatus. All parameters, such as operating temperature, bias voltage, type of plasma source (for surface modification), types of gases, and gas flow rate (for calibrations), can be independently controlled.

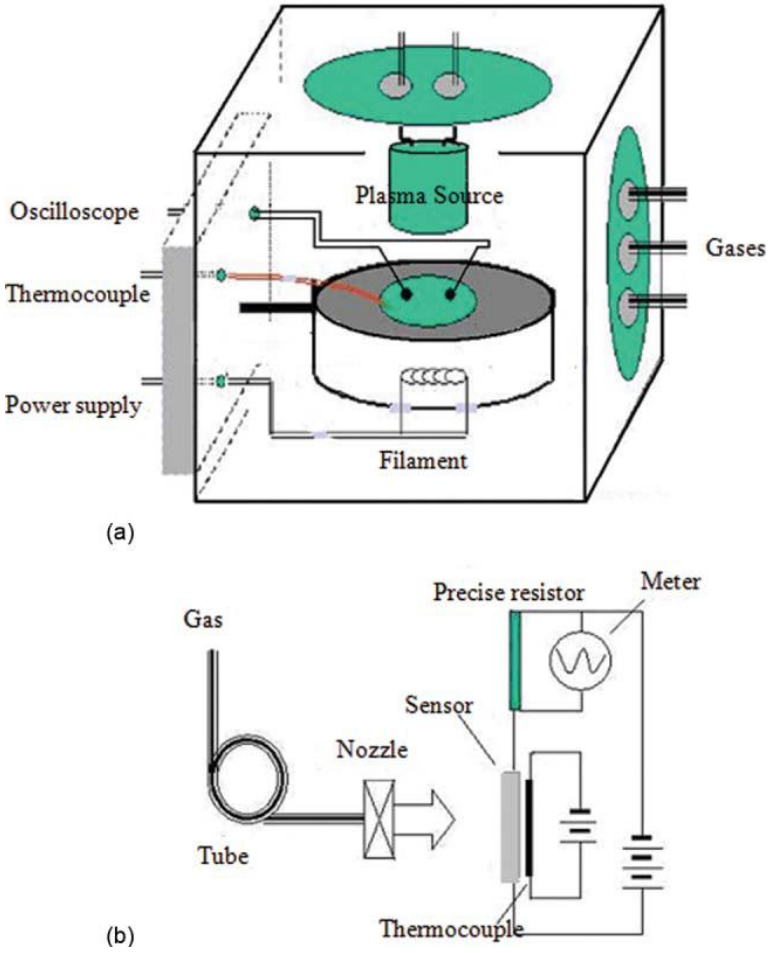

Fig. 2.15 A schematic diagram for static and dynamic characterizations of sensors.

Fig. 2.15 shows the schematic diagram of the system for the static and dynamic calibrations. Basically, measurement of sensor properties includes sensitivity/resistance: *Rs*, response time t_{resp} and recovery time t_{rec}. Two conductive rings installed at two ends of sensing material were connected to a precise resistor $R_{precise}$ and power supply (Stanford Research Systems PS350) $V_{power\ supply}$ with step voltage, respectively. Tungsten filament has been used as a heater that was installed for controlling operating temperature. The stability of temperature is ±5 ℃. The step voltage was provided by Keithley 6517 A electrometer, and the response signal was indicated by the same equipment as well. In order to reduce error, each data point during electronic measurements is the

average of 8 measurements taken 250 ms apart.

In the case of dynamic calibration of response and recovery times of the sensor, a pulse of supersonic gas beam has been installed that is created using a commercial pulse driver from Parker Hannifin Corporation and the response signal V_{precise} is captured and collected by WaveSurfer 452 oscilloscope from LeCroy as shown in Fig. 2.15b [44, 45].

2.9 References

[1] Pulsed Laser Deposition. From Wikipedia: http://en.wikipedia.org/wiki/Pulsed_Laser_Deposition

[2] S.M. Metev and V.P. Veiko, *Laser Assisted Microtechnology*, Springer, Berlin, Heidelberg (1994)

[3] D.B. Chrisey and G.K. Hubler, *Pulsed Laser Deposition of Thin Film*, John Wiley & Sons, Inc., New York (1994)

[4] V. Gupta and K. Sreenivas, *Pulsed laser deposition of Zinc Oxide*, Chapter 4, Edited by C. Jagadish and S. Pearton, Elsevier Limited (2006)

[5] B.Q. Yang, Ph.D Thesis, chapter 2 (2010)

[6] H.X. Zhang, Ph.D Thesis, chapter 2 (2011)

[7] T. Tawara, H. Gotoh, T. Akasaka, N. Kobayashi, and T. Saitoh, *Appl. Phys. Lett.* 83: 830 (2003)

[8] J.T. Chu, T.C. Lu, M. You, B.J. Su, C.C. Kao, H.C. Kuo, S.C. Wang, *App. Phys. Lett.* 89: 121112 (2006)

[9] P. Bhattacharya, R.R. Das, and R.S. Katiyar, *Thin Solid Films* 447-448: 564-567 (2004)

[10] A. Tsukazaki, *et al.*, *Nature Mateirals* 4: 42-46 (2005)

[11] R. Behrisch (ed.). *Sputtering by Particle bombardment*, Springer, Berlin (1981)

[12] U. Ozgur, Ya.I. Alivov, C. Liu, A. Teke, M.A. Reshchikov, S. Dogan, V. Avrutin, S.J. Cho, and H. Morkoc, *Journal of Applied Physics* 98: 041301 (2005)

[13] Operations & Service Manual, Hummer 8.3 RF & DC Power Supplies Deposition System, Anatech Ltd. Union City, CA (2006)

[14] Sputtering. From Wikipedia: http://en.wikipedia.org/wiki/Sputtering

[15] D.S. Camphell, *Handbook of thin film technology*, Ed. L.I. Maissel, and R. Glang, McGraw Hill, New York (1979)

[16] Sputter deposition. From Wikipedia: http://en.wikipedia.org/wiki/Sputter_deposition

[17] MAK Owner's operation and maintenance manual of the MAK sputtering sources, MEI-VAC INC. San Jose, CA (2006)

[18] Chemiacl vapor deposition. From Wikipedia: http://en.wikipedia.org/wiki/Chemical_vapor_deposition

[19] J. Tavares, E.J. Swanson, S. Coulombe, *Plasma Processes and Polymers* 5 (8): 759 (2008)

[20] R.E.I. Schropp, B. Stannowski, A.M. Brockhoff, P.A.T.T. van Veenendaal and J.K. Rath, *Mater. Phys.Mech.* 1: 73–82 (2000)

[21] P.X. Feng, X.P. Wang, H.X. Zhang, B.Q. Yang, Z.B. Wang, A. Gonzalez-Berrios, G. Morell and B. Weiner, *J. Phys. D: Appl. Phys.* 40: 5239 (2007)

[22] X.P. Wang, B.Q. Yang, H.X. Zhang and P.X. Feng, *Nanoscale Res. Lett.* 2: 405 (2007)

[23] J. Chu, X.Y. Peng, A. Aldalbahi, M. in het Panhuis, R. Velazquez and P.X. Feng, *J. Phys. D: Appl. Phys.* 45: 395102 (2012)

[24] Scanning electron microscope. From Wikipedia: http://en.wikipedia.org/wiki/Scanning_electron_microscope

[25]Susan Swapp, University of Wyoming: http://serc.carleton.edu/research_education/geochemsheets/techniques/SEM.html

[26] R.F. Egerton, *Physical Principles of Electron Microscopy: An introduction to TEM, SEM and AEM*, Springer Science & Business Media, Inc., New York, USA (2005) chapter 5

[27] J. Goldstein, D. Newbury, D. Joy, C. Lyman, P. Echlin, E. Lifshin, L. Sawyer and J. Michael, *Scanning Electron Microscopy and X-Ray Microanalysis*, Springer Science & Business

Media, Inc., New York, USA (2003), chaper2

[28] Purdue University, http://www.purdue.edu/rem/rs/sem.htm

[29] D.B. Willianms and C. Barry Carter, *Transmission Electron Microscopy*, Springer Science & Business Media, Inc., New York, USA (1996) volume 1

[30] Transmission electron microscopy. From Wikipedia: http://en.wikipedia.org/wiki/Transmission_electron_microscopy

[31] Raman spectroscopy. From Wikipedia: http://en.wikipedia.org/wiki/Raman_spectroscopy

[32] D.C. Harris and M.D. Bertolucci, *Symmetry and Spectroscopy: An Introduction to Vibrational and Electronic Spectroscopy*, Dover Publications, Inc., New York, USA (1989) chaper 3

[33] T.H. Gfroerer, in Encyclopedia of Analytical Chemistry, ed. R. A. Meyers, John Wiley & Sons, Ltd, Chichester, England (2000) 9209-9231

[34] Field emission. *Encyclopaedia Britannica. Encyclopaedia Britannica Online Academic Edition*. Encyclopædia Britannica Inc., 2014: http://www.britannica.com/EBchecked/topic/206253/field-emission

[35] Field electron emission. From Wikipedia: http://en.wikipedia.org/wiki/Field_electron_emission

[36] N.S. Xu, S.Ejaz Huq, *Materials Science and Engineering*, R 48, 47-189 (2005).

[37] R.C. Che, M. Takeguchi, M. Shimojo and K. Furuya, *J. Phys.: Conf. Ser.* 61: 200 (2007)

[38] Y. Ryu, Y. Tak and K. Yong, *Nanotechnology* 16: S370 (2005)

[39] R.B. Rakhi, K. Sethupathi, and S. Ramaprabhu, *Carbon* 46: 1656 (2008)

[40] D. Jariwala, V.K. Sangwan, L.J. Lauhon, T.J. Marks and M.C. Hersam, *Chem. Soc. Rev.* 42: 2824-2860 (2013)

[41] E. Llobet, Sensors and Actuators B 179: 32– 45 (2013)

[42] J. Chu, X.Y. Peng, P. Feng, Y. Sheng, J. Zhang, Sensors and Actuators B 178: 508– 513 (2013)

[43]J.P. Lukaszewicz, *Electronic Technology* 33: 195–206 (2000)

[44] P.X. Feng, H.X. Zhang, X.Y. Peng, M. Sajjad, and J. Chu, *Rev. Sci. Instrum.* 82: 043303 (2011)

[45] P.X. Feng and B.W. James, *Plasma Sources Sci. Technol.* 13: 68 (2004)

Chapter 3

Synthesis and characterization of carbon micro- and nanorods

In this chapter, tilted well-aligned carbon micro- and nano- hybrid rods were synthesized on Si at different substrate temperatures and incident angles of carbon source beam using the hot filament physical vapour deposition technique. The morphologic surfaces and bond structures of the oblique carbon rod-like structures were investigated by scanning electron microscopy, field emission scanning electron microscopy, transmission electron diffraction and Raman scattering spectroscopy. The field emission behaviour of the fabricated samples was also measured.

3.1 Introduction

One-dimensional carbon nanostructures (such as nanocones, nanotubes, nanoprisms and nanorods) have been widely studied as the next-generation cold cathodes candidates in field emission (FE) displays due to their unique electrical, chemical and mechanical properties [1–5]. A large number of carbon nanostructures have been obtained based on various techniques, including catalyst assisted solid-state growth process [6], reactive plasma beam sputtering [7], pulsed laser deposition (PLD) techniques [8, 9], electron beam induced deposition [10, 11], chemical vapor deposition (CVD) [12, 13], catalytic copyrolysis process [14] and benzene-thermal-reduction-catalysis route [15], etc. Recently, one-dimensional tilted nanorods are attracting noticeable research interest due to their inherent anisotropic nature with the tilted geometry. Ye et al prepared tilted Si nanorod arrays using a two-phase substrate rotation method with the oblique angle deposition technique, with which they produced nanorods with a controllable tilt angle [16]. We synthesized one-dimensional carbon tilted nanorods by using the catalyst-assisted oblique angle PLD technique [17]. However, these methods are limited by the

complicated fabrication process. So far, there is little information available for the synthesis of one dimensional tilted carbon microrods and nanorods.

In this work, we address a simple approach for synthesizing well aligned one-dimensional tilted micro- and nanorods hybrid carbon structure by hot filament physical vapor deposition (HFPVD) technique. The growth process has two remarkable features: firstly, this method can produce uniformly tilted carbon micro- and nanorods with a controllable angle; secondly, the experimental setup is simple and cost effective which satisfies the requirements of commercial applications.

3.2 Experimental setup

One-dimensional slanted carbon micro- and nanorods were synthesized on Si substrates using a simple HFPVD technique under different temperatures and incident angles. The easily-get graphite stick (0.7mm diameter, 15mm length) was used as a precursor to provide carbon source and filament, to replace the tungsten filament in our CVD system described elsewhere [18-20]. A thermocouple was introduced to estimate the substrate temperature. No catalyst or other carbon-containing compound precursor was used. Prior to the experiments, the substrates were ultrasonically washed in the methanol solution for 5mins, and dried with nitrogen. After placing the substrate, the chamber was pumped down to 2.67×10^{-3}Pa, then fed with Ar gas to ambient pressure, and then pumped down to 2.67×10^{-3}Pa. Repeated this process 3 times to keep oxygen out and obtain a good vacuum. A dc power supply HY3020E with an electric current of 18A was used to heat the filament to a temperature of up to 2000℃ to promote gas phase activation. The substrates were placed on a holder under the hot filament. No extra heater was used to heat the substrate. The temperature of the substrate was controlled by simply changing the distance between the substrate and the hot filament. The position of substrate on the holder can be changed

to get different incident angle. The deposition duration was 30 min for all the samples.

The morphologic surface, chemical composition and bond structure of obtained samples were investigated by scanning electron microscopy (SEM) at 20kV, field emission scanning electron microscopy (FESEM) at 15kV, transmission electron diffraction (TED) at 15kV, and Raman scattering spectroscopy, respectively.

The FE measurements were carried out in a vacuum chamber at a pressure of 4.0×10^{-5}Pa at room temperature. A molybdenum rod of 3 mm diameter (area: 0.071cm^2) serves as the anode. The macroscopic surface electric field (E_S) on the sample (i.e. cathode) is estimated by $E_S = V/d_{CA}$, where V is the voltage applied to the anode and d_{CA} ($100 \pm 2\mu m$) is the distance between the anode and the cathode. The current was detected using a KEITHLEY 6517A electrometer. The power supply was a Stanford Research Systems PS350. A detailed description of the FE measurement techniques can be found in our previous papers [18, 21].

3.3 Characterization of carbon micro- and nano- hybrid rods

Fig. 3.1 shows typical SEM images of the synthesized carbon samples (*a*, *b*, *c*) on Si substrates at temperature of (a) 800, (b) 900, (c) 1000℃, respectively. The insets are the cross section measured by JEOL JSM-7500F FESEM. The thickness of the samples is about 13.0 μm, 19.2 μm, 25.3 μm, respectively. Tail-like microrods with different sizes were observed for the samples under different substrate temperatures, but otherwise identical growth conditions. At 800 ℃, the oblique rods with the angle of ~58° to the normal of the substrate have a length of 22.0-24.5 μm and diameter 0.6-0.7 μm for their beginning part, and gradually increasing to 1.0-1.5 μm for the end part, which consist of plume- and bud-like structures. Raising substrate temperature to 900 and 1000℃, similar structures but with larger size were obtained. The rod length was 34.0-36.5

μm and 44.0-47.0 μm, the beginning part diameter was 0.65-0.75 μm and 0.7-1.0 μm, then the diameter gradually increased to 2.0-3.5 μm and 3.0-4.5 μm, respectively.

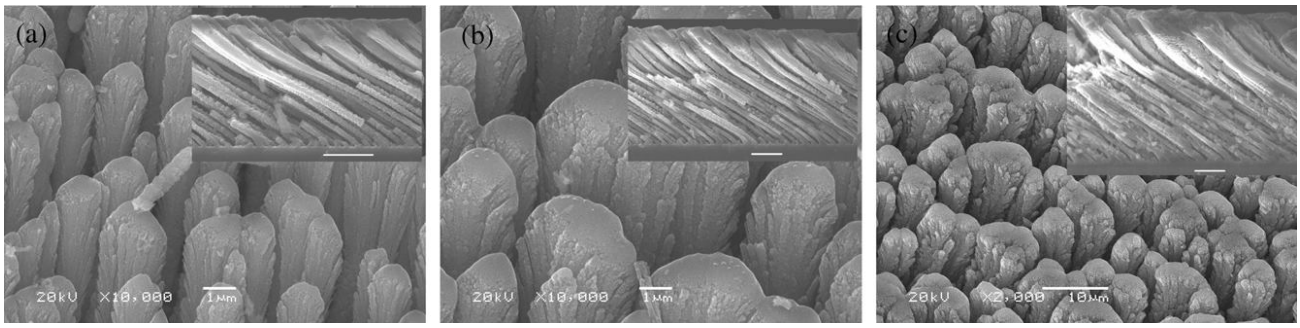

Fig. 3.1 SEM images of the carbon rod structure synthesized at different temperatures of (*a*) 800 ℃, (*b*) 900℃, (*c*) 1000℃ and the corresponding cross sections (insets). The scale bars are 1 μm for (*a*) and (*b*), 10 μm for (*c*) (5 μm in the insets).

Schematic growth mechanisms illustrated in Fig. 3.2 were proposed to explain the different growth modes for tail-like carbon microrods prepared by HFPVD technique. Fig. 3.2a is the sketch of the carbon stick filament connected to the copper electrodes, d_v and d_h is the vertical and horizontal distance between the filament and substrate, respectively, α is the carbon source incident angle to the normal of substrate. The detailed parameters and data of fabricated samples are shown in table 3.1. Fig. 3.2 b demonstrates the growth process of the tail-like micro- and nano-hybrid carbon rods. α' is the real angle of the rod to the normal.

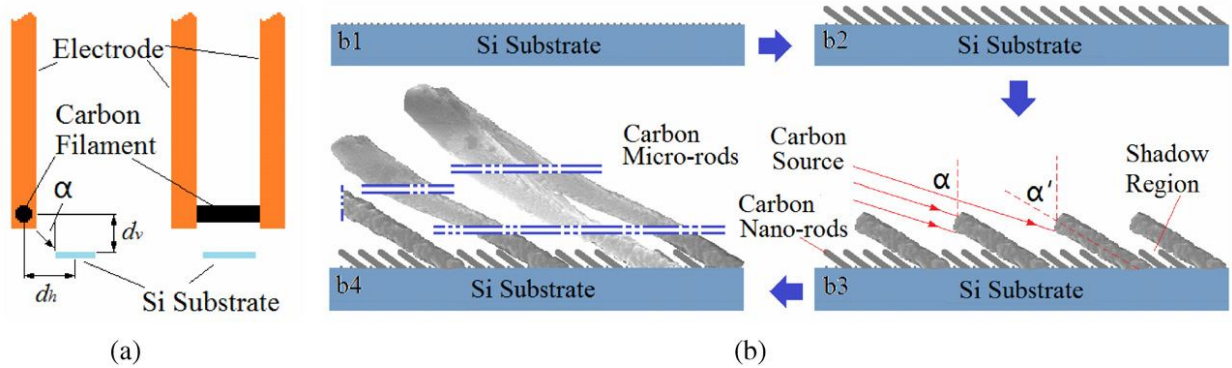

Fig. 3.2 Schematic illustration of (*a*) carbon filament and electrodes, (*b*) growth processes of tilted micro- and nano- hybrid carbon rods.

Table 3.1 Basic parameters

Sample	d_v (mm)	d_h (mm)	$d=\sqrt{(d_v^2+d_h^2)}$ (mm)	Substrate Temperature(℃)	α (°)	α'(°)	Thickness (μm)	Length (μm)	Beginning part dia. (μm)	End dia. (μm)
a	3.0	5.2	6.0	800	60	58.30	13.0	22.0-24.5	0.6-0.7	1.0-1.5
b	2.5	4.3	5.0	900	60	58.13	19.2	34.0-36.5	0.65-0.75	2.0-3.5
c	2.0	3.4	4.0	1000	60	57.68	25.3	44.0-47.0	0.7-1.0	3.0-4.5
d	3.5	7.5	8.3	600	65	60.22	5.5	10.9-11.1	0.35-0.5	0.8-1.0
e	2.8	7.8	8.3	600	70	61.35	4.6	8.9-9.6	0.38-0.6	0.6-1.1
f	2.1	8.0	8.3	600	75	62.46	3.9	8.2-8.5	0.3-0.5	0.6-0.9
g	1.4	8.2	8.3	600	80	63.54	3.3	6.9-7.4	0.35-0.45	0.5-0.9

Van der Drift model can be used to interpret the case of carbon rods as shown in Fig. 3.2b. Random orientation nuclei were developed on the substrate at the initial stage of deposition (Fig. 3.2b1) yields a geometric shadow region [22, 23] where the subsequent incident flux cannot reach. Consequently, the oblique incident plasma flux is preferentially deposited on to the top of surface features, thus nanorods are formed (Fig. 3.2b2). With continued deposition, parts of rod grow up continuously to micro size, but others (shadow area) do not change, as shown in Fig. 3.2b3. Shown in Fig. 3.2b4 is the final stage of deposition process that the tail-like microrods are developed. The sample surface has larger density than interior due to the larger size of the upper part than that of the beginning part.

Raman scattering spectra of the micro- and nanostructured carbon samples were also obtained at room temperature by using a high resolution Jobin-Yvon T-64000 Triple-mate instrument with an excitation wavelength of 514.5 nm (Ar+ ion laser). A liquid nitrogen cooled charge-coupled device system was used to collect and process the scattered data.

Fig. 3.3 shows the Raman spectra of the carbon samples *a*, *b*, *c*, respectively. Characteristic graphite peaks are identified in the Raman spectra between 1000 and 2000 cm^{-1}. The one at around 1345 cm^{-1} (1344, 1341, 1345 cm^{-1}, respectively) called D peak is associated with disorder-allowed zone edge modes of graphite that became Raman active due to the lack of long-range order in amorphous carbon-based materials. The G peak at around 1590 cm^{-1} (1587,

1594, 1602 cm^{-1}, respectively) corresponds to the G line associated with the optically allowed E_{2g}-zone centre of crystalline graphite [24].

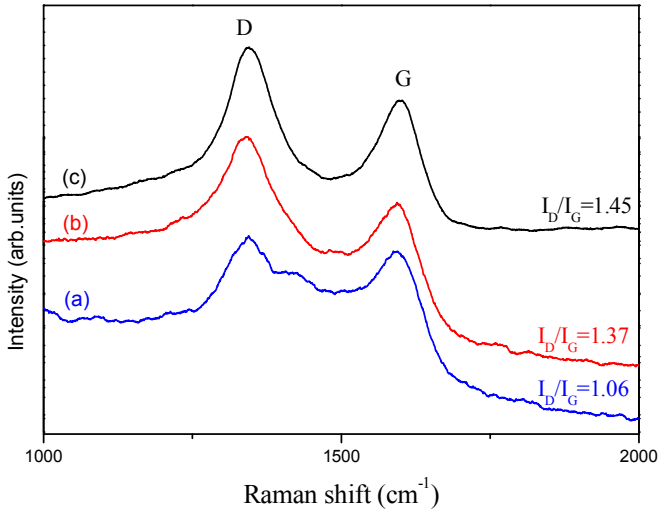

Fig. 3.3 Raman spectra of (a) sample a, (b) sample b, (c) sample c.

It is also noted that the Raman signal ratio I_D/I_G increases from 1.06 to 1.45 following the substrate temperature from 800 to 1000℃. Higher temperature may lead to more vaporific impurity from residue gas or contamination into the sample, which results in increased disorder. Similar phenomenon has been reported by other researchers [17, 21, 25].

The electrical properties of the samples *a*, *b*, *c* were investigated using a FE measurement system. Fig. 3.4 shows the field emission currents from the samples. The current density-electric field curve was obtained by recording each data point for 8 times with 250 ms apart in order to reduce errors. In this work, electric current lower than 1×10^{-10} A was considered as the background noise level. The turn-on field (E_t) is defined as the electric field necessary to emit 1 nA current. The E_t of this three samples was 9.1 V/μm (sample *a*), 5.8 V/μm (sample *b*) and 0.4 V/μm (sample *c*). It should be mentioned that because of the effect of the Si substrate and the SiO_2 on its surface, the actual E_t value should be lower than what we measured. We repeated the FE

measurement several times and the results showed a good consistency. The tail-like carbon rods deposited at 1000℃ has higher current density and lower turn-on field than others. These results clearly indicate that the FE characteristics of the samples are obviously improved under higher substrate temperature during the deposition process.

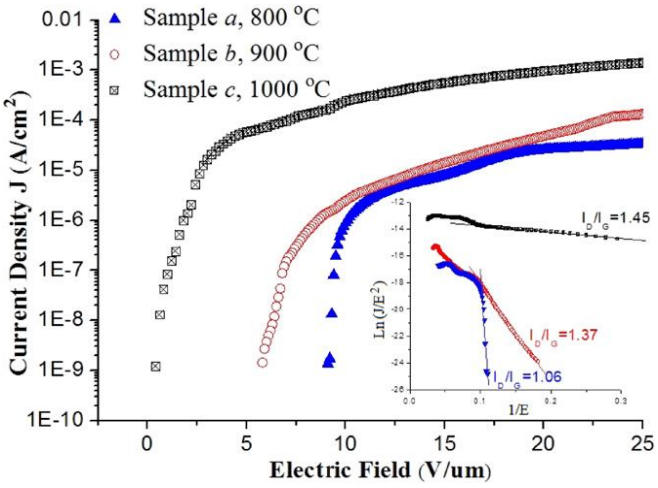

Fig. 3.4 *I–V* characteristics and FN plots (the inset) of samples a–c.

According to the Fowler–Nordheim (FN) theory, the field emission current density J (emission current I /emission area A) can be expressed as a function of the work function of the emission tip Φ, the applied electric fields E and the field enhancement factor β [10, 26, 27]. The FN equation is

$$J = A(\beta E)^2/\Phi \exp(-B\Phi^{3/2}/\beta E)$$

where A and B are constants and their values are 1.54×10^{-6} $A(eV)(V)^{-2}$ and 6.83×10^{3} $(eV)^{-2/3}V\mu m^{-1}$, respectively. The inset of Fig. 3.4 shows FN plots of the samples *a*, *b*, *c*. The fitted linear lines in the high voltage region indicate that electron emission follows the tunnelling mechanism, and from the slope of the fitted lines, the tail-like carbon micro- and nanorods hybrid

structure at 1000℃ exhibits a higher value of field enhancement factor (β) than the other two samples shown in Fig. 3.4 [28]. Higher temperature yields higher density of the carbon rods with plume-like structures that consists of many small tips. The distances between different tips are ~50-100 nm, which means each tip would emit electronics in FE measurement. Consequently, the sample deposited at higher substrate temperature shows better FE performance. It can also be found that the FE characteristics of the carbon samples were enhanced together with the increase in the Raman signal ratio I_D/I_G [25] from 1.06 to 1.45 shown in Fig. 3.4.

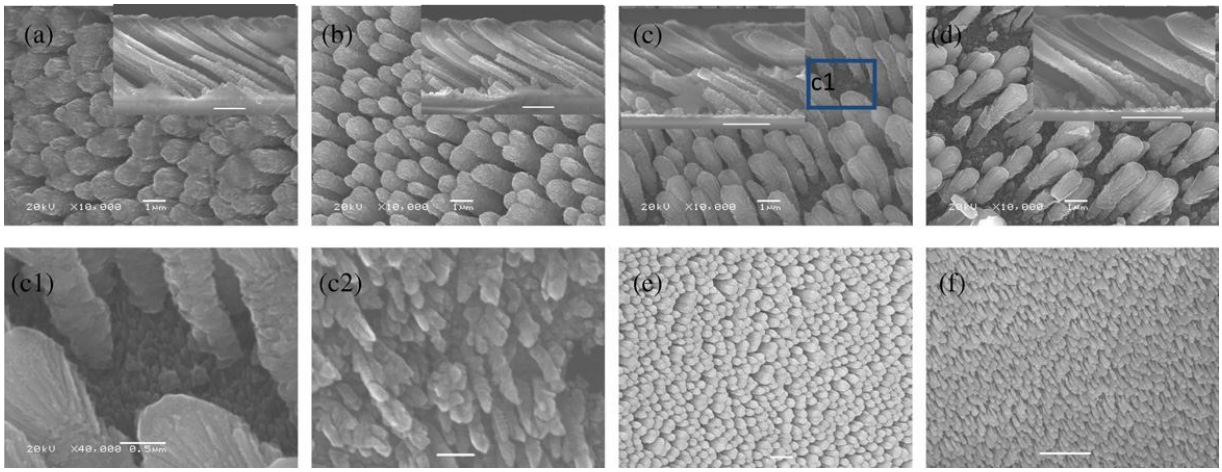

Fig. 3.5 (*a*)–(*d*) SEM images of carbon rod structure grown at 600℃ with different incident angles. (*c*1) Magnified SEM image of the selected area in (*c*). (*c*2) High-magnification FESEM image of the shadowed area in (*c*). (*e*), (*f*) Low-magnification FESEM images of samples e and f. The scale bars are (*a*)–(*d*) 1μm (2μm in the insets), (*c*1) 0.5μm, (*c*2) 100 nm, (*e*) 2μm, (*f*) 10μm.

In order to further study the effect of incident angle of carbon source on sample structure, additional four experiments have been conducted and the basic parameters for obtained four samples (*d*, *e*, *f*, *g*) are listed in Table 3.1. Fig. 3.5 shows SEM and FESEM images of carbon rods structures grown at 600℃ with different incident angle. The insets are FESEM images of their cross sections. Large-area uniformed tail-like microrods, which have an average length of 6.9-11.1 μm and diameters 0.3-0.6 μm and 0.6-1.2 μm for the beginning part and the end part, hybridized

with some 130-150 nm length, 25-35 nm diameter nanorods (Fig. 3.5c2) were found in the four samples.

The density of the microrods decreases with an increase of the incident angle. Fig. 3.5c1 shows the magnified SEM image of the selected area in sample *f* (Fig. 3.5c) where the micro- and nanorods hybrid structure is clearly visible. Fig. 3.5c2 shows a shadow area with slant carbon nanorods structure. It is inferred that well-aligned carbon nanorods might be synthesized by controlling deposition duration and introducing inert gas to slow down the deposition rate.

Fig. 3.5e and Fig. 3.5f show the lower magnification FESEM images of sample *e* and *f*, respectively, which confirms the large-area uniform rod-like structure.

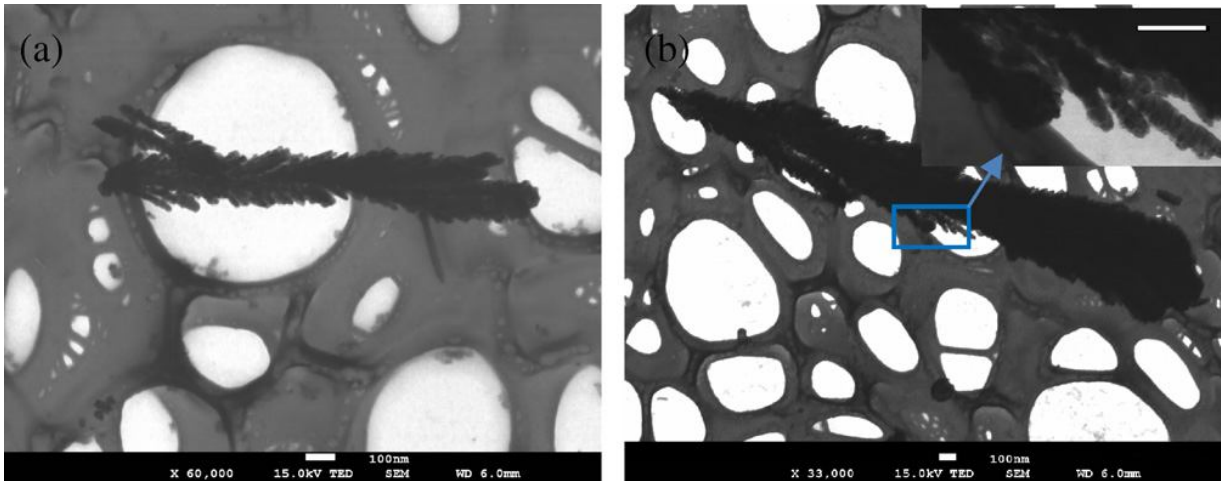

Fig. 3.6 TED BF images from sample f. The scale bars are 100 nm for (*a*), (*b*) and inset.

Fig. 3.6 shows the TED bright field (BF) images of single rods from the sample *f*. Shown in Fig. 3.6a is a plume-like structure with average diameter of 160 nm and length of 1.4 μm, which makes up the tail-like rod. Fig. 3.6b shows part of a tail-like rod from the sample *f* with a length of 3.4 μm and diameter of 0.4-0.6 μm, the inset is its enlarged image of the marked area. The experimental data provide direct evidence that each carbon rod has very coarse surface,

consequently, having extremely high surface area, which is definitely important for hydrogen storage application [29, 30].

3.4 Conclusion

In summary, we have demonstrated a simple route for synthesizing well aligned carbon micro- and nano- hybrid rod-like structures by using hot filament physical vapor deposition technique. The SEM images exhibit that micro-sized rods with different diameters are obtained for different substrate temperatures. The oblique angle and the density of the fabricated carbon rods are influenced by the incident angle of carbon source beam. The carbon nanorods with diameter of 25-35 nm are also obtained at the shadow areas. The turn-on field E_t of samples *a*, *b*, *c* is 9.1 V/μm, 5.8 V/μm and 0.4 V/μm. The field enhancement factor β increases following the increasing of substrate temperature from 800 to 1000℃ which is in accord with the Raman signal ratio I_D/I_G.

In this chapter, we studied the application of carbon nanorods on field emission. In the following chapters, we are going to investigate some other applications of various carbon nanomaterials.

3.5 References

[1] R.H. Baughman, A.A. Zakhidov, W.A. de Heer, *Science* 297: 787 (2002)

[2] A. Yamamoto, T. Tsutsumoto, *Diam. Relat. Mater.* 12: 1729 (2003)

[3] M.S. Wang, L.M. Peng, J.Y. Wang, C.H. Jin, Q. Chen, *J. Phys. Chem. B* 110: 9397 (2006)

[4] M.S. Wang, J.Y. Wang, L.M. Peng, *Appl. Phys. Lett.* 88: 243108 (2006)

[5] H.X. Zhang, P.X. Feng, *Appl. Surf. Sci.* 255: 5939 (2009)

[6] M.Y. Teng, K.S. Liu, H.F. Cheng, I.N. Lin, *Diam. Relat. Mater.* 12: 450 (2003)

[7] M. Ishihara, M. Suzuki, T. Watanabe, T. Nakamura, A. Tanaka, Y. Koga, *Diam. Relat. Mater.* 14: 989 (2005)

[8] H.X. Zhang, P.X. Feng, P. Jin, V.I. Makarov, L. Fonseca, G. Morell, B.R. Weiner, *Appl. Phys. Lett.* 95: 061906 (2009)

[9] H.X. Zhang, P.X. Feng, V.I. Makarov, L. Fonseca, G. Morell, B.R. Weiner, *J. Phys. D: Appl. Phys.* 42: 035409 (2009)

[10] R.C. Che, M. Takeguchi, M. Shimojo, K. Furuya, *J. Phys.: Conf. Ser.* 61: 200 (2007)

[11] I.C. Chen, L.H. Chen, X.R. Ye, C. Daraio, S. Jin, C.A. Orme, A. Quist, R. Lal, *Appl. Phys. Lett.* 88: 153102 (2006)

[12] J.B. Chen, C.W. Wang, J. Wang, Y. Li, R.S. Guo, B.H. Ma, F. Zhou, W.M. Liu, *Appl. Surf. Sci.* 256: 39 (2009)

[13] J.J. Schneider, N.I. Maksimova, J. Engstler, R. Joshi, R. Schierholz, R. Feile, *Inorg. Chim. Acta* 361: 1770 (2008)

[14] G.F. Zou, J. Lu, D.B. Wang, L.Q. Xu, Y.T. Qian, *Inorg. Chem.* 43: 5432 (2004)

[15] X.J. Wang, J. Lu, Y. Xie, G.A. Du, Q.X. Guo, S.Y. Zhang, *J. Phys. Chem. B* 106: 933 (2002)

[16] D.X. Ye, T. Karabacak, B.K. Lim, G.C. Wang, T.M. Lu, *Nanotechnology* 15: 817 (2004)

[17] H.X. Zhang, P.X. Feng, *J. Phys. D: Appl. Phys.* 42: 025406 (2009)

[18] P.X. Feng, X.P. Wang, H.X. Zhang, B.Q. Yang, Z.B. Wang, A. Gonzalez-Berrios, G. Morell, B. Weiner, *J. Phys. D: Appl. Phys.* 40: 5239 (2007)

[19] H.X. Zhang, B.Q. Yang, P.X. Feng, *J. Nanomater.*: 957935 (2008)

[20] X.P. Wang, B.Q. Yang, H.X. Zhang, P.X. Feng, *Nanoscale Res. Lett.* 2: 405 (2007)

[21] H.X. Zhang, P.X. Feng, *J. Phys. D: Appl. Phys.* 41: 155425 (2008)

[22] J. Chu, X.Y. Peng, M. Sajjad, B.Q. Yang, P.X. Feng, *Thin Solid Films* 520: 3493 (2012)

[23] C. Gaire, F. Tang, G.C. Wang, *Thin Solid Films* 517: 4509 (2009)

[24] H.Y. Li, Y.C. Shi, P.X. Feng, *Appl. Phys. Lett.* 89: 142901 (2006)

[25] M.C. Rossi, S. Salvatori, P. Ascarelli, E. Cappelli, S. Orlando, *Diam. Relat. Mater.* 11: 819 (2002)

[26] Y. Ryu, Y. Tak, K. Yong, *Nanotechnology* 16: S370 (2005)

[27] Field electron emission. From Wikipedia: http://en.wikipedia.org/wiki/Field_electron_emission

[28] C.Y. Su, Z.Y. Juang, Y.L. Chen, K.C. Leou, C.H. Tsai, *Diam. Relat. Mater.* 16: 1393 (2007)

[29] R. Strobel, J. Garche, P.T. Moseley, L. Jorissen, G. Wolf, *J. Power Sources* 159: 781 (2006)

[30] A.C. Dillon, M.J. Heben, *Appl. Phys. A* 72: 133 (2001)

Chapter 4

Fabrication and characterization of carbon films for humidity sensors

In this chapter, carbon nanosheets and nanohoneycombs were synthesized on Si (100) substrates using a hot filament physical vapor deposition technique under methane ambient and vacuum, respectively. The four-point Au electrodes are then sputtered on the surface of the nanostructured carbon (n-C) films to form prototypical humidity sensors.

The sensing properties of prototypical sensors at different temperature, humidity, direct current (DC), and alternative current (AC) voltage were characterized. Linear sensing response of sensors to relative humidity ranging from 11% to 95% is observed at room temperature. Experimental data indicate that the carbon nanosheets based sensors exhibit an excellent reversible behavior and long-term stability. It also has higher response than that of the humidity sensor with carbon nanohoneycombs materials.

4.1 Introduction

Humidity sensors are widely used in industry and agriculture such as air conditioning systems, food quality monitoring, meteorology and medical equipment. Commercial sensors are mostly based on metal oxides [1, 2], porous silicon [3-6] and polymers [7, 8]. In these materials the adsorption of water vapor drastically changes the electrical properties, such as resistivity and capacity, of the device. Recently, carbon films have attracted great attention for their potential applications in the humidity sensors because of their large sensing area and high chemical inertness [9-11].

Various structures of electrodes have been proposed for the sensor systems. Traditionally, the humidity signals obtained using a sensor with two-electrode techniques are affected by

polarization effect. This is because of the migration of some electrons from the metal probe into the conductive samples. As a result, positive charges in the samples migrate towards the metallic probe, creating a cation layer between the metallic probe and the samples. For nanostructured carbon (n-C) based humidity sensor, the polarization effect frequently occurs under direct current (DC) circuit due to the existence of physisorption of water when relative humidity (RH) is high enough [12, 13]. Polarization effect could be caused by the migration of the H^+ ions into the metallic probe because H^+ ions appear in the physisorbed absorbed water [14-16]. To avoid or reduce this effect, four-point probes are commonly used [17, 18]. The voltage is measured on the inner electrodes without polarization effects because no current flows in the measuring circuit.

In this work we have demonstrated simple, fast response, and high sensitive resistive-type n-C based humidity sensors. The films are produced by a hot filament physical vapor deposition (HFPVD) method on Si (100) substrates with a SiO_2 buffer layer. The newly designed humidity sensors consist of n-C sensing elements combined with four-point electrodes. The sensing properties are characterized, and humidity sensing mechanism is discussed. What's more, comparisons of sensing properties of the sensors in the DC and alternative current (AC) circuits are also presented.

4.2 Experimental details

4.2.1 Preparation and characterization of the carbon nanomaterials

n-C films were synthesized on Si (100) substrates with an area of 10 mm×10 mm using a HFPVD technique in methane ambient (57.5 Pa) and vacuum, respectively. The easily-get graphite stick (0.7 mm diameter, 15 mm length) was used as a precursor to provide carbon source and filament, to replace the tungsten filament in the system described elsewhere in our previous

publications [19, 20]. No catalyst was used. After placing Si substrates, the chamber was pumped down to 2.67×10^{-3} Pa, following feeding Ar gas up to ambient pressure, it was then pumped down to 2.67×10^{-3} Pa again. Repeated this process 3 times to keep oxygen out and obtain a good vacuum. A DC power supply HY3020E with an electric current of 18 A was used to heat the graphite stick to a temperature up to 2000℃ to promote gas phase activation. The substrates were placed on a holder under the hot graphite stick. No an extra heater was used to heat the substrates. The deposition duration for each sample was 30 min.

The morphologies and chemical contents of n-C were characterized by Field Emission Scanning Electron Microscope (FESEM) and Energy-Dispersive X-ray Spectroscopy (EDS). Micro Raman scattering was performed using a Jobin-Yvon T64000 Triple-mate system with the radiation of 514.5 nm from a coherent argon ion laser and a liquid nitrogen cooled charge coupled device was used to collect and process the scattered data.

4.2.2 Preparation of sensor electrodes

After deposition of the n-C sensing materials, a four-point configuration of Au electrodes marked as 1, 2, 3 and 4 were sputtered onto the surface of as-deposited n-C sensing materials using properly desired mask. Each electrode was controlled in the thickness of 30 nm, width of 1 mm, length of 1 cm that is separated (center-to-center) by 2 mm. The illustration of the sensor is schematically shown in Fig. 4.1. Current is supplied via the outer electrodes 1 and 4. The voltage is measured across the inner electrodes 2 and 3. The contact for the Au electrodes with silver wires was made by silver paste.

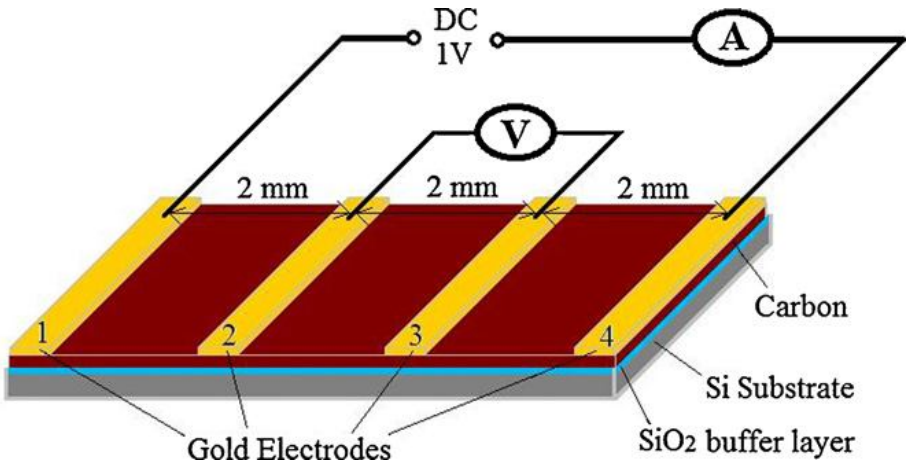

Fig. 4.1 Schematic illustration of four-point electrodes measurement of resistance between electrodes 2 and 3.

4.2.3 Measurement of sensing properties

Fig. 4.2 depicts a schematic diagram of the facility aiming at the charactering resistive-type humidity sensors. It consists of a stainless steel chamber with a volume of 1 L, pipelines and valves to transfer and control gases RH inside the test chamber, a dryer device to dry the sensors, an electrical circuit (marked as A) connected a DC (or AC) power supply with outer electrodes to offer current and a meter to measure the current flows in the circuit, and another electrical circuit (marked as B) to measure the voltage drop. The desired level of humidity was regulated by mixing different percentages of humid air and dry air, and the humidity was measured by a standard hydrothermal meter. The humidity response of the sensors was probed by monitoring the variation of the resistance of the sensors (the part between electrodes 2 and 3) in different RH environments, which was estimated based on the measurement of the electrical signals of the two testing circuits, according to the Ohm's law: $R = V/I$, where the R, V and I are the resistance, voltage drop and

the current flow of the n-C based sensors, respectively. Unless otherwise stated, the whole system was maintained at room temperature around 25 ^{0}C during measurements with a homogeneous pressure distribution inside the chamber.

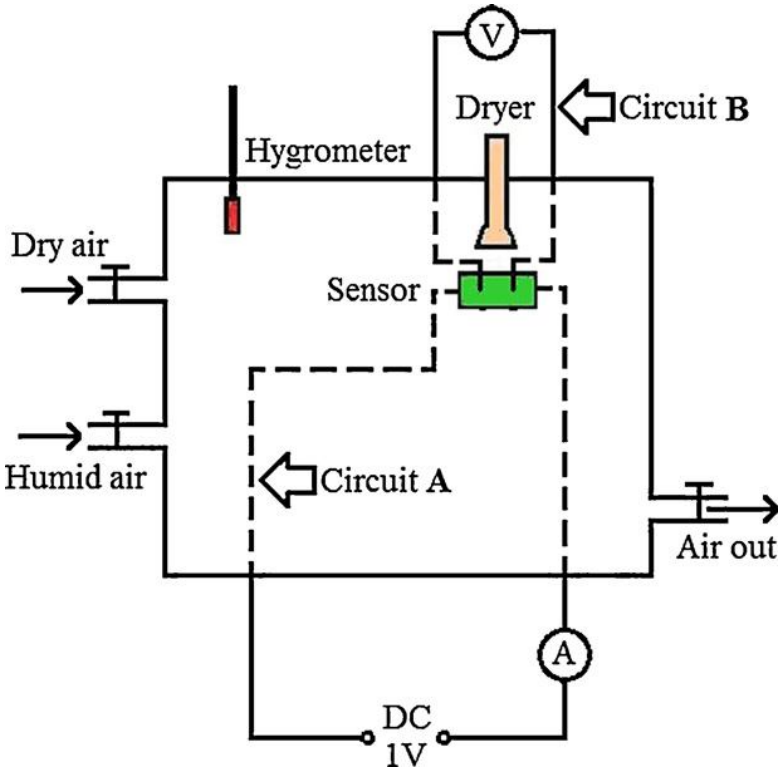

Fig. 4.2 A schematic diagram of device assembly.

4.3 Results and discussions

4.3.1 Characterizations of the carbon nanostructure

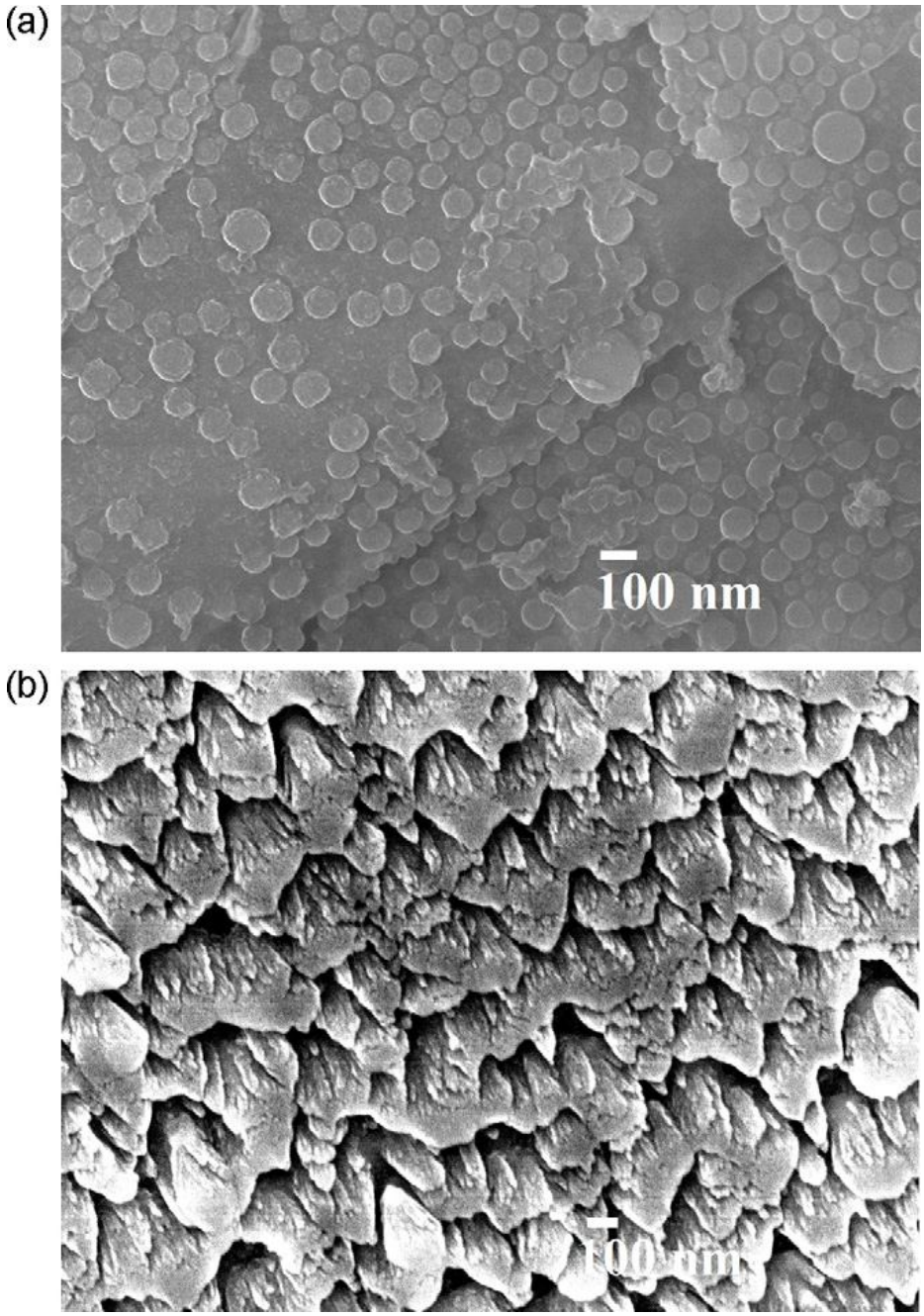

Fig. 4.3 FESEM images of carbon nanostrutcture grown (a) under methane and (b) in vacuum.

Fig. 4.3 shows the FESEM images of n-C films grown under methane (57.5 Pa) and in vacuum, respectively. The presence of nanoparticles on the surfaces of carbon nanosheets can be observed in the sample grown under methane, as shown in Fig. 4.3a. The average size of the particles is about 80 nm. These nanoparticles can be regarded as the sites that enhance the adsorption of water vapor molecules. For the sample grown in vacuum, vertically and well-organized nanohoneycomb structures are obtained (Fig. 4.3b). The thickness of the two samples is 550 and 210 nm, respectively.

Table 4.1 EDS data of the two samples

Element	Nanosheets (Atomic %)	Nanohoneycombs (Atomic %)
C K	53.08	38.09
O K	7.94	9.25
Si K	38.73	52.46
Fe K	0.09	0.07
Sn L	0.16	0.13

Table 4.1 lists the EDS data of the obtained n-C films. Besides the C element and Si (from substrate and SiO_2 buffer layer), O elements (from SiO_2 buffer layer and adsorbed by sample surface), a small quantity of Sn and Fe are also emerged. This may be due to the contamination of chamber or impurity of carbon source. The existence of the metallic elements Sn and Fe makes the synthesized samples to be p-type semiconductors, which is in accordance with previous reports [21, 22].

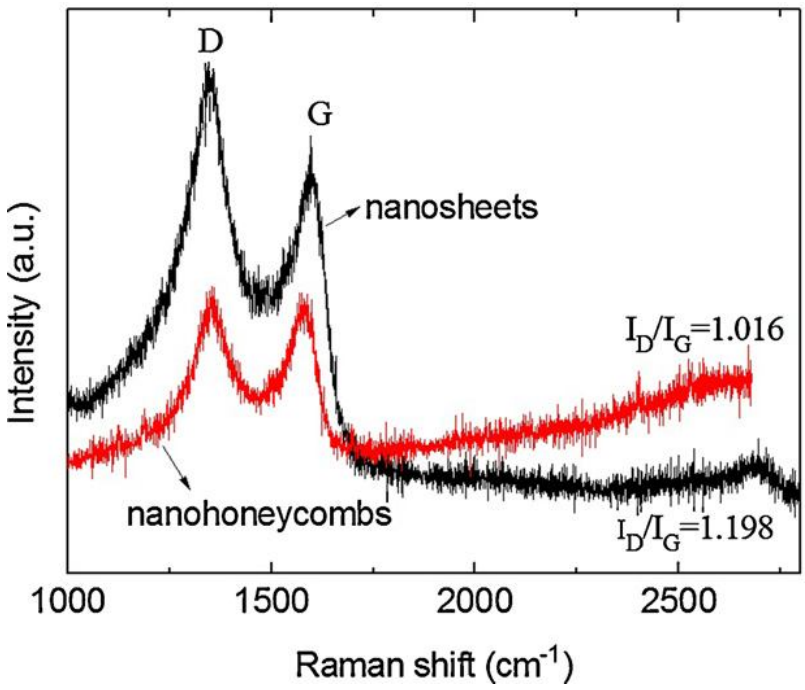

Fig. 4.4 Raman spectra of carbon nanosheets and nanohoneycombs.

Fig. 4.4 shows the Raman spectra of the carbon nanosheets and nanohoneycombs, respectively. Characteristic graphite peaks are identified in the Raman spectra between 1000 and 2800 cm^{-1}. The one at around 1350 cm^{-1}, which is called D peak, has been attributed to dislocation defects in the graphite [23]. It is associated with disorder-allowed zone edge modes of graphite that became Raman active due to the lack of long-range order in amorphous carbon based materials [24]. The G peak at around 1596 cm^{-1} corresponds to the G line associated with the optically allowed E_{2g}-zone centre of crystalline graphite [24]. The Raman signal ratio I_D/I_G is 1.198 and 1.016 for carbon nanosheets and nanohoneycombs, respectively. It suggests that the carbon nanosheets have higher defects, which could also serve as water adsorption sites, than the carbon nanohoneycombs.

4.3.2 Humidity properties of the two n-C films based sensors

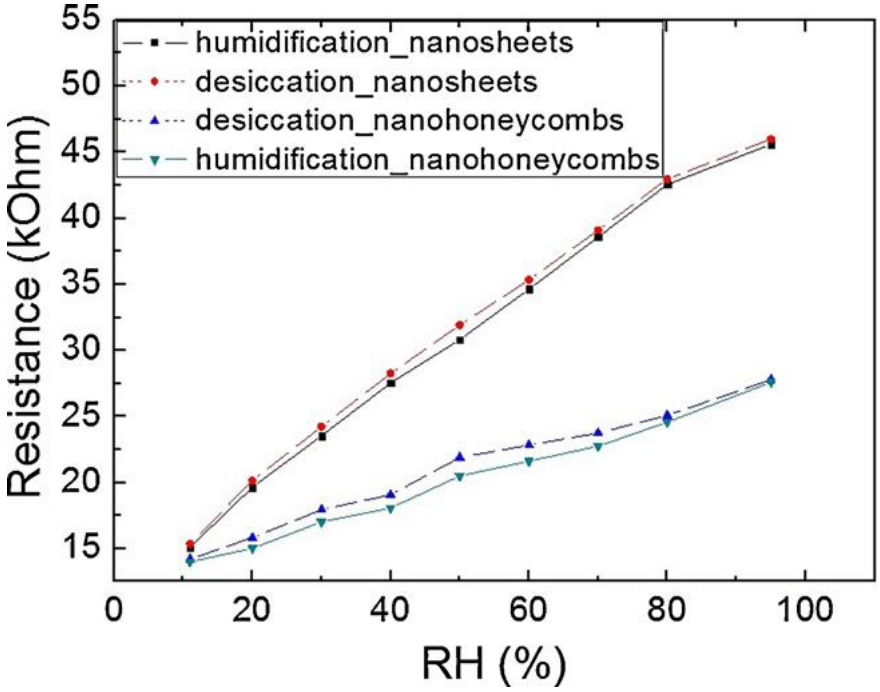

Fig. 4.5 Resistance of both sensors against RH during humidification–desiccation processes at room temperature.

After characterizations, n-C films based prototypic sensors are fabricated. A chamber was employed to provide different humidity levels in incremental steps. Each step was maintained at constant parameters till the electrical signals reading reached a steady value. The corresponding resistance change versus different humidity was monitored, as shown in Fig. 4.5. The solid lines in the figure are corresponding to the water adsorption process (humidification process), while the dashed lines indicate the desiccation process, corresponding to the desorption process. It shows that the resistance of both n-C films based sensors changes almost linearly with RH. When RH increases from 11% to 95%, the resistances of the carbon nanosheets and nanohoneycombs based sensors increase 225% and 112%, respectively.

The conductivity of p-type semiconductor is determined by holes scattering through the material. Usually carbon contains numerous oxygen derivatives on its surface, which makes the carbon surface hydrophilic and increases water vapor adsorption [16]. The adsorbed water molecules donate electrons to the valence band, therefore decreasing the number of holes and increasing the separation between the Fermi level and valence band [21, 25], and then reduce the conductivity of the p-type semiconductor. The higher the RH level, the more water molecules are adsorbed and more electrons are transferred, which would inevitably lower the holes concentration and lead to an increase of resistances of samples with RH.

The non-coincidence between the loading and unloading curves is known as hysteresis. For a perfect sensor device, its loading and unloading curves normally follow the same or almost same path. Hysteresis of resistance versus RH in the desiccation process is found in both samples. This may be caused by the different amount of water molecules adsorbed on the sensors between the humidification process and desiccation process, resulting in the difference in resistance at the same RH [26]. The maximum humidity hysteresis is about 3.57% and 6.83% under 50%RH for the carbon nanosheets and nanohoneycombs based sensors, respectively.

The response of sensor to humidity is calculated by the ratio of the resistance change occurred in a sample under exposure of the humidity to the original resistance: $S = (R_h - R_0)/R_0 \times 100\%$, where R_h refers to the resistance at certain humidity and R_0 represents the original resistance of the sensors at air of 3%RH. The obtained sensors show linear response of RH over the range of 11-95% as shown in Fig. 4.6, where the carbon nanosheets based sensor (~225% at RH 95%) has much higher response than that of the carbon nanohoneycombs based sensor(~110% at RH 95%). Water molecules could be adsorbed on surface of n-C film because the hydrogen in H_2O molecule could form a weak bond with one of the surface C atoms [26]. The nanoparticles on the surface of

the carbon nanosheets make water molecules adsorb easily. As lots of hydroxyl could be connected to the nanoparticles, they could act as sites of adsorption to water molecules. What's more, the improvement in sensing performance may be caused by the defects of the carbon nanosheets, as proved by Raman spectrum, which could also offer sites for water molecules adsorption [27, 28]. Pati et al. [29] reported that charge could transfer between the adsorbate and the n-C film. A quantitative analysis based on Mulliken approach shows a charge transfer of $0.03e^-$ from a single H_2O molecule to n-C film [25]. The more water molecules can be adsorbed on the surface, the more charge transfer happens between the water molecules and n-C. Consequently, the humidity sensing characteristics of the carbon nanosheets is better than that of the nanohoneycombs.

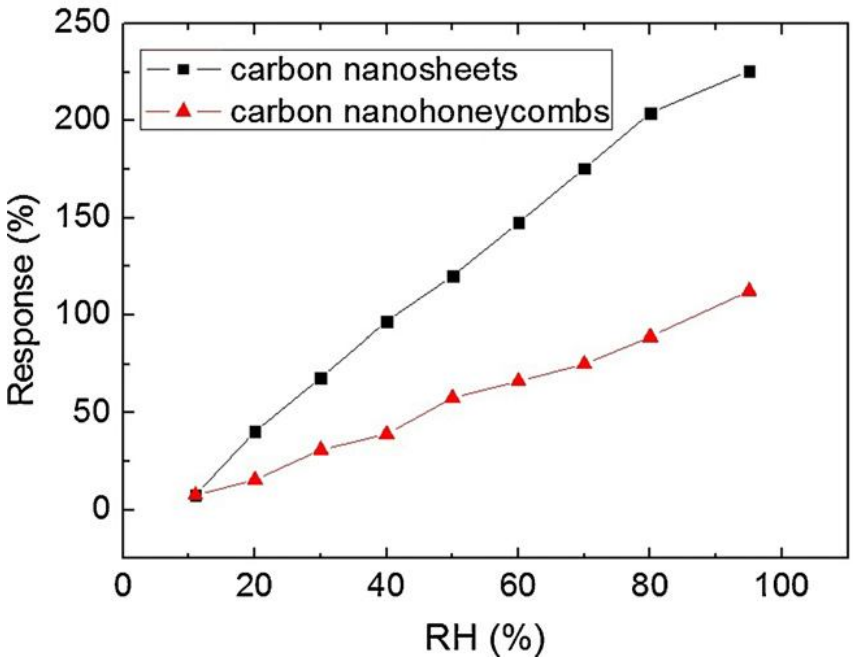

Fig. 4.6 Humidity sensing properties of carbon nanosheets and nanohoneycombs based sensors.

4.3.3 Resistance–temperature characteristic of n-C based sensors

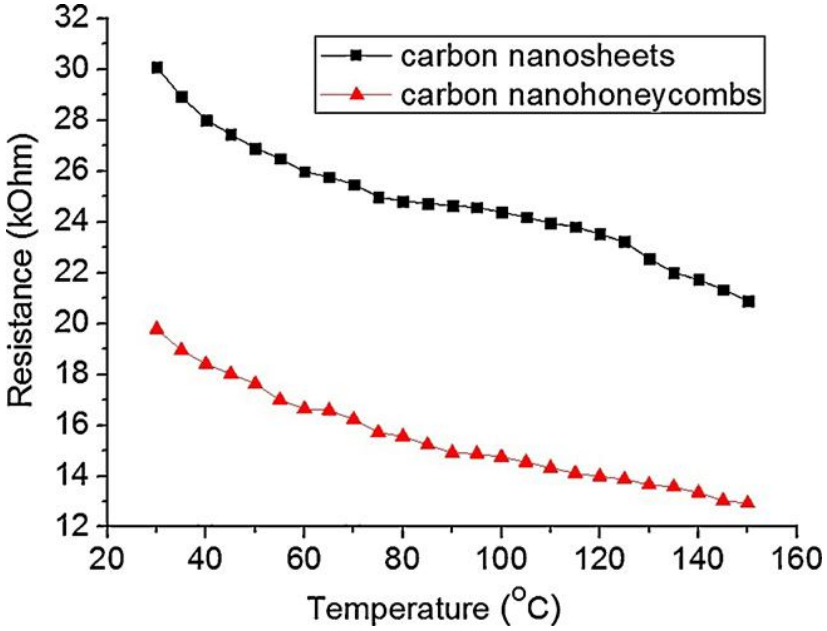

Fig. 4.7 The plot of resistance vs. temperature for carbon nanosheets and nanohoneycombs based sensors.

Fig. 4.7 depicts the resistance–temperature behavior of the two n-C films based sensors in air (RH is ~50%). The variations of resistances of both samples are strongly dependent on the temperature. Resistive values decrease following the increase of temperature. And these decreases are comparable with the change arising from the RH, so temperature compensation should be made when these films are used at different temperatures. This negative temperature effect indicates that the concentration of carrier in the samples increases when temperature increases then consequently leads to the increase of the conductivity of the samples, which results in decrease of the resistance of the film.

4.3.4 Further sensing performances of the carbon nanosheets based humidity sensors

In the following characterizations, we would mainly focus on the carbon nanosheets based sensor due to its better humidity sensing performance than that of the nanohoneycombs.

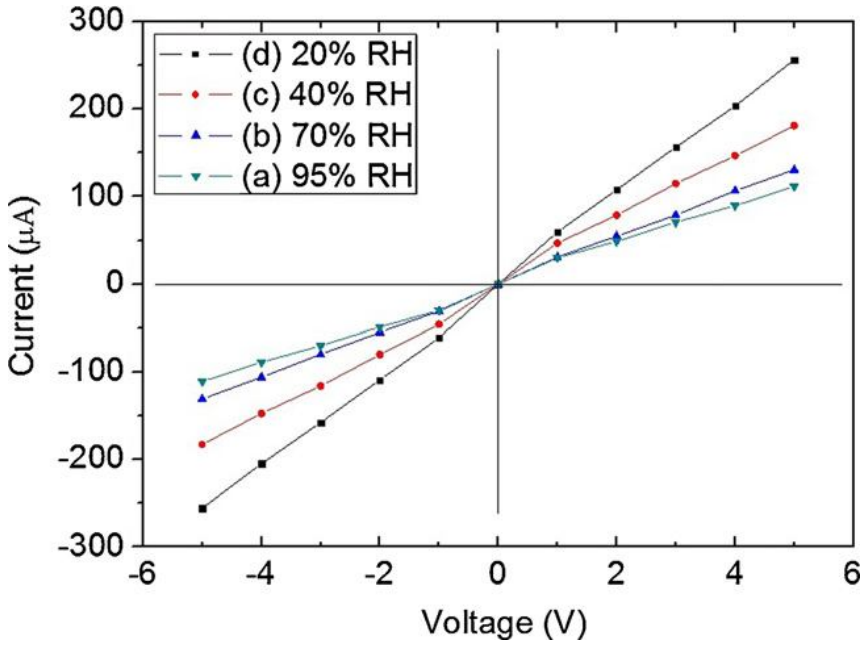

Fig. 4.8 I–V characteristics of the carbon nanosheets based sensor in different static RH atmosphere from 20% to 95%RH at room temperature.

Fig. 4.8 shows the current-voltage (I–V) characteristics measured using four-point technique at different RH for the carbon nanosheets based sensor at room temperature. The four I–V curves appear non-linear properties at the vase of low voltage (below 1 v), but become linear at higher voltage (above 1 v). This behavior may be explained by the existence of a potential barrier between the electrodes and the carbon nanosheets [30] at low voltage. The I–V characteristics were linear at high voltage, suggesting an ohmic contact between the Au electrodes and the carbon nanosheets. Based on this, we applied the DC voltage of 1 v for the sensing measurements. The ohmic contact may be attributed to closeness of the work functions of Au (5.1 eV) and carbon

(about 5 eV). From experimental data in Fig. 4.8, it can also be found that the resistance of the sensor increases with RH in air, which is in good agreement with the results shown in Fig. 4.5.

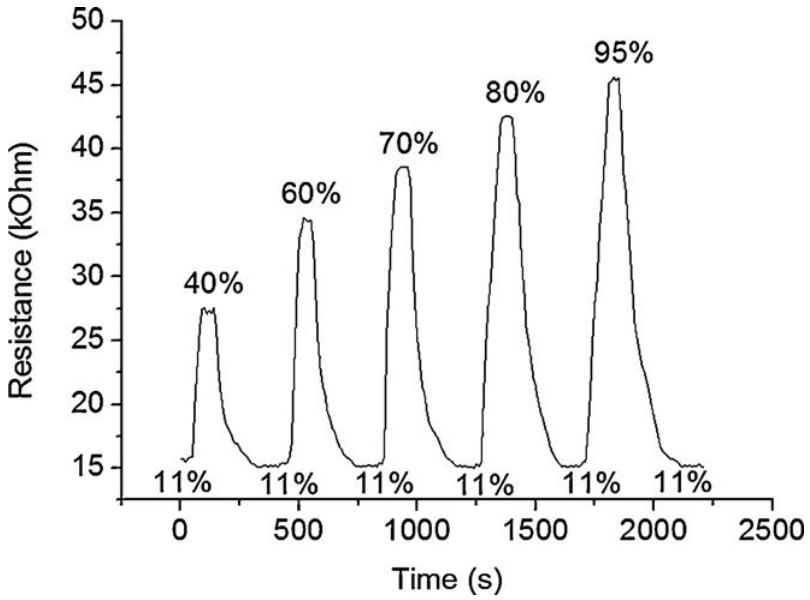

Fig. 4.9 Dynamic response of the carbon nanosheets based sensor to different RH levels.

The transient response behavior of the carbon nanosheets based sensor to dynamic switches between 11%RH and different RH levels ranging from 40% to 95%RH is given in Fig. 4.9, indicating good reversibility of the response of the sensor. When the humidity was switched to 11%RH from a high RH, the resistance abruptly decreased and then gradually reached a relatively stable value. When the sensor was exposed to high RH levels, the resistance of the sensor promptly increased and then reached a relatively stable value. So, the water-carbon interaction can be considered as physisorption with a weak bond [31].

The response time (defined as the time required to reach 90% of the total resistance change) is influenced by the change of RH level. The response time to humidification from 11% to 40%RH is about 30 s, while the recovery time from 40% to 11%RH is about 90 s, which is much faster than the results reported early [12]. Need to mention that the actual response time and recover time

should be shorter. This is because the measurement results were affected by the time delay in the valve switching and the gas exchange in the chamber. When RH increases from 40% to a higher RH, the response and recovery time slightly increases accordingly. This can be explained by the nature of the diffusion and adsorption process. There are more water molecules diffused into the structure and absorbed by the surface of sensing material at higher RH levels [32]. This results in longer response and recovery time.

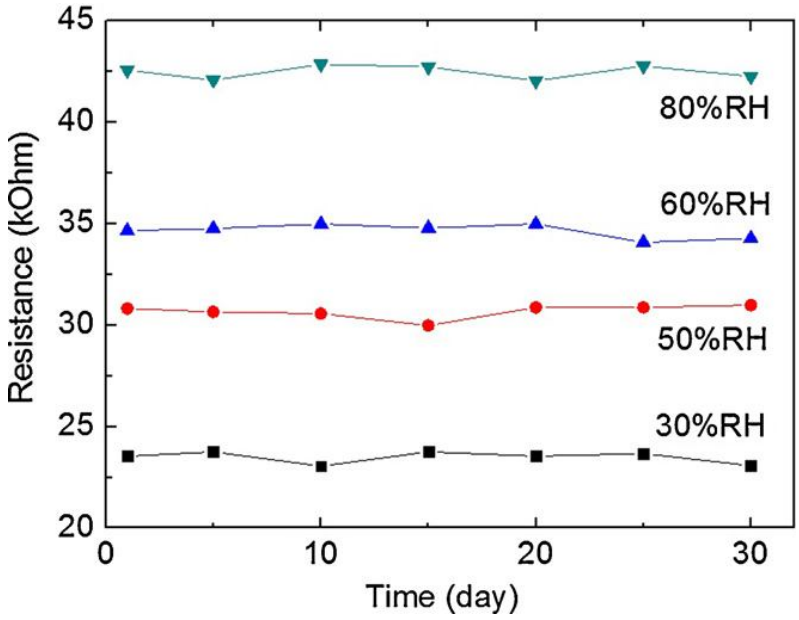

Fig. 4.10 The long-term stability of carbon nanosheets based sensor at room temperature.

In order to evaluate the reliability of the sensor, tests for long-term stability were also carried out. The results are shown in Fig. 4.10. The measurements of resistance-RH characteristics were repeated every 5 days for one month. Only slight variation in resistance at each humidity region is observed over time after aging, proving good stability and durability of the carbon nanosheets based sensor.

4.3.5 Comparison of humidity sensing performances of the carbon nanosheets based sensors using DC and AC power supplies

In order to compare the sensing performance at DC and AC systems, we replaced the DC power supply by AC power supply in electrical circuit A to measure the humidity sensing properties of the carbon based sensors. Fig. 4.11 shows the comparison of resistance and response of the carbon nanosheets and nanohoneycombs based sensors measured by using AC (1 V, 1 kHz) and DC power supply, respectively. The solid lines in both figures are corresponding to the values in DC case, while the dashed lines are corresponding to that of AC case.

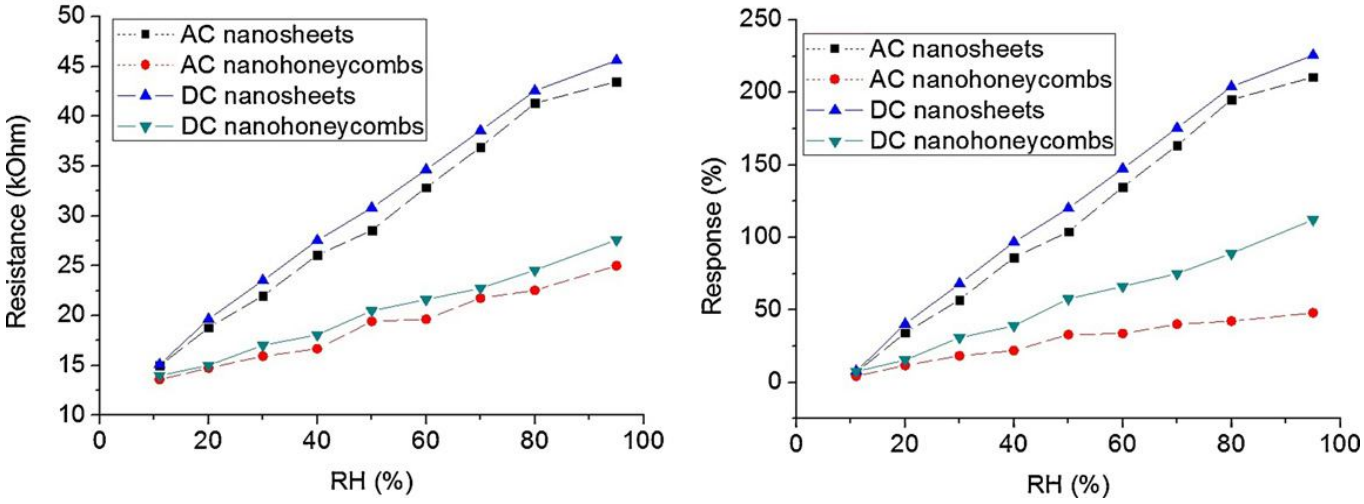

Fig. 4.11 Sensing properties comparison of n-C films based sensors using DC and AC power supplies.

At the same humidity environment, the obtained impedance values of the sensor with AC power supply are lower than the values in the case of DC circuit. Because the physisorbed water molecules on the carbon film surface have dipole moment [33, 34], the equivalent circuit of the sensor under humidity environment can be consider a parallel combination of a resistance

component of sensor material: a resistance component of physisorbed water and then a capacitance component of physisorbed water. This results in low impedance values in the case of AC circuit, as shown in Fig. 4.11a. The calculated response values of both sensors at AC and DC circuit are exhibited in Fig. 4.11b. Obviously, both sensors have higher response with DC electrical circuit than that with AC circuit.

4.4 Conclusion

In summary, the performances of carbon nanosheets and nanohoneycombs based resistive humidity sensors were measured by a four-point method. Both sensors show linear dependence of resistance and sensor response on RH. The carbon nanosheets based sensor exhibits high response in comparison with the sensor based on carbon nanohoneycombs. The response time and the recovery time of the carbon nanosheets based sensor are 30 s and 90 s at 40%RH, and the hysteresis is about 3.57% at 50%RH. What's more, good stability is observed within one month. At the same humidity environment, both carbon nanosheets and nanohoneycombs based sensors have higher sensing response with DC electrical circuit than that with AC circuit. Need to mention here, four-point method is necessarily used to avoid any possibility of polarization effect when DC power supply is employed.

Actually, carbon nanosheets and nanohoneycombs based humidity sensors are not extensively used. In the following chapter, we are going to discuss a widespread carbon nanomaterials—carbon nanotube for sensing applications.

4.5 References

[1] Z.M. Rittersma, *Sens. Actuators A* 96: (2002) 196–210 (2002)

[2] O.K. Varghese, C.A. Grimes, *J. Nanosci. Nanotech.* 3: 277–293 (2003)

[3] Z.M. Rittersma, A. Splinter, A. Bodecker, W. Benecke, *Sens. Actuators B* 68: 210–217 (2000)

[4] E.J. Connolly, G.M. O'Halloran, H.T.M. Pham, P.M. Sarro, P.J. French, *Sens. Actuators A* 99: 25–30 (2002)

[5] M. Bjorkqvist, J. Salonen, J. Paski, E. Laine, *Sens. Actuators A* 112: 244–247 (2004)

[6] J. Das, S.M. Hossain, S. Chakraborty, H. Saha, *Sens. Actuators A* 94: 44–52 (2001)

[7] F. Kraus, S. Cruz, J. Muller, *Sens. Actuators B* 88: 300–311 (2003)

[8] P.M. Harrey, B.J. Ramsey, P.S.A. Evans, D.J. Harrison, *Sens. Actuators B* 87: 226–232 (2002)

[9] J.P. Lukaszewicz, *Electron. Technol.* 33: 195–206 (2000)

[10] J.P. Lukaszewicz, *Sens. Actuators B* 60: 184–190 (1999)

[11] J.P. Lukaszewicz, M. Panas, J. Siedlewski, *Sens. Actuators B* 32: 221–226 (1996)

[12] Q.Y. Tang, Y.C. Chan, K.L. Zhang, *Sens. Actuators B* 152: 99–106 (2011)

[13] J.P. Lukaszewicz, M. Skompska, *Sens. Actuators B* 113: 970–977 (2006)

[14] J.H. Anderson, G.A. Parks, *J. Phys. Chem.* 72: 3362–3368 (1968)

[15] W.M. Sears, *Sens. Actuators B* 67: 161–172 (2000)

[16] S. Pokhrel, K.S. Nagaraja, *Sens. Actuators B* 92: 144–150 (2003)

[17] E. Hesse, *Solid-State Electron.* 21: 637–641 (1978)

[18] J. Wtorek, L. Jozefiak, A. Polinski, J. Siebert, *IEEE Trans. Biomed. Eng.* 49: 240–246 (2002)

[19] P.X. Feng, X.P. Wang, H.X. Zhang, B.Q. Yang, Z.B. Wang, A. Gonzalez-Berrios, G. Morell, B. Weiner, *J. Phys. D: Appl. Phys.* 40 : 5239–5245 (2007)

[20] X.P. Wang, B.Q. Yang, H.X. Zhang, P.X. Feng, *Nanoscale Res. Lett.* 2: 405–409 (2007)

[21] J. Kong, N.R. Franklin, C.W. Zhou, M.G. Chapline, S. Peng, K. Cho, H.J. Dai, *Science* 287 : 622–625 (2000)

[22] O.K. Varghese, P.D. Kichambre, D. Gong, K.G. Ong, E.C. Dickey, C.A. Grimes, *Sens. Actuator B* 81: 32–41 (2001)

[23] X.J. Huang, Y.F. Sun, L.C. Wang, F.L. Meng J.H. Liu, *nanotechnology* 15: 1284–1288 (2004)

[24] H.Y. Li, Y.C. Shi, P.X. Feng, *Appl. Phys. Lett.* 89: 142901 (2006)

[25] A. Zahab, L. Spina, P. Poncharal, C. Marliere, *Physical Review B* 62: 10000–10003 (2000)

[26] C.L. Cao, C.G. Hu, L. Fang, S.X. Wang, Y.S. Tian, C.Y. Pan, *J. Nanomater.* 707303 (2011)

[27] X. Feng, S. Irle, H. Witek, K. Morokuma, R. Vidic, E. Borguet, *J. Am. Chem. Soc.* 127: 10533–10538 (2005)

[28] Z.E. Horvath, A.A. Koos, K. Kertesz, G. Molnar, G. Vertesy, M.C. Bein, T. Frigyes, Z. Meszaros, J. Gyulai, L. P. Biro, *Appl. Phys. A* 93: 495–504 (2008)

[29] R. Pati, Y. Zhang, S.K. Nayak, P.M. Ajayan, *Appl. Phys. Lett.* 81: 2638–2640 (2002)

[30] Q. Chen, S. Wang, L.M. Peng, *Nanotechnology* 17: 1087–1098 (2006)

[31] Z.G. Zhao, X.W. Liu, W.P. Chen, T. Li, *Sens. Actuator A* 168: 10–13 (2011)

[32] Y. Wang, S. Park, J.T.W. Yeow, A. Langner, F. Muller, *Sens. Actuator B* 149: 136–142 (2010)

[33] H.J. Chen, Q.Z. Xue, M. Ma, X.Y. Zhou, *Sens. Actuator B* 150: 487–489 (2010)

[34] J. Wang, F.Q. Wu, K.H. Shi, X.H. Wang, P.P. Sun, *Sens. Actuator B* 99: 586–591 (2004)

Chapter 5

Characterization and applications of carbon nanotubes

In this chapter, conductive composite films of carbon nanotubes (CNTs) were prepared in two different ways using the biopolymer kappa- carrageenan (KC) as a dispersant. Evaporative casting and vacuum filtration film-formation processes were compared using electrical characteristics. These measurements showed that, films produced using vacuum filtration had higher electrical properties than those prepared using the evaporative casting method. These evaporative casted MWCNTs composite films also performed as the best humidity sensor over all other films measured.

5.1 Introduction

Carbon nanotubes (CNTs) have attracted many researchers duo to their unique electronic, mechanical, optical and thermal properties which make them suitable for current and future application in nanotechnology [1-4]. Humidity sensors are widely applied in process control, environment monitoring, storage, electrical devices, and so forth, and the research to develop some new materials for sensor device attracts more and more attention [5]. CNTs are considered to be a novel humidity sensing materials owing to their large surface area to volume ratio [6], high chemical inertness, nanoscale structure and hollow center [5, 7]. Many researchers have studied the effects of humidity on the electrical conductivity of SWCNTs [8-10] and it has been reported that the water molecules act as a donor and modify the electrical properties of SWCNTs [11-14]. In multi walled carbon nanotubes (MWCNTs), when exposed to the humidity, impedance changes were also observed which could be attributed to the *p*-type conductivity of MWCNTs [15]. Further, it is also reported that the height of Schottky barrier formed between *p*-type MWCNTs and a

metallic electrode changes with changing values of ambient humidity [16, 17]. Varghese et al. [18], Valentini et al. [19], and Cantalini et al. [11] have investigated the gas sensitive characteristics of MWCNTs systematically and observed humidity sensitivity of MWCNTs briefly. CNT-based humidity sensors have been demonstrated to be more sensitive and faster response in detecting humidity [7].

In this work, the effect of preparation method and presence of glycerin on the electrical and humidity sensing properties were investigated.

5.2 Experimental details

Kappa-carrageenan (KC) –CNTs including KC–SWCNTs and KC–MWCNTs with or without glycerin (G) were prepared using evaporative casting method (A1-A4) and vacuum filtration method (B5-B7) (table 5.1) by our collaborator Dr. Marc in het Panhuis and Dr. Ali Aldalbahi from Soft Materials Group, School of Chemistry, and ARC Centre of Excellence for Electromaterials Science, University of Wollongong, Australia, see the details in [20].

Table 5.1 Sample information. Numbers for dispersions indicate the concentration of biopolymer and CNT, i.e. "KC-0.50-MWCNT 0.10" corresponds to dispersion with KC and MWCNT concentration of 0.50 % w/v and 0.10% w/v, respectively.

Film	Dispersion
A1	KC 0.50 – MWCNT 0.10
A2	KC 0.50 – MWCNT 0.10 + 50%G
A3	KC 0.50 – SWCNT 0.10
A4	KC 0.50 – SWCNT 0.10 + 50%G
B5	KC 0.15 – MWCNT 0.03
B6	KC 0.15 – MWCNT 0.03 + 50%G
B7	KC 0.15 – SWCNT 0.03
B8	KC 0.15 – SWCNT 0.03 + 50%G

5.3 Characterization of synthesized carbon nanotubes

5.3.1 The morphologic surface

Fig. 5.1 show SEM images acquired using a JEOL JSM-7500F Field Emission Scanning Electron Microscope. Samples were prepared by mounting small pieces of films onto a brass stage using double-sided conductive carbon tape. CNTs with diameters about 10 nm (A1, A2, B5, B6) and 5 nm (A3, A4, B7, B8) were observed in all samples. The samples prepared by using vacuum filtration method exhibited higher density than the samples prepared by evaporative casting method. The background of the CNTs are KC and KC + G, respectively.

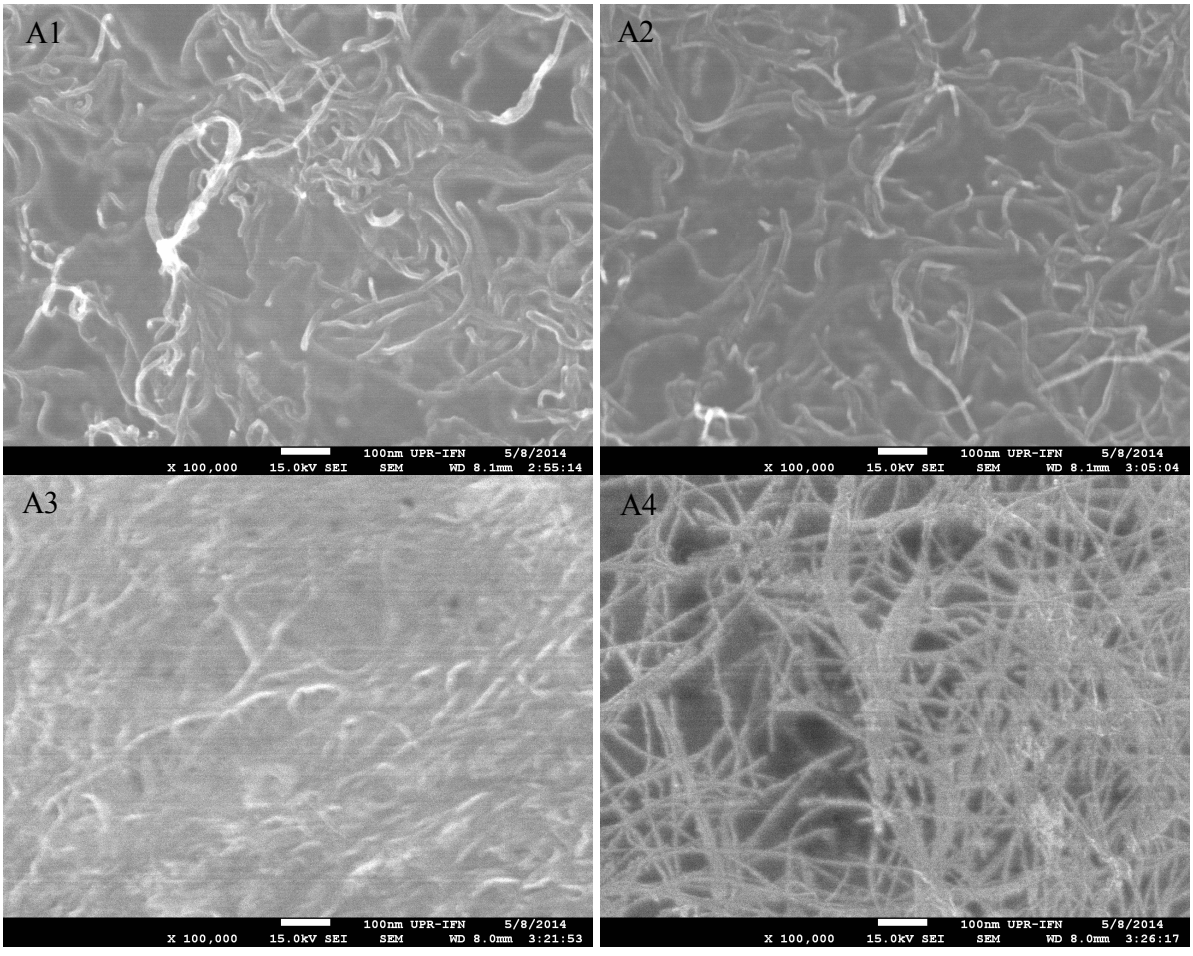

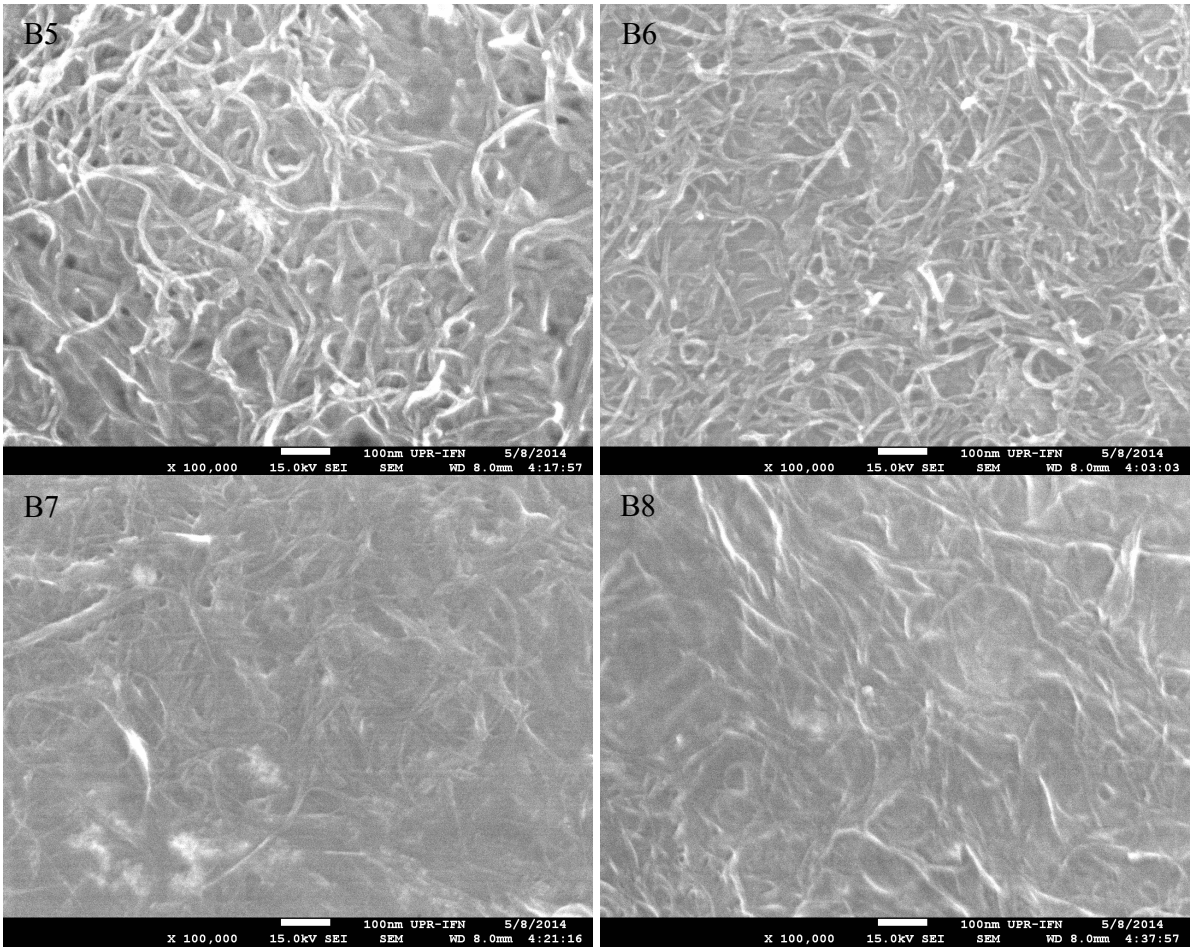

Fig. 5.1 SEM images of KC-CNT with or without G composite films prepared by evaporative casting method (A1-A4) and vacuum filtration method (B5-B8), respectively.

5.3.2 Raman spectroscopy

Raman spectroscopy yield information about the purity, defects and tube alignment, and assists in the distinction the presence of MWCNTs relative to other carbon allotropes. The technique has been strikingly successful at describing the structural properties of SWCNTs [21]. Unfortunately, the interpretation of the spectra from a MWCNT is often very complicated and has not yet yielded the same level of output as Raman spectroscopy has achieved for SWCNTs. For

Raman scattering, MWCNTs can be said to be an ensemble of carbon nanotubes with diameters ranging from small to very large [21]. Despite this, a number of reports have indicated that Raman spectroscopy can have qualitative and even quantitative characterization power. Because much less theoretical work has been devoted to understanding the Raman spectrum of MWCNTs, the interpretation of the experimental spectra is usually based on well-established results obtained for SWCNTs. This approach has proven valuable but has also shown important limitations since a number of effects, absent in SWCNTs, are often found in the spectra of MWCNTs [22].

The typical spectrum of a SWCNT has the following major features [22]:

(1) A low-frequency peak (<200 cm^{-1}), assigned to the A_{1g} symmetry radial breathing mode (RBM). This peak is absent in graphite and is the main signature of a SWCNT. The frequency of this mode depends only on the tube diameter, but the complete description of tube chiral indices can be inferred from resonant Raman measurements by using information tabulated in the Kataura plot for allowed excitations [23, 24].

(2) A group of peaks around 1340 cm^{-1}, called the D band, is assigned to the presence of disorder in graphitic materials. The origin of the D band in nanotubes is often considered as a measure of disorder as in graphite. It was also demonstrated that the D band was active for nanotubes satisfying a certain chirality due to double resonance conditions [25, 26].

(3) A group of peaks in the 1550–1600 cm^{-1} range constitutes the G band. In graphite, a single peak is present at 1582 cm^{-1} and corresponds to the tangential vibrations of the carbon atoms. This peak is a good measure of the graphitization of the sample. In nanotubes, this G band is composed of two features (G+ and G-) due to the confinement of the vibrational wave in the circumferential direction. Because the G+ band corresponds to atomic displacements along the nanotube axis, it is independent of the diameter, as opposed to the G- band, which corresponds to circumferential

atomic displacements. The G- band has a different line shape for semiconducting and metallic systems.

(4) A line is present around 2600 cm^{-1}, it is an overtone or second-order harmonic of the Dmode. It is labeled G' or sometimes D* or 2D. The G' band is indicative of long range order in a sample, and arises from a two-phonon, second-order scattering process that results in the creation of an inelastic phonons.

(5) Some second-order modes are also visible in the 1700–1800 cm^{-1}, but have not attracted particular attention, in part because of their relatively low intensity.

Raman spectroscopy on MWCNTs has been focused on exploiting the presence or absence of these bands in the corresponding spectra to infer electronic and structural information about the tube. In many samples of MWCNTs, the G band's frequency and lineshape are comparable to those of the E_{2g} phonon of graphite (though graphite linewidth is typically smaller than that for MWCNTs). The linewidth is, however, not a reliable criterion to distinguish MWCNTs from graphite, since the linewidth may be affected by a number of factors such as tube diameter. The signature of a single-shell vibration is expressed by the presence of a low frequency RBM and in the splitting of the G band. I most cases, these two effects are not observed in MWCNTs, even for highly ordered samples. The main reason is that the innermost shell in MWCNTs often has a diameter in excess of 2 nm. For such a size range, the RBM's scaling rules derived for SWCNTs indicate that the RBM frequency and intensity are not measurable. This also applies to the scaling rules for the G- band. In other words, for shells of small curvature, the electronic properties differ little from those of flat graphite. It follows that typical MWCNT spectra resemble those of graphite and display little or any effect of cylindrical geometries. This also indicates that the spectral feature of this G mode can often be used to distinguish between MWCNTs and SWCNTs: while

the G band is clearly split into two bands in SWCNTs, the G band is typically made up of a broad asymmetric feature in MWCNTs [22].

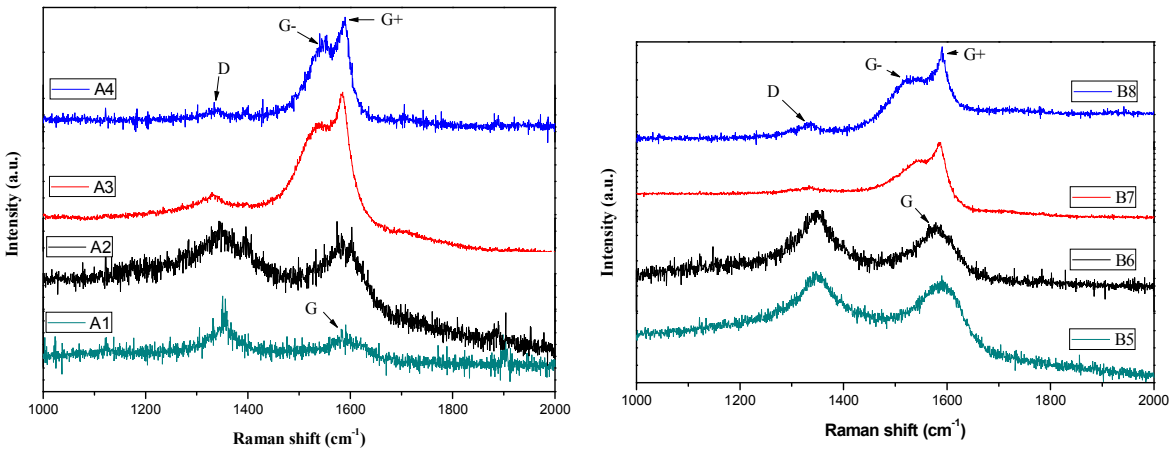

Fig. 5.2 Raman spectroscopy of KC-CNTs films prepared by evaporative casting method (A1-A4) and vacuum filtration method (B5-B8), respectively.

Fig. 5.2 show the Raman spectra of the CNTs. Characteristic peaks are identified in the Raman spectra between 1000 and 2000 cm^{-1}. The one at around 1340 cm^{-1} called the D band is associated with disorder allowed zone edge modes of graphite that became Raman active due to the lack of long range order in amorphous carbon based materials. The G band at around 1590 cm^{-1} corresponds to the G line associated with the optically allowed E_{2g} zone centre of crystalline graphite [27]. Two separated G band were observed in MWCNTs which are called G+ and G- band, respectively. It is also noted that the Raman signal ratio I_D/I_G of MWCNTs is much higher than that of SWCNTs.

5.3.3 FTIR spectroscopy

Fourier transform infrared spectroscopy (FTIR) is commonly used to investigate

functionalization. The extent of functionalization will alter the wettability of the nanotubes in various surfactants and may thus also alter the toxicity [22].

FTIR studies have been performed in the range 600 to 4000 cm^{-1} for the identification of the CNTs, as shown in Fig. 5.3. The dominant peaks at ~3300-3375 associated with O-H stretch [22, 24, 26]. The peaks located at ~2890 and 2930 cm^{-1} are corresponding C-H stretches [24, 26]. Other peaks at ~1235 and 1220 cm^{-1} are observed as C=C stretch and D band, respectively.

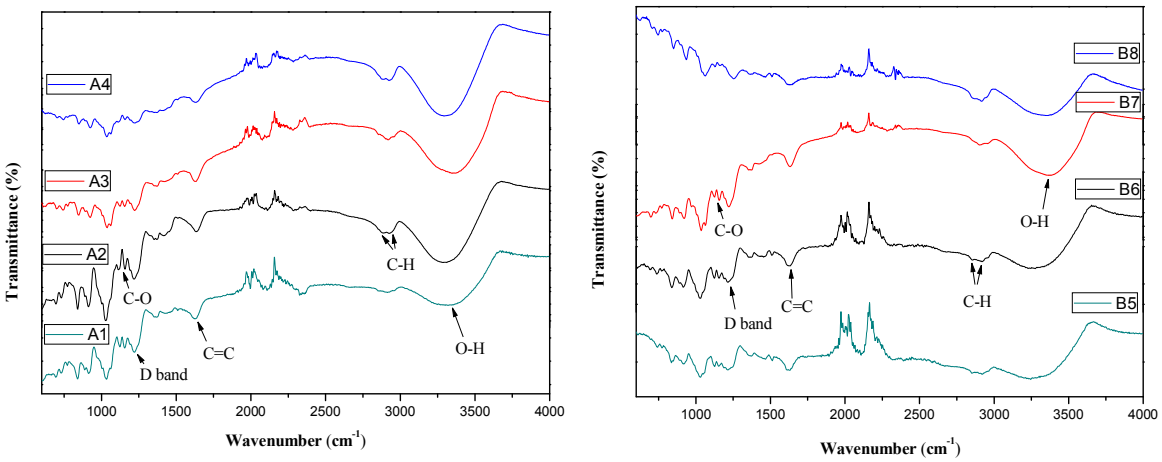

Fig. 5.3 FTIR spectrum of KC-CNTs composite films prepared by evaporative casting method (A1-A4) and vacuum filtration method (B5-B8), respectively.

5.3.4 Electrical conductivity of films

Characterization of electrical current-voltage (I-V) properties is based on HP – Agilent 6268B Power Supply and keithley 6517A electrical meter controlled by Labview program. I-V curves of selected CNTs are shown in Fig. 5.4. All films exhibited linear I-V characteristics, i.e. Ohmic behaviour. SWCNTs showed better conductivity than MWCNTs. Samples prepared by vacuum filtration method exhibited better conductivity than samples prepared by evaporative casting method. KC-CNTs composite films with glycerin had better conductivity than films without glycerin.

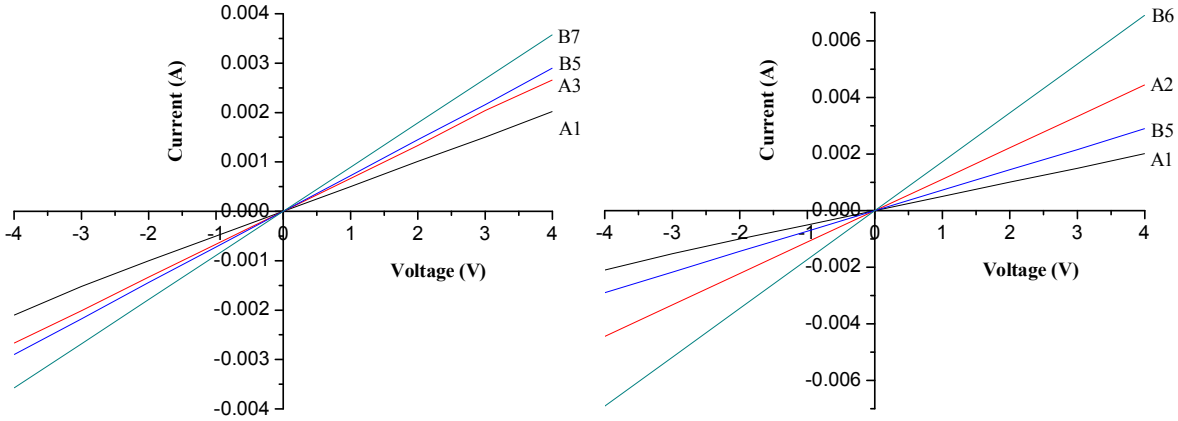

Fig. 5.4 I-V characteristics for KC-CNT composite films prepared by evaporative casting and vacuum filtration of KC-CNT dispersions.

5.3.5 Sensing properties of films

Sensing properties of the films were investigated using a custom-build system [28]. The films are connected in series to a known resister (909 Ω) and a battery (4.91 V) to form a voltage-current-resistor (*V-I-R*) electrical circuit as a prototype sensor. The sensitivity of the sensors was characterized using measurements of voltage drop across the known resistor and film under different environmental conditions, i.e. as a function of temperature and humidity, and by exposure to different gases (H_2 and CH_4) at a concentration of 100 ppm in air. For all measurements air was used as the carrier gas. The volume of chamber is 1000 ml to ensure that the change of gas concentration was instantaneous, which is a prerequisite condition for the accurate measurements of response and recovery time of the sensor.

By measuring the variation in resistance upon changing the environment of the films, the sensitivity (*S*) can be calculated using the following equation [29]:

$$S(\%) = \left(\frac{\left| R_g - R_a \right|}{R_a} \right) \times 100\% \quad (1)$$

where R_g and R_a represent the resistance of the film in the targeted gas (humidified air, H_2 and CH_4) and air, respectively.

Fig. 5.5 depicts the resistance–RH behavior of the KC-CNT composite films prepared by evaporative casting method. The resistance decreased with introduced water vapour. Table 5.2 shows the detailed parameters.

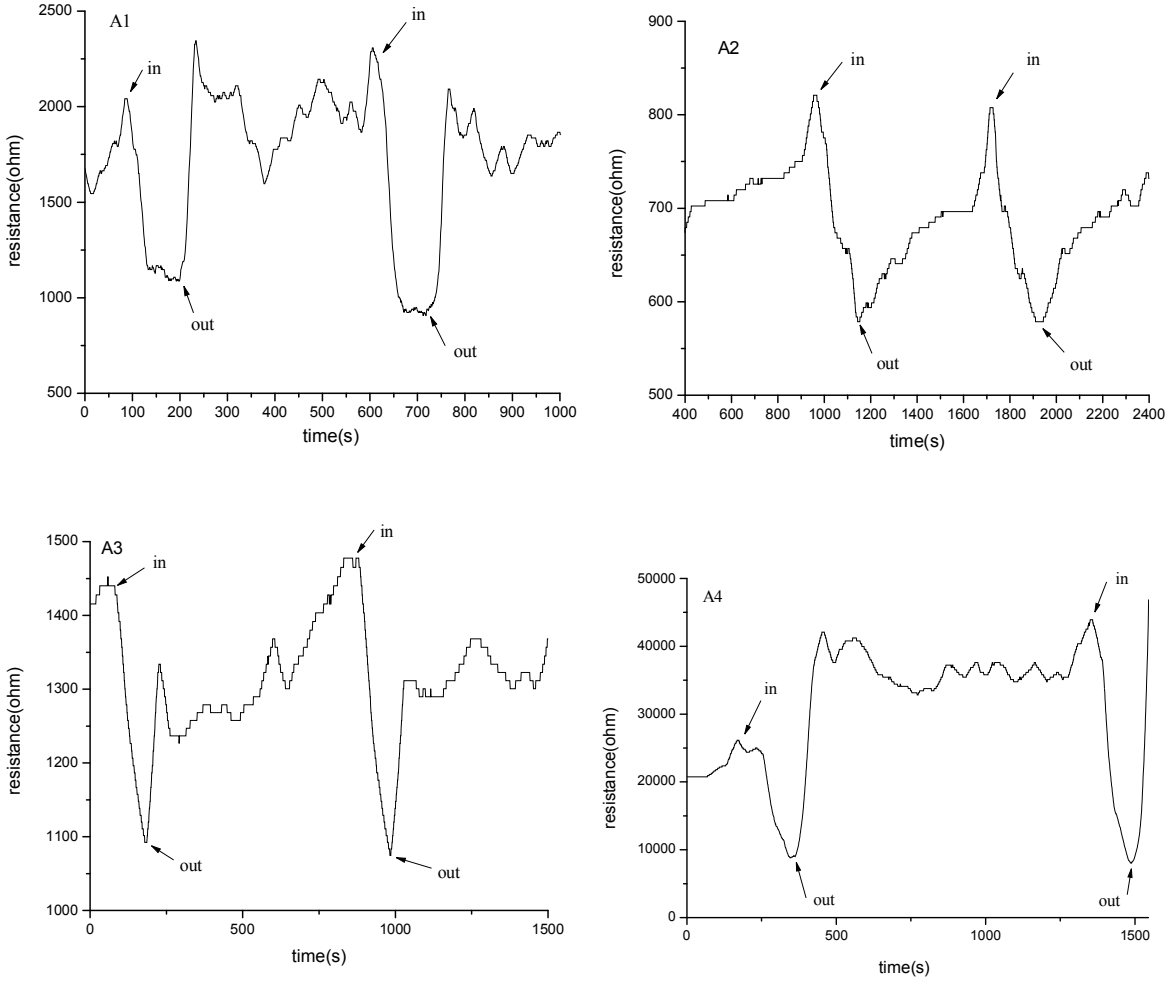

Fig. 5.5 Resistance change based on RH of CNT films prepared by evaporative casting method.

Table 5.2 Detailed parameters of Fig. 5.5

Sample	Vapor in time(s)	Humidity Change(HC)	Vapor out time(s)	in	HC	out
A1	80	55-80%	210	600	56-82%	730
A2	950	46-90%	1100	1700	46-90%	1850
A3	100	46-90%	250	700	46-90%	850
A4	150	50-90%	350	1320	50-90%	1500

In order to measure the sensitivity of the films to humidity, the resistance was measured for a humidity change from 40 - 90%. This was carried out for films containing both MWCNTs and SWCNTs prepared by evaporative casting and vacuum filtration methods. It can be seen that the sensitivity of KC-MWCNT films was higher than that of KC-SWCNT; this is shown by a greater decrease in resistance for the films containing MWCNTs. The MWCNT films exhibited a sensitivity of 70% compared to 21% for SWCNT films (Fig. 5.6). Films prepared using vacuum filtration method had a lower sensitivity of 17% and 15% for MWCNT and SWCNT films, respectively. This could be attributed to the vacuum filtration process which leads to biopolymer losses compared to the evaporative casting method of film preparation. The films were also exposed to H_2 and CH_4 gases at 25℃, however no response in resistance was observed, indicating that they were not sensitive to these gases.

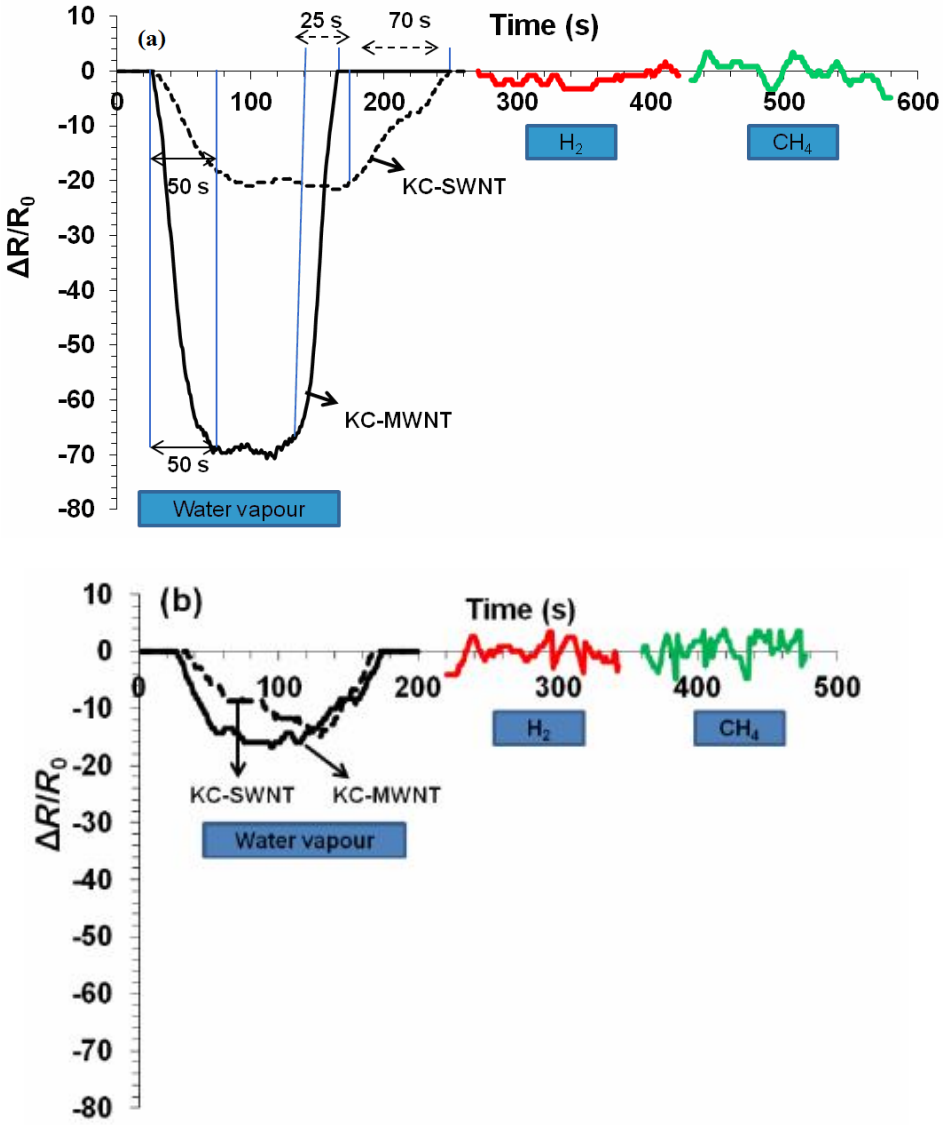

Fig. 5.6 Responses of KC–MWCNT and KC–SWCNT composite films to humidity change, H_2 and CH_4 gases (100 ppm in air) at operating temperature of 25℃. Films prepared by (a) evaporative casting and (b) vacuum filtration methods. Continuous and dashes arrows indicate the response and recovery time, respectively.

5.4 Conclusion

KC–SWCNTs and KC–MWCNTs were successfully synthesized by using evaporative casting and vacuum filtration methods. KC–MWCNT films prepared by evaporative casting process displayed higher conductivity compared to KC–SWCNT films. The conductivity of films

prepared by vacuum filtration method was higher than films prepared by evaporative casting. MWCNT films exhibited sensitivity to humidity as high as of 70%, easily outperforming SWCNT films. This work contributes toward the development of conducting biopolymer composite materials.

5.5 References

[1] M.S. Dresselhaus, *Science of fullerenes and carbon nanotubes*. San Diego: Academic Press (1996)

[2] A. Jorio, G. Dresselhaus and M. Dresselhaus, *Carbon nanotubes : advanced topics in the synthesis, structure, properties and applications*. Berlin: Springer-Verlag (2008)

[3] R. Saito, *Physical properties of carbon nanotubes*. London: Imperial College Press (1998)

[4] M. in het Panhuis, *Journal of Materials Chemistry* 16(36): 3598-3605 (2006)

[5] C.L. Cao, C.G. Hu, L. Fang, S.X. Wang, Y.S. Tian and C.Y. Pan, *Journal of Nanomaterials*: 707303 (2011)

[6] M. Cinke, J. Li, B. Chen et al., *Chemical Physics Letters* 365: 69–74 (2002)

[7] Z.G. Zhao, X.W. Liu, W.P. Chen, T. Li, *Sensors and Actuators A* 168: 10–13 (2011)

[8] A. Zahab, L. Spina, P. Poncharal and C. Marliere, *Physical Review B* 62: 10000–10003 (2000)

[9] R. Pati, Y. Zhang, S.K. Nayak and P.M. Ajayan, *Applied Physics Letters* 81: 2638–2640 (2002)

[10] J.W. Han, B. Kim, J. Li, and M. Meyyappan, *J. Phys. Chem. C* 116: 22094−22097 (2012)

[11] C. Cantalini, L. Valentini, I. Armentano, L. Lozzi, J. M. Kenny and S. Santucci, *Sens. Actuators B* 95: 195-202 (2003)

[12] P. S. Na and H. Kim, *Appl. Phys. Lett.* 87: 093101 (2005)

[13] M. Rinkio, M.Y. Zavodchikova, P. Torma and A. Johansson, *Phys. Stat. Sol. (b)* 245: 2315 (2008)

[14] D. Tang, L. Ci, W. Zhou and S. Xie, *Carbon* 44: 2155 (2006)

[15] D.B. Hibbert, *Introduction to Electrochemistry*, Mackays of Chatham PLC Chatham, Kent (1993)

[16] S.M. Sze, *Semiconductor Devices*. Physics and Technology, John Wiley & Sons, New York

(1985)

[17] Kh.S. Karimov, M.M. Ahmed, Z.M. Karieva, M. Saleem, A. Mateen and S.A. Moiz, *Sensor Lett.* 9 (5): 1-5 (2011)

[18] O.K. Varghese, P.D. Kichambre, D. Gong, K.G. Ong, E.C. Dickey and C.A. Grimes, *Sensors and Actuators B* 81: 32–41 (2001)

[19] L. Valentini, I. Armentano, J.M. Kenny, C. Cantalini, L. Lozzi and S. Santucci, *Applied Physics Letters* 82: 961–963 (2003)

[20] A. Aldalbahi, J. Chu, P. Feng and M. in het Panhuis , *Beilstein J. Nanotechnol.* 3: 415–427(2012)

[21] A. Jorio, M.A. Pimenta, A.G. Souza, R. Saito, G. Dresselhaus, M.S. Dresselhaus, *New J. Phys.* 5:139.1–17 (2003)

[22] J.H. Lehman, M. Terrones, E. Mansfield, K.E. Hurst,V. Meunier, *Carbon* 49: 2581–2602 (2011)

[23] A.M. Rao, E. Richter, S. Bandow, B. Chase, P.C. Eklund, K.A. Williams, *et al.*, *Science* 27:187–191 (1997)

[24] U.J. Kim, C.A. Furtado, X.M. Liu, G. Chen, and P.C. Eklund, *J. AM. CHEM. SOC.* 127: 15437-15445 (2005)

[25] J. Maultzsch, S. Reich, C. Thomsen, *Phys. Rev. B* 64(12):121407-1–4 (2001)

[26] S. Hussain, P. Jha, A. Chouksey, R. Raman, S. S. Islam, T. Islam, P. K. Choudhary, Harsh, *Journal of Modern Physics* 2: 538-543 (2011)

[27] H.Y. Li, Y.C. Shi, P.X. Feng, *Appl. Phys. Lett.* 89: 142901 (2006)

[28] P.X. Feng, H.X. Zhang, X.Y. Peng, M. Sajjad and J. Chu, *Review of Scientific Instruments* 82(4): 043303 (2011)

[29] X.Y. Peng, M. Sajjad, J. Chu, B.Q. Yang and P.X. Feng, *Applied Surface Science* 257(11): 4795-4800 (2011)

Chapter 6

Summary and suggestions for future works

In this thesis, a systematic study was carried out on the synthesis and characterizations of carbon nanomaterials, including carbon nanorods, carbon nanosheets, carbon nanohoneycombs and carbon nanotubes, for a purpose of developing efficient field emission displays, humidity sensors…. Different growth techniques such as hot filament physical vapour deposition, evaporative casting and vacuum filtration methods were applied to synthesize carbon nanomaterials. The morphology, chemical compositions, bond structures, electronic, mechanical and sensing properties of the obtained samples were characterized.

Well aligned one-dimensional tilted well-aligned carbon micro- and nano- hybrid rods were synthesized on Si at different substrate temperatures and incident angles of carbon source beam by using a simple hot filament physical vapour deposition (HFPVD) technique. The growth process has two remarkable features: firstly, this method can produce uniformly tilted carbon micro- and nanorods with a controllable angle; secondly, the experimental setup is simple and cost effective which satisfies the requirements of commercial applications. SEM images exhibit that micro-sized rods with different diameters are obtained for different substrate temperatures. The oblique angle and the density of the fabricated carbon rods are influenced by the incident angle of carbon source beam. The carbon nanorods with diameter of 25-35 nm are also obtained at the shadow areas. The turn-on field E_t of samples *a*, *b*, *c* is 9.1 V/μm, 5.8 V/μm and 0.4 V/μm. The field enhancement factor β increases following the increasing of substrate temperature from 800℃ to 1000℃ which is in accord with the Raman signal ratio I_D/I_G.

Carbon nanosheets and nanohoneycombs were also synthesized on Si substrates using the

HFPVD technique under methane ambient and vacuum, respectively. A simple, fast response, and high sensitive resistive-type nanostructured carbon (n-C) based humidity sensors was demonstrated. The newly designed humidity sensors consist of n-C sensing elements combined with four-point electrodes which were sputtered on the surface of the n-C films. The sensing properties of prototypical sensors at different temperature, humidity, direct current (DC), and alternative current (AC) voltage were characterized. Linear sensing response of sensors to relative humidity (RH) ranging from 11% to 95% is observed at room temperature. Experimental data indicate that the carbon nanosheets based sensors exhibit an excellent reversible behavior, higher responses and long-term stability in comparison with the sensor based on carbon nanohoneycombs. The response time and the recovery time of the carbon nanosheets based sensor are 30 s and 90 s at 40%RH, and the hysteresis is about 3.57% at 50%RH. At the same humidity environment, both carbon nanosheets and nanohoneycombs based sensors have higher sensing response with DC electrical circuit than that with AC circuit.

Free-standing conductive composite films of carbon nanotubes (CNTs) were prepared in two different ways using the biopolymer kappa- carrageenan (KC) as a dispersant. Evaporative casting and vacuum filtration film-formation processes were compared using electrical characteristics. The conductivity of films prepared by vacuum filtration was higher than films prepared by evaporative casting. MWCNTs films exhibited sensitivity to humidity as high as of 70%, easily outperforming SWCNTs films.

Based on the studies of the synthesis and characterization of carbon nanomaterials, the well controlled synthesis and applications of carbon nanomaterials will be further considered. The application of CNTs and graphene on solar cells is an attractive research field.

List of Publications

Thesis related publications

1. Jin Chu, Xiaoyan Peng, Peter Feng, Yong Sheng, Jianting Zhang, "Study of humidity sensors based on nanostructured carbon films produced by physical vapor deposition", *Sensors & Actuators B* 178 (2013) 508-513

2. Jin Chu, Xiaoyan Peng, Ali Aldalbahi, Marc in het Panhuis, Rafael Velazquez and Peter X Feng, "A simple route to carbon micro- and nanorod hybrid structures by physical vapour deposition", *J. Phys. D: Appl. Phys.* 45 (2012) 395102

3. Ali Aldalbahi, Jin Chu, Peter Feng and Marc in het Panhuis, "Conducting composite materials from the biopolymer kappa-carrageenan and carbon nanotubes", *Beilstein J. Nanotechnol.* 3(2012) 415–427

Other Publications during Ph.D study

1. J. Chu, X.Y. Peng, K. Dasari, R. Palai, P. Feng, "The shift of optical band gap in W-doped ZnO with oxygen pressure and doping level", Materials Research Bulletin 54 (2014) 73-77
2. Jin Chu, Xiaoyan Peng, Zhenbo Wang and Peter Feng, "Sensing performances of ZnO nanostructures grown under different oxygen pressures to Hydrogen", Material Research Bulletin 47 (2012) 4420-4426
3. Jin Chu, Xiaoyan Peng, M. Sajjad, Boqian Yang, Peter.X.Feng, "Nanostructures and sensing properties of ZnO prepared using normal and oblique angle deposition techniques", Thin Solid Films 520 (2012) 3493-3498
4. Xiaoyan Peng, Jin Chu, Boqian Yang, Peter Feng, "Mn-doped zinc oxide nanopowders for humidity sensors", Sensors and Actuators B 174 (2012) 258-262
5. Xiaoyan Peng, Jin Chu, Peter Feng, "Synthesis of WOx-ZnO Double-Layer by Two Step Process". Material letters 73 (2012) 65-67
6. Xiaoyan Peng, Jin Chu, Sajjad Muhammad, Peter Feng, "Study of the structural evolution of crystalline zinc oxide films prepared by PLD technique", International Journal of Material Research 103 (2012) 10-14
7. M. Sajjad, X.Y. Peng, J. Chu, H.X. Zhang, P.X. Feng, "Design and Installation of CO_2- Pulsed Laser Plasma Deposition System for the Growth of Mass Product Nanostructures", Journal of Material Research 28 (2013) 1747-1752
8. Xiaoyan Peng, Boqian Yang, Jin Chu, Peter Feng, "Effects of nitrogen pressure during pulsed laser deposition on morphology and optical properties of N-doped ZnO nanostructures", Surface Science 609 (2013) 48-52
9. X.Y. Peng, M. Sajjad, J. Chu, B.Q. Yang, P.X. Feng, "Studies of structural evolution and sensing properties of ZnO nanocrystalline films", Applied Surface Science, 257 (2011) 4795–4800
10. Peter Feng, Hongxin Zhang, Xiaoyan Peng, M. Sajjad, and Jin Chu , "A novel compact design of calibration equipment for gas and thermal sensors", Review of Scientific Instruments. 82 (2011) 043303